Global Brain Connectivity Analysis by Diffusion MR Tractography:
Algorithms, Validation and Applications

PAR

Xavier GIGANDET

EPFL

ÉCOLE POLYTECHNIQUE
FÉDÉRALE DE LAUSANNE

Suisse
2009

Les questions montrent l'étendue de l'esprit et les réponses sa finesse.

Joseph Joubert

Acknowledgements

I met Prof. Jean-Philippe Thiran for the first time in 2002, during his introductory course on signal processing. His passionate presentation of the topic and the great enthusiasm with which he was showing the potential applications are undoubtedly at the origin of my interest in image processing. I would like to thank him for having offered me the opportunity to become a PhD student at the signal processing laboratory and for his support during all these years. I also had the chance to have an exceptional advisor, Dr. Patric Hagmann, who introduced me gently into the world of diffusion MRI and generously shared his knowledge. I would like to thank him for the brilliant ideas he shared with me, for his helpful advices and for the passionate discussions we had.

A thesis is never an individual work, and many people participated: Dr. Leila Cammoun, Dr. Gunnar Krueger, Dr. Maciej Kurant, Prof. Olaf Sporns, Dr. Christopher Honey, Dr. Cristina Granziera and Prof. Reto Meuli. Without their help and their advices, this thesis would not have been achieved. For all that I would like to thank them. I would also like to thank all the members of the diffusion team who contributed to the most recent projects and will pursue this work in the future: Stephan Gerhard, Elda Fischi Gomez, Alessandro Daducci, Alia Lemkaddem and Djalel Eddine Meskaldji.

Then, there are many persons who punctually helped me, for example to perform MRI acquisitions or to solve technical problems. I would like to thank Nicolas Chevrey, Tobias Kober, Delphine Ribes, Dr. Meritxell Bach Cuadra, Dominique Zosso, Gilles Auric and all the anonymous I may have forgotten, from the lab or elsewhere. Special thanks also to Adeline Jabès, Benoîte Bargeton and Guillaume Azarias, members of the *neuroteam*, with whom I shared happiness, doubts, despair and doctoral courses. Finally, I would like to thank my family and my friends for their endless support.

Contents

List of Figures

List of Tables

Version Abrégée

Le cortex cérébral humain est constitué d'environ 10^{10} neurones, organisés selon un réseau complexe de circuits locaux et de connexions à longue distance. Ces dernières années ont été marquées par un intérêt grandissant de la part de la communauté neuro-scientifique envers l'étude de ce réseau, communément appelé *connectome* humain. En raison de sa capacité à mesurer la micro-structure des tissus biologiques *in vivo* et de manière non invasive, l'IRM de diffusion est un outil de choix pour l'analyse à l'échelle millimétrique des trajectoires des axones dans le cerveau. Alors que le niveau du neurone reste inatteignable, l'IRM de diffusion permet d'obtenir une estimation à basse résolution du connectome humain, qui devrait révolutionner l'étude de la neuro-anatomie normale et pathologique.

Cette thèse commence par une brève introduction sur l'IRM de diffusion et la tractographie, procédé par lequel les faisceaux de fibres sont reconstruits à partir des images de diffusion. Puis, une méthodologie permettant la création de matrices de connectivité cérébrale est présentée. Ces matrices, obtenues au moyen des résultats de tractographie, constituent une représentation du connectome humain. Partant de la méthodologie développée, une étude est menée sur l'adaptation des algorithmes de propagation de front à la tractographie. Cette approche est comparée aux méthodes de tractographie conventionnelles pour des faisceaux bien connus de fibres associatives, et les avantages et inconvénients de la méthode sont discutés.

Plusieurs solutions sont proposées afin d'évaluer et de valider la méthodologie sous-jacente au connectome. En tractographie, nous développons une méthode permettant d'estimer les contributions respectives du contraste de diffusion et des autres facteurs. Au moyen de cette méthode, nous montrons que nous pouvons avoir une grande confiance dans les connexions à moyenne et à longue distance, alors que les connexions courtes doivent être interprétées avec prudence. Ensuite, nous démontrons la forte relation exis-

tant entre la connectivité structurelle obtenue à partir de la tractographie et la connectivité fonctionnelle mesurée avec l'IRM fonctionnel. Puis, nous comparons la performance de plusieurs techniques d'IRM de diffusion au moyen de mesures basées sur le connectome. Nous montrons que l'imagerie par spectre de diffusion est plus sensible et par conséquent améliore les résultats de tractographie.

Enfin, nous présentons deux applications basées sur l'étude des réseaux. Nous employons le connectome humain pour révéler que l'architecture du cerveau est de type "petit monde", une charactéristique des réseaux efficaces en termes de câblage et d'alimentation en énergie. Nous identifions également les aires corticales appartenant au coeur de la connectivité structurelle. Nous montrons que ces régions appartiennent aussi au *default mode network*, un ensemble de régions couplées dynamiquement qui sont fortement actives lors du repos. Pour conclure, nous insistons sur le potentiel important du connectome humain dans le cadre d'applications cliniques et d'études pathologiques.

Mots-clés IRM de diffusion, tractographie, neuro-anatomie, cortex cérébral, réseaux du cerveau, connectome humain.

Abstract

The human cerebral cortex consists of approximately 10^{10} neurons that are organized into a complex network of local circuits and long-range connections. During the past years there has been an increasing interest from the neuro-scientific community towards the study of this network, referred to as the human *connectome*. Due to its ability to probe the tissue microstructure *in vivo* and non invasively, diffusion MRI has revealed to be a helpful tool for the analysis of brain axonal pathways at the millimeter scale. Whereas the neuronal level remains unreachable, diffusion MRI enables the mapping of a low-resolution estimate of the human connectome, which should give a new breath to the study of normal or pathologic neuroanatomy.

After a short introduction on diffusion MRI and tractography, the process by which fiber tracts are reconstructed from the diffusion images, we present a methodology allowing the creation of normalized whole-brain structural connection matrices derived from tractography and representing the human connectome. Based on the developed framework we then investigate the potential of front propagation algorithms in tractography. We compare their performance with classical tractography approaches on several well-known associative fiber pathways, and we discuss their advantages and limitations.

Several solutions are proposed in order to evaluate and validate the connectome-related methodology. We develop a method to estimate the respective contributions of diffusion contrast versus other effects to a tractography result. Using this methodology, we show that whereas we can have a strong confidence in mid- and long-range connections, short-range connectivity has to be interpreted with care. Next, we demonstrate the strong relationship between the structural connectivity obtained from diffusion MR tractography and the functional connectivity measured with functional MRI. Then, we compare the performance of several diffusion MRI techniques through connectome-based measure-

ments. We find that diffusion spectrum imaging is more sensitive and therefore enhances the results of tractography.

Finally, we present two network-oriented applications. We use the human connectome to reveal the small-world architecture of the brain, a very efficient network topology in terms of wiring and power supply. We identify the cortical areas that belong to the core of structural connectivity. We show that these regions also belong to the *default mode network*, a set of dynamically coupled brain regions that are found to be more highly activated at rest. As a conclusion, we emphasize the potential of human connectome mapping for clinical applications and pathological studies.

Keywords Diffusion MRI, tractography, neuroanatomy, cerebral cortex, brain networks, human connectome.

Preface

1

1.1   Context

Diffusion MRI, providing information about the size and orientation of the multiple compartments lying inside an imaging voxel, has proved to be a powerful tool to probe the tissue microstructure, *in vivo* and non invasively. From the widely used Diffusion Tensor Imaging (DTI) [14] to higher angular resolution MRI methodologies such as Diffusion Spectrum Imaging (DSI) [227], diffusion measurements in the brain white matter have given a new breath to fiber tract architecture studies, thus opening a window on brain anatomical connectivity [25, 182]. During the last decade, these techniques have induced an innumerable quantity of studies related to normal or pathologic neuroanatomy.

However, beyond the aim of analyzing and characterizing individual fiber pathways in the human brain, there has been a tremendous interest towards the connectivity profile of the entire brain. Given the increasing importance of whole-brain connectivity, the scientific community introduced in 2005 a specific term referring to the complete description of the brain structural connectivity: the *human connectome* [89, 196].

As the reader might expect, the optimal solution to build and map the human connectome is non-trivial, and thus raises many issues. There is a huge discrepancy between the real brain neuronal network composed of 10^{10} neurons and the rough estimate provided by diffusion MR tractography. Which diffusion MR acquisition techniques and which tractography algorithms are better suited to build the connectome? Which is the adequate scale to analyze the coarse grain topology of the brain network? What are the optimal representations of the connectome? How can we register the connectomes of several human brains in order to perform group studies?

1.2 Outline

In the present work, we not only try to address the mentioned issues, but we also investigate several solutions in order to evaluate and validate the connectome-related methodology. In addition, we also demonstrate the high potential of this brain exploration tool through several neuro-scientific applications. In order to reflect those multiple aspects, this thesis is divided into three parts, as follows.

After an introduction on diffusion MRI and tractography, we present our approach to map the human connectome at multiple scales. Based on this methodology, we propose a new tractography algorithm especially designed for whole-brain tractography with high angular resolution diffusion MR acquisitions. In Part II, we cover different evaluation and validation experiments. First, we present a method to assign a confidence level to the fibers produced by tractography. Then, we show through computational modelling how functional connectivity can be predicted from structural connectivity, demonstrating the relevance of the human connectome. Next, we go through a connectome-based performance comparison between various diffusion MRI techniques. In Part III, we show two applications of the human connectome. We analyze its network properties and use the associated measures to show some interesting characteristics of the brain connectivity as a whole. Finally, based on several network measures we define the cortical areas that belong to the core of structural connectivity.

1.3 Main Contributions

The main contributions of this thesis are the following:

- Development of a methodology to map the human connectome, based on the combination of DSI tractography and cortex parcellation.

- Development of a new DSI tractography algorithm.

- Development of a methodology to assign a confidence level to the fibers obtained with MR tractography.

- Demonstration of the relationship between functional connectivity derived from resting-state functional MRI and structural connectivity measured with tractography.

- Performance analysis of different diffusion MRI techniques based on multiple MRI experiments.

- Analysis of the network properties and the topology of the human brain through a variety of graph-based measurements.

- Demonstration of the relationship between the structural core of the human cerebral cortex defined using DSI tractography and the brain's default network.

Part I

Whole-Brain Diffusion MR Tractography

Diffusion MRI <div style="float:right">**2**</div>

2.1 Introduction

The aim of this chapter is to provide the reader with a review of the basic principles behind molecular diffusion and diffusion MRI. Whereas a detailed description of the physical concepts underlying Nuclear Magnetic Resonance (NMR), MRI and diffusion MRI can be found in the literature [24, 35], we focus on the description of the existing reconstruction techniques for diffusion imaging.

First, we cover the basics in molecular diffusion and diffusion MRI. Then, we present various reconstruction techniques for diffusion MRI: Diffusion Tensor Imaging (DTI), Q-Ball Imaging (QBI) and Diffusion Spectrum Imaging (DSI). These three schemes have been extensively used by the scientific community and are considered as references in the field of diffusion MRI.

2.2 The concept of molecular diffusion

Molecular diffusion is macroscopically defined as the process by which the molecules are transported from a region of high concentration to a region of low concentration, thus decreasing the gradient of concentration. As an example, we can consider the case of a water-soluble dye placed in a glass of water that spreads out and results in a solution with a uniform color. In 1855, Adolf Fick was the first to give a mathematical description of this phenomenon [60].

Fick's law and the diffusion equation

Fick's first law describes the dependence of the molecular flux J on the molecular concentration gradient ∇C:

$$J = -D\nabla C, \tag{2.1}$$

with D being the diffusion coefficient, or diffusivity. When considering a closed system, the number of particles is conserved. This is described by the continuity equation, which states that the divergence of the flux is equal to the negative rate of change of the concentration:

$$\frac{\partial C}{\partial t} = -\nabla \cdot J. \tag{2.2}$$

By combining Equation 2.2 with Fick's first law and considering the diffusion coefficient D as a constant, we obtain the diffusion equation:

$$\frac{\partial C}{\partial t} = D\nabla^2 C. \tag{2.3}$$

In the case of an unbounded medium with spatially uniform diffusivity, we can easily compute the solution of the diffusion equation. Setting the initial condition $C(\mathbf{r}, 0) = \delta(\mathbf{r} - \mathbf{r_0})$, with $\mathbf{r}$ the position, we obtain:

$$C(\mathbf{r}, t) = (\frac{1}{\sqrt{4\pi Dt}})^3 \exp(\frac{-(\mathbf{r} - \mathbf{r_0}) \cdot (\mathbf{r} - \mathbf{r_0})}{4Dt}), \tag{2.4}$$

indicating that the concentration spreads with time as a dilating Gaussian distribution. This equation suggests that we can determine the diffusion coefficient D by measuring the evolution of the concentration, using for example radioactive or fluorescent tracers. However, these techniques are inherently invasive and are therefore not suitable for *in vivo* studies.

The Brownian motion

Another approach consists in measuring the diffusion coefficient by monitoring the diffusion process itself. Indeed, whereas under equilibrium conditions the macroscopic description would suggest no diffusion, the molecules still exhibit a random motion caused by thermal energy. This phenomenon, illustrated in Figure 2.1, is called Brownian motion, from the name of the botanist Robert Brown, who first reported on this random movement of particles [29]. In 1905, Einstein [57] showed that the diffusion coefficient defined in Equation 2.3 also appears in the variance of the conditional probability distribution $P(\mathbf{r}|\mathbf{r_0}, t)$, the probability of finding a molecule at a position $\mathbf{r}$ at time t given its initial position $\mathbf{r_0}$. Moreover, in the case of free diffusion, this conditional probability distribution follows the same Gaussian distribution as the one describing the concentration. From this constatation results a relation between the diffusion coefficient D and the root mean square of the diffusion distance, as follows:

$$\langle (\mathbf{r} - \mathbf{r_0}) \cdot (\mathbf{r} - \mathbf{r_0}) \rangle = 6Dt. \tag{2.5}$$

From this equation, we directly understand that we can infer the diffusion coefficient from the measurement of the displacement of the molecules. NMR, which is currently the only tool allowing the noninvasive measurement of molecular displacements in the micron range, is thus a perfect candidate for the study of diffusion *in vivo*.
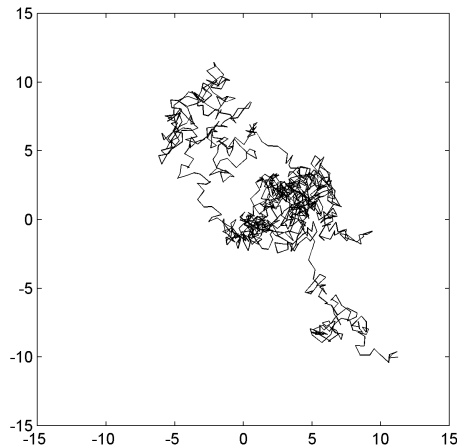
Figure 2.1: Simulation of the two-dimensional Brownian motion of a particle.

2.3   Diffusion in the human brain

From histological studies we know that biological tissues are highly heterogenous. They are composed of different compartments with specific diffusion coefficients, e.g. intracellular and extracellular volumes, glial cells, axons, neurons. In such an heterogenous medium, the Brownian motion of water molecules is strongly influenced by the environment, since the particles will bounce off, cross and interact with tissue components such as cell membranes, fibers and macromolecules. These interactions significantly reduce the diffusion distance compared to the free diffusion case, and in general the diffusion displacement does no longer follow a Gaussian distribution. In this case, we speak of restricted diffusion. It is worthwhile to note that this effect is observed only with long enough diffusion times, so that water molecules have the time to probe the local environment.

A particularly interesting case is the neural tissue, which consists in a specific organization of parallel bundles made of tightly packed axonal fibers. This coherently ordered arrangement of fibers found in nerve and white matter (WM) significantly affects the diffusion, which is faster in the direction of the fibers than in the transverse direction. This phenomenon called anisotropic diffusion [42] is illustrated in Figure 2.2. Whereas the anisotropy is undoubtedly related to the orientational property of the neural tissue, the contributions of the tissue microstructure components to the anisotropic diffusion are still not clearly defined. Several studies tend to demonstrate that the axonal cellular membranes, that restrict water diffusion both in the intracellular and extracellular volumes, constitute the major source of anisotropy [19]. The myelin sheath that surrounds the axons and which is composed of numerous lipid bilayers probably also modulate the degree of anisotropy.

However, more than the anisotropy, diffusion measurements in the brain WM allow us to obtain the main directions of diffusivity, which provides us with an information about the orientation of the axonal bundles. This information is of the highest importance for the understanding of brain anatomical connectivity, and opens a way towards the study of normal or pathologic neuroanatomy. This explains why measuring diffusion in the human brain is of high interest.
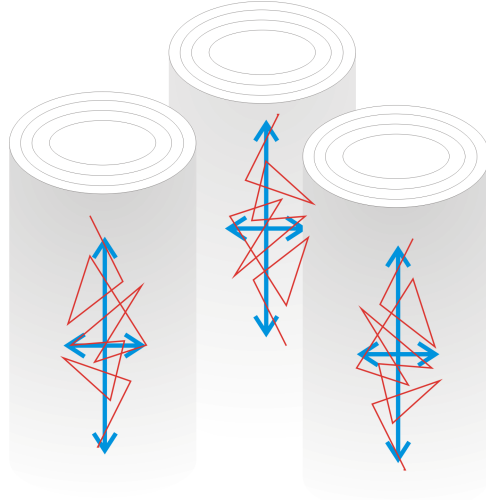
Figure 2.2: Illustration depicting the axonal organization in neural tissue. The diffusion is faster in the direction of the axons than in the transverse direction.

2.4 Measuring diffusion with MRI

Introduced in the 1970s [136], MRI is a powerful tool allowing the study of the anatomy *in vivo* with a sub-millimetric spatial resolution. This is achieved by perturbing with electromagnetic waves the magnetization of water hydrogen nuclei induced in a strong and homogenous magnetic field. Depending on the nature of the biological tissue, the speed to which the water magnetization returns to the equilibrium state varies. This property, called the relaxation time, is the basis for the contrast of anatomical MRI. For more details on MRI, please refer to [35].

Diffusion contrast

In order to enable the measurement of diffusion with MRI, it is sufficient to add a pair of sharp magnetic field gradient pulses to a conventional MRI sequence [200], such as a simple Pulsed Gradient Spin Echo (PGSE), as depicted in Figure 2.3. The gradient vector is denoted by $\mathbf{g}$, and the pulse spacing and duration by Δ and δ, respectively. The first pulse magnetically labels spins carried by molecules according to their spatial location, since the magnetic field varies along one direction. The resulting phase shift is given by:

$$\phi_1 = \gamma \mathbf{g} \cdot \int_0^\delta \mathbf{x}(t)\mathrm{d}t, \tag{2.6}$$

where $\mathbf{x}(t)$ is the spin position at time t and γ is the gyromagnetic ratio.

The phase shift ϕ_1 is then reverted by the π pulse, thus transformed into $-\phi_1$. Next, the second pulse produces a phase shift ϕ_2:

$$\phi_2 = \gamma \mathbf{g} \cdot \int_\Delta^{\Delta+\delta} \mathbf{x}(t)\mathrm{d}t, \tag{2.7}$$

resulting in a net dephasing $\delta(\phi)$:

$$\delta(\phi) \quad = \quad \phi_2 - \phi_1 \tag{2.8}$$
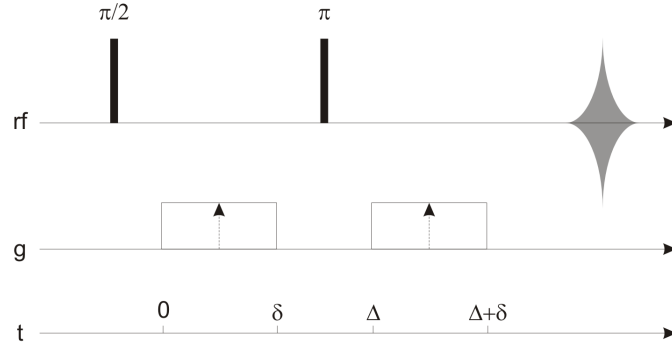
Figure 2.3: Time diagram of the Stejskal and Tanner pulsed gradient spin echo (PGSE) sequence. Δ and δ are the pulse spacing and pulse duration, respectively.

$$= \gamma \mathbf{g} \cdot [\int_{\Delta}^{\Delta+\delta} \mathbf{x}(t) \mathrm{d}t - \int_{0}^{\delta} \mathbf{x}(t) \mathrm{d}t]. \tag{2.9}$$

For a moment, let us consider that the pulse duration δ is negligible compared to the pulse spacing, that is $\delta \ll \Delta$, also called narrow pulse approximation. In this case, we can show that the net dephasing is proportional to the spin displacement $\mathbf{r}$, as follows:

$$\delta(\phi) = \gamma\delta\mathbf{g} \cdot [\mathbf{x}(\Delta) - \mathbf{x}(0)] \tag{2.10}$$
$$= \mathbf{q} \cdot \mathbf{r}, \tag{2.11}$$

where $\mathbf{q} = \gamma\delta\mathbf{g}$ is defined as the gradient wave vector.

MR signal

The MR signal results from the voxel average ($\langle \cdot \rangle$) dephasing of the individual spins and is given by:

$$S_\Delta = S_0 \langle e^{\mathrm{i}\delta(\phi)} \rangle, \tag{2.12}$$

where S_0 is a constant that can be computed by the spin echo experiment without applying the diffusion weighting, i.e. without applying the pair of gradient pulses.

Pursuing with the narrow pulse approximation and considering the voxel average as an expectation $E(\cdot)$, we can see that the MR signal is proportional to the characteristic function of the spin displacement $\mathbf{r}$ [226]. This yields a Fourier relationship between the MR signal S_Δ and the underlying density $\bar{p}_\Delta(\mathbf{r})$, as follows:

$$S_\Delta(\mathbf{q}) = S_0 E(e^{\mathrm{i}\delta(\phi)}) \tag{2.13}$$
$$= S_0 \int_{\Re^3} \bar{p}_\Delta(\mathbf{r}) e^{\mathrm{i}\mathbf{q}\cdot\mathbf{r}} \mathrm{d}^3\mathbf{r}, \tag{2.14}$$

with $\bar{p}_\Delta(\mathbf{r})$ representing the density of the average relative spin displacement in a voxel. In other words, this term can be seen as the voxel average of the individual spin conditional probability distributions. When there is no net translation or flux, it describes the voxel averaged diffusion process. In what follows, $\bar{p}_\Delta(\mathbf{r})$ will also be called the average propagator, or diffusion spectrum.

In practice, magnetic gradient pulses must have a non-negligible duration in order to produce measurable diffusion sensitization. As a consequence, the narrow pulse approximation is no longer verified, and we have $\delta \approx \Delta$. In that case, we must replace the displacement vector $\mathbf{r}$ by the average dynamic spin displacement:

$$\mathbf{r} = \frac{1}{\delta} \int_{\Delta}^{\Delta+\delta} \mathbf{x}(t)\mathrm{d}t - \frac{1}{\delta} \int_{0}^{\delta} \mathbf{x}(t)\mathrm{d}t. \tag{2.15}$$

$\mathbf{r}$ now represents the displacement between the spin mean position during the first pulse and the spin mean position during the second pulse. Considering Equation 2.15 the description of the MR signal remains valid. However, we have to keep in mind that for a given pulse spacing Δ the longer the pulse duration δ, the less contrasted the MR signal.

2.5 Diffusion Tensor Imaging (DTI)

Introduced by Basser et al. in 1994 [14], the diffusion tensor model is based on the hypothesis that diffusion is unrestricted, which allows to model the diffusion by a Gaussian distribution. Although this assumption is not correct due to the nature of biological tissues, DTI has proved to be very useful in the study of diffusion in the human brain (see for example [25, 26]), and has become part of many routine clinical protocols.

Measuring the diffusion tensor

As already mentioned, the diffusion in an unbounded medium is fully described by the scalar diffusion coefficient D. However, in the case of an anisotropic medium, the characterization of the diffusion requires a second order symmetric tensor, $\mathbf{D}$, which describes the diffusion along each direction. The average propagator $\bar{p}_{\Delta}(\mathbf{r})$ for an anisotropic Gaussian diffusion is thus given by:

$$\bar{p}_{\Delta}(\mathbf{r}) = \frac{1}{\sqrt{\det |\mathbf{D}|(4\pi\Delta)^3}} \exp(-\frac{\mathbf{r}^T \mathbf{D}^{-1} \mathbf{r}}{4\Delta}). \tag{2.16}$$

By replacing the average propagator in Equation 2.14, we can deduce the MR signal under the narrow pulse approximation ($\delta \ll \Delta$):

$$S_{\Delta}(\mathbf{q}) = S_0 \exp(-\Delta \mathbf{q}^T \mathbf{D} \mathbf{q}). \tag{2.17}$$

Since the diffusion tensor is a 3x3 symmetric matrix, six elements have to be determined. As a consequence, at least six diffusion-weighted images with different gradient orientations are needed in order to fully reconstruct the diffusion tensor. An additional non-weighted image is also required to measure S_0. The gradient directions are usually chosen so that they are uniformly distributed over a sphere. The diffusion tensor is then evaluated by solving the system of equations given by the signal in Equation 2.17. In practice, a higher number of gradient directions is used in order to have a more reliable measurement.

The various imaging parameters are commonly described by a single scalar, the b-value, defined as follows:

$$b = \Delta \|\mathbf{q}\|^2 = \Delta \gamma^2 \delta^2 \|\mathbf{g}\|^2. \tag{2.18}$$

For the Stejskal-Tanner scheme, Δ is usually replaced in the b-value by the effective diffusion time ($\Delta - \delta/3$), in order to compensate for the finite duration of the gradient pulse [24].
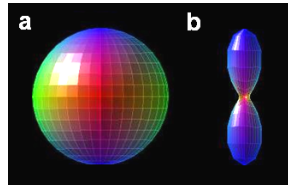
Figure 2.4: a: Example of a fuzz ball with a ball-like shape, in the case of an isotropic medium. b: Example of a fuzz ball with a peanut-like shape, typical in the anisotropic case.
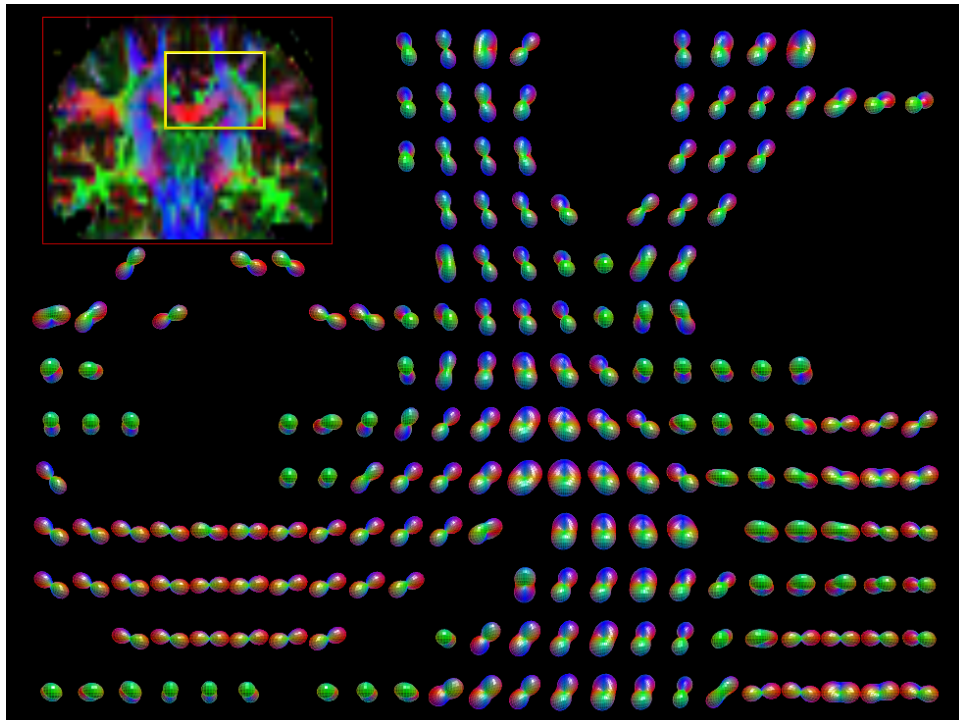
Figure 2.5: Zoomed coronal slice of a human brain, showing the diffusion tensors represented as fuzz balls. The displayed region is located within the yellow box shown in the color FA map (upper left).

Visualization of the diffusion tensor

A common representation for DTI images is a three-dimensional plot, in which each voxel contains a fuzz ball whose surface is given by the set of points $\mathbf{u}^T\mathbf{D}\mathbf{u}$, with $\mathbf{u}$ a vector defined on the unit sphere. With this representation, anisotropic regions display peanut-like shapes whose orientation corresponds to the orientation of the axonal bundles, whereas isotropic regions display ball-like shapes, as shown in Figure 2.4. As an illustration, a zoomed coronal section of a human brain showing DTI represented as a fuzz ball field is displayed in Figure 2.5.

Another way of visualizing the diffusion consists in displaying various scalar measures derived from the diffusion tensor. Two common measures are the mean diffusion $\langle\mathbf{D}\rangle$ and
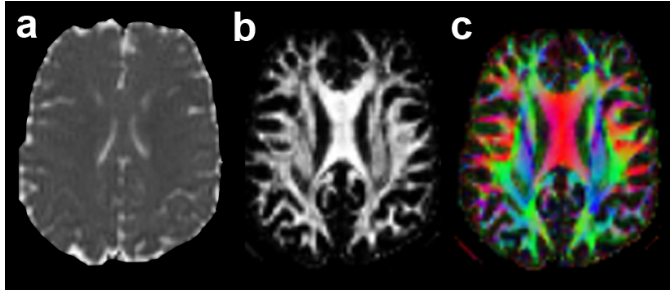
Figure 2.6: Axial slice of a human brain, showing scalar maps derived from DTI. a: mean diffusion, b: fractional anisotropy, c: color-coded fractional anisotropy (green: anterior-posterior direction, blue: head-feet direction and red: left-right direction).

the fractional anisotropy FA. They are given by:

$$\langle \mathbf{D} \rangle = \frac{1}{3}\text{Trace}(\mathbf{D}),\qquad(2.19)$$

$$FA = \sqrt{\frac{3\sum_i(\lambda_i - \langle\lambda\rangle)^2}{2\sum_i \lambda_i^2}},\qquad(2.20)$$

where λ_i and $\langle\lambda\rangle$ are the eigenvalues, respectively the mean of the eigenvalues, of the diffusion tensor $\mathbf{D}$. The mean diffusion allows to distinguish areas of high diffusivity from areas of low diffusivity. The fractional anisotropy characterizes the amount of anisotropy of the diffusion tensor and highlights fibrous regions. Note that the principal eigenvector of $\mathbf{D}$ can be used to apply a RGB color code to the map of fractional anisotropy, in order to add information about the main direction of diffusion. Examples of scalar maps are shown in Figure 2.6.

2.6 Diffusion Spectrum Imaging (DSI)

As seen previously, the diffusion tensor model assumes that the diffusion can be modelled by a Gaussian, which is a function which admits only a single directional maximum. As a consequence, the diffusion tensor model can only capture a single direction of diffusion inside each imaging voxel. However, at the scale of a MR voxel (approximatively 2mm), there is typically a distribution of fiber orientations within each voxel, due to partial volume effects between adjacent or crossing tracts [6,69,216]. In this case, DTI measures the mean of the underlying fiber directions, which of course does not reflect the true direction of the axonal bundles. Consequently, in voxels where there are more than one preferred fiber direction, the diffusion contrast is lost. Recently, Behrens et al. [21] showed that one third of white matter voxels are affected by this problem.

Diffusion spectrum imaging is a model-free approach that allows to measure diffusion without making any assumptions about the form of the underlying diffusion function. Introduced by Wedeen et al. in 2000 [227], it has the capacity to resolve multiple intra-voxel fiber directions.

Measuring the diffusion spectrum

As seen in Section 2.4, there is a Fourier relationship between the MR signal and the diffusion spectrum (under the narrow pulse approximation):

$$S_\Delta(\mathbf{q}) = S_0 \int_{\Re^3} \bar{p}_\Delta(\mathbf{r}) e^{i\mathbf{q}\cdot\mathbf{r}} d^3\mathbf{r}. \tag{2.21}$$

We can therefore obtain the diffusion spectrum by taking the Fourier transform of the MR signal, as follows:

$$\bar{p}_\Delta(\mathbf{r}) = S_0^{-1}(2\pi)^{-3} \int_{\Re^3} |S_\Delta(\mathbf{q})| e^{-i\mathbf{q}\cdot\mathbf{r}} d^3\mathbf{q}. \tag{2.22}$$

Note that in the above equation we replaced the MR signal by its modulus in order to exclude phase shifts arising from tissue motion. Indeed, it has been shown that the Fourier transform of the diffusion spectrum due to diffusion is real and positive in the case of spin motion without net flux or intra-voxel incoherent motion [226].

Practically, the diffusion spectrum is obtained by sampling the $\mathbf{q}$-space, which is the space of the spin displacements. A typical way of achieving this consists in taking the points of a cubic lattice within a sphere whose radius is n lattice units, as follows:

$$\mathbf{q} = a\mathbf{q}_x + b\mathbf{q}_y + c\mathbf{q}_z \quad \text{with } \sqrt{a^2 + b^2 + c^2} \leq n, \tag{2.23}$$

with a, b, c integers and $\mathbf{q}_x$, $\mathbf{q}_y$, $\mathbf{q}_z$ the unit diffusion sensitizing gradient vectors in the respective coordinate directions. Note that the signal is usually pre-multiplied by a Hanning window before Fourier transformation in order to ensure a smooth attenuation of the signal at high $\mathbf{q}$-values.

Typical scans are achieved by using $n = 4$ (DSIq4) or $n = 5$ (DSIq5) [79,90,173]. Since the signal is supposed to be symmetric, a hemisphere can be used instead of a sphere. This yields a number of encoding gradients of 129 for the DSIq4 scan and 258 for the DSIq5 scan.

Visualization of the diffusion spectrum

Diffusion spectrum is a six-dimensional imaging technique, and therefore the data need to be simplified in order to allow a practical visualization. The weighted radial summation is a good candidate, as the angular structure of the diffusion spectrum is of the highest interest. Therefore, we define the Orientation Density Function (ODF), which measures the quantity of diffusion along the unit vector $\mathbf{u}$:

$$ODF(\mathbf{u}) = Z^{-1} \int_{\Re^+} \bar{p}_\Delta(\rho\mathbf{u})\rho^2 d\rho, \tag{2.24}$$

with $\|\mathbf{u}\| = 1$ and Z a normalization constant. An example of the diffusion spectrum obtained with DSI in the case of a fiber crossing, as well as the corresponding ODF are shown in Figure 2.7. A zoomed coronal section of a human brain, showing DSI represented as a field of ODFs is displayed in Figure 2.8.
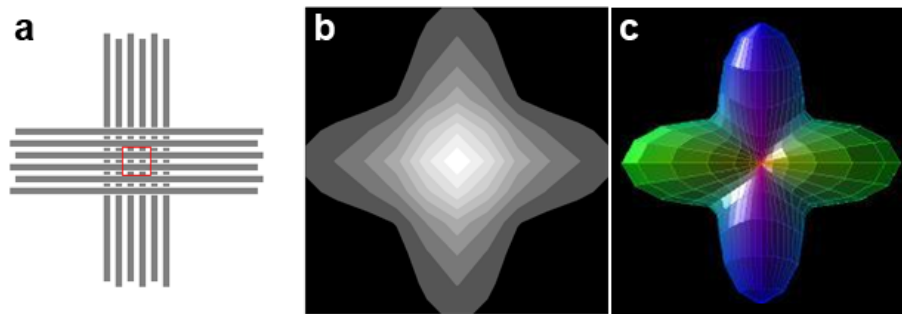
Figure 2.7: a: Model of a fiber crossing, b: diffusion spectrum and c: orientation density function measured with DSI in the case of a voxel located within the fiber crossing area (red box).
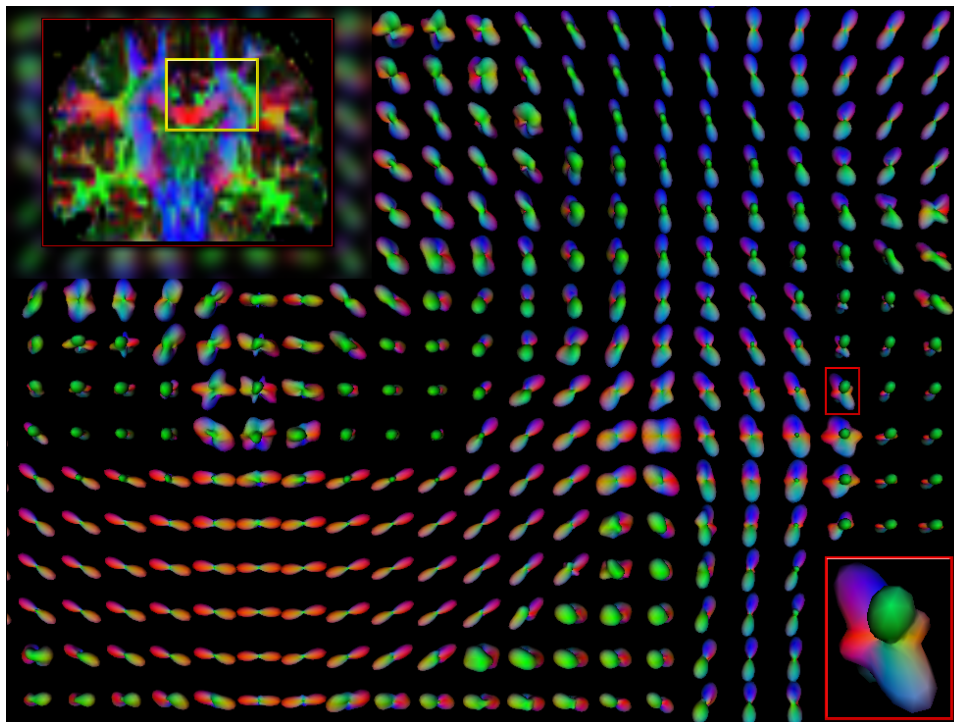
Figure 2.8: Zoomed coronal slice of a human brain, showing the diffusion spectrum MRI represented as a field of orientation density functions. The displayed region is located within the yellow box shown in the color FA map (upper left). A zoom on a single ODF (red box) shows the multiple fiber orientations captured with DSI.

2.7 Q-Ball Imaging (QBI)

Introduced by Tuch et al. [212, 213], Q-Ball imaging (QBI) is a model-free reconstruction scheme, based on the Funk-Radon transform [73, 102]. It aims at providing an approximation to the radial projection of the spin propagator. In other words, it only measures the angular structure of the diffusion spectrum.

The Funk-Radon Transform

The Funk-Radon transform is a transform from the sphere to the sphere. Let us define $f(\mathbf{w})$ a function on the sphere, with $\mathbf{w}$ a unit direction vector. The Funk-Radon transform for a direction $\mathbf{u}$ is given by the sum over the corresponding equator, i.e. the set of points perpendicular to $\mathbf{u}$:

$$
\begin{aligned}
\mathscr{G}[f(\mathbf{w})](\mathbf{u}) &= \int_{\mathbf{w} \perp \mathbf{u}} f(\mathbf{w}) \mathrm{d}\mathbf{w} && (2.25) \\
&= \int f(\mathbf{w}) \delta(\mathbf{w}^T \mathbf{u}) \mathrm{d}\mathbf{w}, && (2.26)
\end{aligned}
$$

with δ the Dirac function. Let us consider a function $f(\mathbf{x})$ defined on the three-dimensional Cartesian space (with $\mathbf{x}$ a three-dimensional vector). By extension of the classical Funk-Radon transform, we can define the Funk-Radon transform of $f(\mathbf{x})$ at a particular radius r', as follows:

$$
\mathscr{G}[f(\mathbf{x})](\mathbf{u}, r') = \int f(\mathbf{x}) \delta(\mathbf{x}^T \mathbf{u}) \delta(|\mathbf{x}| - r') \mathrm{d}\mathbf{x}. \tag{2.27}
$$

Relationship between the MR signal and the ODF

It has been shown that the Funk-Radon transform of the diffusion signal $S_\Delta(\mathbf{q})$ gives a strong approximation of the ODF:

$$
ODF(\mathbf{u}) \approx Z^{-1} \mathscr{G}[S_\Delta(\mathbf{q})](\mathbf{u}, q'), \tag{2.28}
$$

with q' the radius of the sampling shell and Z a normalization constant [215]. Consequently, we directly understand that for a given vector $\mathbf{u}$, it is possible to estimate $ODF(\mathbf{u})$ by integrating the diffusion signal along the equator around $\mathbf{u}$.

In practice, it has a direct consequence on the sampling of the $\mathbf{q}$-space. Indeed, whereas DSI requires a cartesian sampling of the $\mathbf{q}$-space, for QBI it is sufficient to sample the MR signal on a single spherical shell in the $\mathbf{q}$-space. The angular resolution of the method is given by the radius of the shell. We should also mention that the equator points do not coincide with the diffusion sampling points. Therefore, an interpolation is required before computing the integral along the equator. This is generally performed using spherical radial basis function interpolation [213].

2.8 Other reconstruction techniques

Several other reconstruction techniques have been proposed. The multiple tensor (MT) technique [165] proposes to model the diffusion MR signal with a finite mixture of tensors, as follows:

$$
\frac{S_\Delta(\mathbf{q})}{S_0} = \sum_{i=1}^{N} f_i \exp(-\Delta \mathbf{q}^T \mathbf{D}_i \mathbf{q}), \tag{2.29}
$$

with f_i the relative weight of the i-th component in the mixture. A variational framework is used to estimate the parameters of the model. Another similar method is the CHARMED model developed by Assaf et al. [10]. This model express the diffusion MR signal in terms of Gaussian and non-Gaussian contributions. The additional non-Gaussian contribution allows to estimate multiple fiber orientations with a lower uncertainty than what can be obtained with a finite mixture of tensors. Finally, let us also mention the work from Tournier et al., who have proposed the constrained spherical deconvolution (CSD) technique [211]. The CSD method try to model the diffusion MR signal by a single isotropic component and a mixture of infinitely anisotropic components. The fiber orientation distribution is estimated by using constrained spherical deconvolution.

2.9 Conclusion

In this chapter, we have presented an overview of the various strategies proposed to map the fiber orientations. The tensor model used in DTI presents some limitations, especially in areas where several fiber populations interfere. Nevertheless, it is very practical, since it allows to delineate the major fiber structures in the brain, and only requires an acquisition time of approximately 6 minutes (for a typical 64 encoding gradients scheme). This explains why it has become part of many routine clinical protocols. On the other extreme, the DSI requires very long acquisition times (26 minutes for a typical DSIq5 scheme) that are not acceptable for clinical applications. The high angular resolution of the method and its ability to map fiber crossings are nevertheless very interesting for the study of anatomical connectivity and related pathologies. The other presented methods, QBI, CSD, MT and CHARMED, can be considered as intermediate solutions between the two extremes tensor model and model-free reconstruction techniques. They provide a kind of trade-off between acquisition time and angular resolution, and therefore may represent interesting alternatives to DTI and DSI.

The scalar maps, such as the fractional anisotropy or the mean diffusion, are immensely useful in many clinical applications. They can be used for example to localize brain lesions and identify the potentially affected axonal tracts [23,115], or to evaluate the maturity of white matter tracts in premature newborns [161]. They are also helpful for the localization of the main fiber pathways for presurgical planning. However, the scalar maps only show a part of the information obtained by diffusion MRI. Another application of diffusion imaging is the tractography, whose aim consists in inferring the trajectories of the axonal bundles directly from the diffusion measurements [152]. In the next chapter, we discuss in detail this interesting application.

Tractography

3

3.1 Introduction

As we have seen in the previous chapter, diffusion MR data contains a high quantity of information. This information can be processed in order to provide us with maps of fiber tracts. This essential step towards maps of brain connectivity is called *tractography*. It produces lines or trajectories capturing coherent orientations of maximal diffusion that are likely to represent real axonal trajectories. However, we have to keep in mind that there are several orders of magnitude between the resolution of the MR acquisitions and the diameter of the axons. Therefore, tractography is only able to map large axonal bundles, and a single fiber produced by any algorithm is in fact representative of a huge coherent set of real anatomical trajectories.

When going through specialized literature, it is striking to see the huge quantity of tractography algorithms that have been proposed, demonstrating (i) the great interest it has raised in the scientific community and (ii) the variety of strategies proposed to extract information from the diffusion MR images. A tractography algorithm is essentially defined by three global characteristics. The first one is the type of data used to compute the trajectories (DTI, Q-Ball, DSI, or other high angular resolution methods). Indeed, tractography performed with DTI, with only a single preferred direction per voxel, is generally not performed in the same way with DSI data, where multiple fiber directions can share the same voxel. The second characteristic is the technique used to generate the trajectories. We can divide those techniques into two main classes: the line propagation techniques and the energy minimization techniques [152]. The algorithms of the first category directly propagate fibers according to the diffusion information. For energy minimization techniques, the procedure is different. The diffusion information is exploited
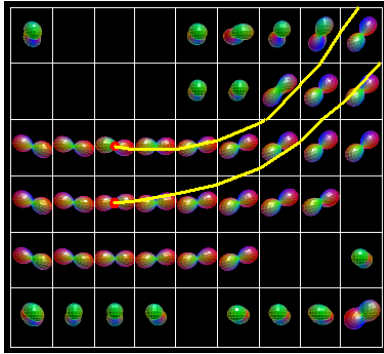
Figure 3.1: Illustration of the FACT algorithm propagation technique on DTI. Every time the fiber enters a new voxel, the orientation is updated to match the local orientation.

to produce probabilistic maps of connectivity, that can be used to create trajectories in the brain white matter. Finally, the third characteristic of a tractography algorithm is the method of selection of the fiber tracts. Several possibilities have been investigated: selection of the desired fibers by capturing fibers starting from, arriving to or simply running through a particular region of interest (ROI), selection of fibers linking two or multiple ROIs, or selection of fibers by other criterions such as the probability of connection, or other scalar value computed along the tract.

The aim of this chapter is to provide the reader with an overview of the existing tractography approaches. We try to focus on the basic principles behind the line propagation techniques and energy minimization techniques, rather than collecting an exhaustive list of all the existing tractography algorithms. Next, we discuss the main advantages and shortcomings of the presented approaches, and we analyze the possibilities and the limitations of tractography.

3.2   Line propagation techniques

Deterministic algorithms

Let us start by considering a DTI data set, that we reduce into a simple vector field by capturing in each voxel the main orientation of diffusion. This vector field is assumed to represent the orientation of dominant axonal tracts. A simple way to build three-dimensional trajectories in this vector field consists in choosing a seed point, and let a fiber expand along the local orientation of the vector field. As soon as the fiber enters a new voxel, the orientation is updated to match the local orientation, as depicted in Figure 3.1. This linear propagation approach, called FACT (Fiber Assignment by Continuous Tracking), is considered as the first published tractography technique [150]. It has been successfully used to reconstruct brain axonal projections in the rat [231], and despite its relative simplicity is still widely used by the scientific community. Others have proposed to propagate the lines using a small step size, the orientation at each step being computed by interpolation of the vector field, or more rigorously by interpolation of the diffusion tensors themselves [15, 50]. These methods have proved to generate smoother tracts, especially for highly-curved tracts with respect to the size of the imaging voxels.

Depending on the type of study, several initialization strategies can be investigated.

If we are interested in a tractus for which we have prior information about its trajectory or about the end regions, initialization points can be chosen in manually defined ROIs. The other approach consists in generating a whole set of fibers, with many initialization points randomly chosen in the white matter, and then selecting the fibers of interest by capturing those that run through the ROIs.

Such kind of propagation techniques requires some criteria to decide when the line propagation process is terminated. To this purpose, the fractional anisotropy is widely used, because it allows to distinguish easily between white matter and gray matter. A simple threshold applied on the fractional anisotropy map allows to define the volume in which fibers can propagate. It is also a convenient way of limiting the effect of noise (which may strongly affect the orientation of the vector field in low anisotropy regions), by preventing fibers to propagate in areas where the orientation uncertainty is high. Another important termination criterion is the maximum angle between two successive steps. Indeed, it is widely assumed that the trajectories of the main fiber tracts in the brain are relatively smooth. As a consequence, if a sharp-turn occurs during the line propagation, it is highly likely that it is due to noise, partial volume effect, or any undesired effect, and that it does not truly reflect the trajectory of the axonal bundles. Practically, the choice of the maximum angle depends on the type of tracts we want to study, as well as on the spatial resolution of the images.

These deterministic algorithms can be easily adapted to higher angular resolution diffusion techniques. In this case, instead of having a single orientation vector per voxel, we can have multiple vectors inside a single imaging voxel corresponding to the set of local maxima of the ODF. During the line propagation process, the fiber expands along the vector that is the most collinear to the previous orientation of the fiber. This approach has been successfully used to reconstruct complex fiber crossing arrangements in post-mortem fixed macaque brain as well as in the healthy human brain *in vivo* [89,95,228]. Figure 3.2 shows the result of whole-brain tractography performed on DSI data of a human brain, using the FACT algorithm.

Probabilistic algorithms

The advent of probabilistic tractography approaches mainly comes from the constatation that deterministic algorithms have difficulties handling with noise, particularly in regions of low anisotropy. The probabilistic algorithms have appeared as soon as 2003, with the Probabilistic Index of Connectivity (PICo) introduced by Parker et al. [159]. The key concept behind this approach consists in exploiting the uncertainty in the orientation of the principal direction of the tensor.

This uncertainty is directly incorporated in the line propagation process, as follows. At each step of the line propagation, instead of propagating along the principal eigenvector of the tensor, the orientation is randomly drawn from a specific probability density function (pdf), representing the error model. This pdf can be built using various techniques. It can for example be modelled from the diffusion tensor itself, as proposed by our group in [96]. In the PICo approach, a pdf is built such that the orientation with maximum probability is aligned with the first eigenvector of the tensor. Its shape is governed by the fractional anisotropy: the lower the FA the wider the pdf, accounting for the higher uncertainty. Others have used a bayesian framework to estimate the pdf, by modelling the underlying fiber distribution [22].
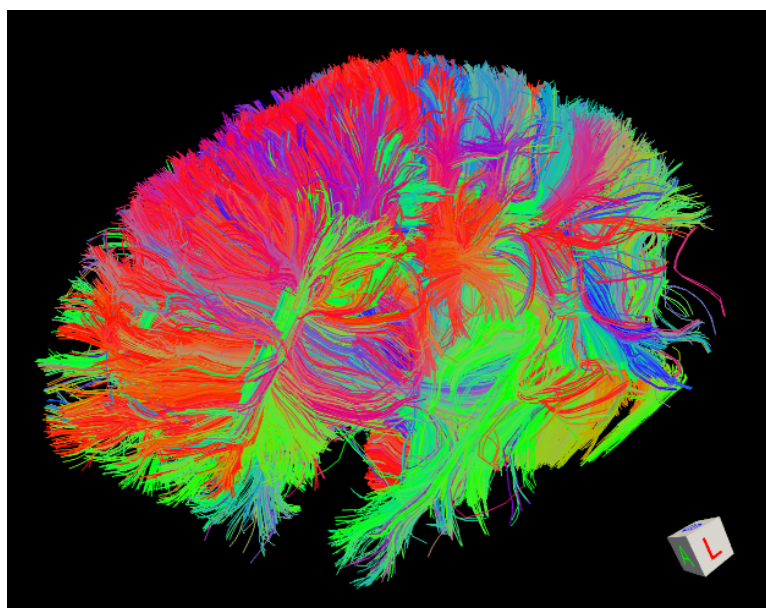
Figure 3.2: Example of a whole-brain FACT tractography experiment obtained on a DSI acquisition of a healthy human brain.
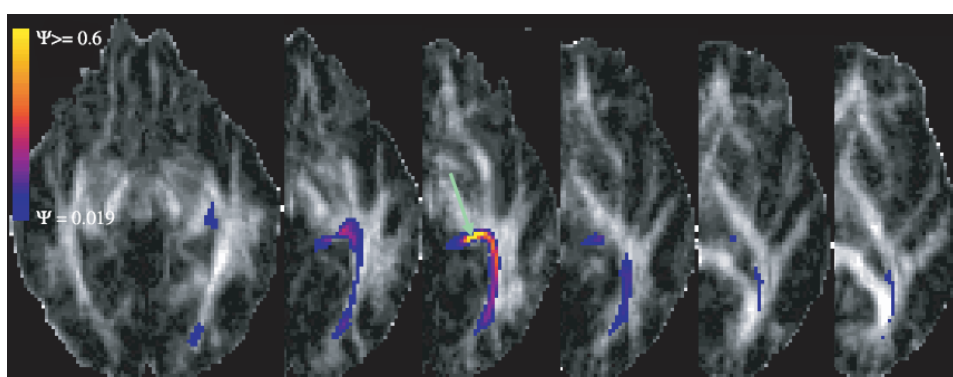
Figure 3.3: Example of connection probability maps of the optic radiation (axial slices, overlaid on fractional anisotropy maps, left to right: inferior to superior). The green arrow represents the starting point for tractography (in the left lateral geniculate nucleus). The color scale shows the probability of connection. This figure is reproduced from [159].

Using this modified tracking process, many fibers are generated from a given starting point, following a Monte Carlo process. Those fibers are then used to create connection probability maps [159]. An example of such a connectivity map is depicted in Figure 3.3. Another way of mapping the connectivity is to map the trajectories that have the highest probability [96].

Those probabilistic techniques have been successfully applied to high angular resolution diffusion MR techniques. The PICo methodology has been extended to handle with persistent angular structures (PAS) and Q-ball imaging, in order to exploit a maximum of information contained in the ODF [158, 187]. Perrin et al. have developed a specific

probabilistic technique for QBI [166]. Let us finally mention an interesting study about the potential of probabilistic approaches with high-angular resolution diffusion MRI [21].

3.3 Energy minimization techniques

Differential geometric framework

Introduced by Sethian in 1996 [184], the fast-marching algorithm allows to model the evolution over time of a front in the space. In the context of DTI tractography, it has been shown that such techniques can produce maps of the connection likelihood, by controlling the front propagation with the main eigenvector of the tensor [160]. Indeed, if we define the front propagation speed so that it is maximal in the direction of the main eigenvector, the time of arrival of the front reflects the coherence in the alignment of the diffusion maxima. Therefore, it provides us with an information about the probability of connection.

The method proposed by Parker et al. [160] consists in three steps, described in what follows:

1. First, a front propagation is performed from a given starting point. Following the procedure proposed by Sethian [184], the voxels are divided into three categories: the *front* voxels that have already been reached by the front, the *narrow band* voxels that are adjacent to front voxels and the *outside* voxels (see Figure 3.4A). At each iteration step, the narrow band voxel that has the smallest time of arrival is added to the front. The time of arrival is defined according to a specific speed function, which depends on the direction of the main eigenvector in the origin and destination voxels, as well as on the direction of the normal to the front (see [160] for more details). Every time a voxel is added to the front, the time of arrival of each narrow band voxel is updated. This procedure produces a map of the time of arrival, as shown in Figure 3.4B.

2. Next, from every point reached by the front, the optimal path can be found by a gradient descent through the time of arrival map. Some examples are shown in Figure 3.4C. Steps 1 and 2 can be repeated for any desired number of starting points, in order to provide a more complete representation of connectivity. Whole-brain tractography can for example be achieved by iterating over all white matter-gray matter interface voxels.

3. As this methodology is able to connect every point in the brain with the starting voxel, a way to select the paths connecting regions for which the probability of existence of a connection is high is needed. Therefore, a specific connectivity metric is assigned to each voxel, which is generally defined as the minimal propagation speed along the tract. When computing the connection paths, only the paths starting from voxels with a connectivity metric above a fixed threshold are considered.

The fast-marching methodology has been used to produce probabilistic maps of connectivity for anterior callosal fibers, optic radiations, and pyramidal tracts in humans [46]. An improved version of the fast marching algorithm has been recently proposed by Staempfli et al. [198]. A qualitative comparison with a classical line propagation technique has shown its high potential in fiber crossing areas (see Figure 3.5). Let us also
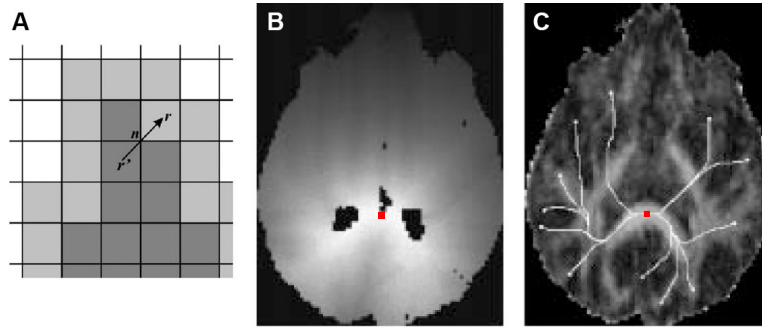
Figure 3.4: A: The voxels are divided into three categories during the front propagation step: the front voxels that have already been reached by the front (dark gray), the narrow band voxels that are adjacent to front voxels (light gray) and the outside voxels (white). B: Example of a map representing the time of arrival. Bright areas = early arrival, dark areas = late arrival. The red point indicates the starting point. C: Connection paths (white) from randomly chosen points (white dots) to the starting point, generated by gradient descent through the time of arrival map. This figure is adapted from [160] and [198].

mention the work of Jbabdi et al. [114], which have successfully adapted the anisotropic fast-marching algorithm [170] for DTI tractography.

Statistical mechanics inspired

Whereas line propagation techniques compute fiber trajectories on a local basis, following the voxelwise diffusion information, others have investigated global optimization approaches inspired from chemistry, and more particularly from polymerization [168]. These techniques consider the total diffusion MR signal in the white matter, the configuration of the fiber tracks being optimized globally. As an illustration, we briefly present the principles of a technique called Gibbs tracking [131].

The idea behind Gibbs tracking is the following: the produced fiber tracts and the totality of the diffusion MR signal are linked and therefore have to be considered simultaneously. Supposing that we have a priori knowledge about the relation between a given fiber population and the resulting MR signal, a global tractography result can be obtained in three steps. First, a set of fibers is created. This set of fibers is then used to calculate the corresponding diffusion signal. Finally, the set of fibers is updated so that it minimizes the difference between the measured and the computed diffusion MR signals.

In practice, neuronal pathways are approximated by small cylinders present in every white matter voxel. An interaction energy is defined such that it favors the formation of the cylinders into chains, following the structure of neuronal fibers. Each cylinder participates to the diffusion MR signal by the mean of a diffusion tensor whose parameters are adjusted according to the cylinder properties. The minimization of the total energy is performed using a Monte Carlo Markov Chain approach and simulated annealing [131]. At each step, a random modification of the configuration of the cylinders is proposed. It can consists in the birth or death of a cylinder, the connection or disconnection of two cylinders, or the move of the ends of the cylinder. The new configuration is then evaluated using the computed diffusion MR signal and the interaction energy. Then, according to the score of the configuration, it is either accepted or rejected. This process is repeated
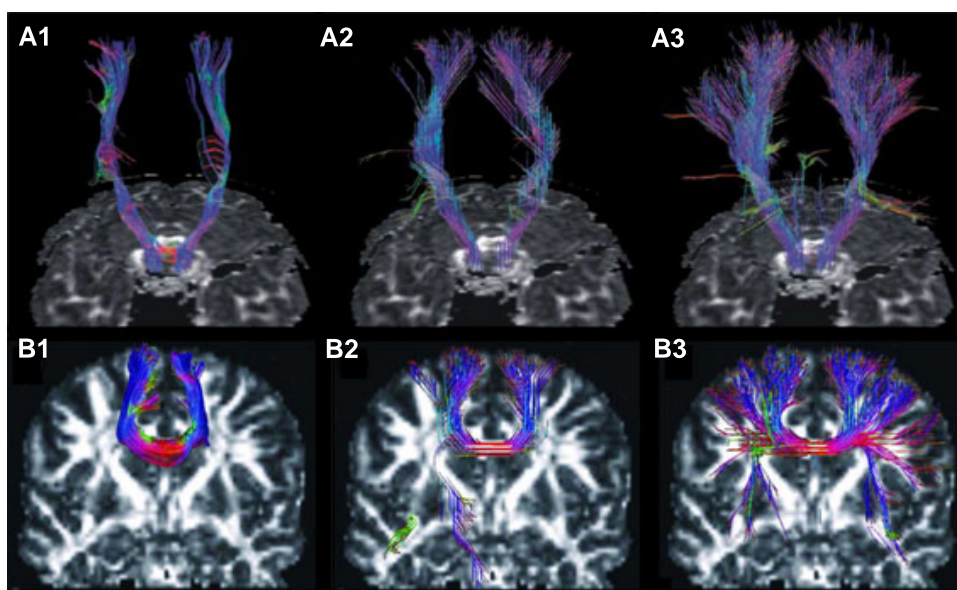
Figure 3.5: A: Reconstructed trajectories of the cortico-spinal tract (1: FACT algorithm, 2: fast marching algorithm and 3: advanced fast marching algorithm [198]). The pathways are seeded in the brainstem. B: Reconstructed trajectories of the commissural fibers (1: FACT algorithm, 2: fast marching algorithm and 3: advanced fast marching algorithm). The seed area is defined in a sagittal plane as the segmented cross section of the corpus callosum. This figure is reproduced from [198].

iteratively.

Several pathways have been successfully reconstructed with the Gibbs tracking, such as the corticospinal tract, the cingulum, the arcuate fasciculus and the optic radiation (see Figure 3.6 and [131]). It has shown to be able to reconstruct spreading and crossing fibers in DTI.

3.4   Discussion

Although diffusion MRI provides valuable information about the orientation of fiber tracts *in vivo*, we have to keep in mind the limitations of the technique, that may affect the results of tractography. Apart from systematic biases such as susceptibility artifacts, aliasing or other perturbations, we can identify two main limitation factors: (i) the noise and (ii) the limited resolution. The consequence of noise on the diffusion tensor data is important: it may lead to a deviation of the principal eigenvector of the tensor from the real fiber orientation. On QBI or DSI, it may even produce unwanted local maxima of diffusion. Noise is therefore an important contributor to aberrant connectivity. The limited spatial and angular resolutions may lead to biased principal directions of diffusion (e.g. smoothing of two diffusion peaks into one) and partial volume effects [5], which are other causes of aberrant fiber tracts.

The line propagation techniques, such as FACT, are the most sensitive to noise. Indeed, at every step the uncertainty in the principal eigenvector of the tensor perturb the direction of the fiber, and thus the error accumulates along the trajectory. Due to
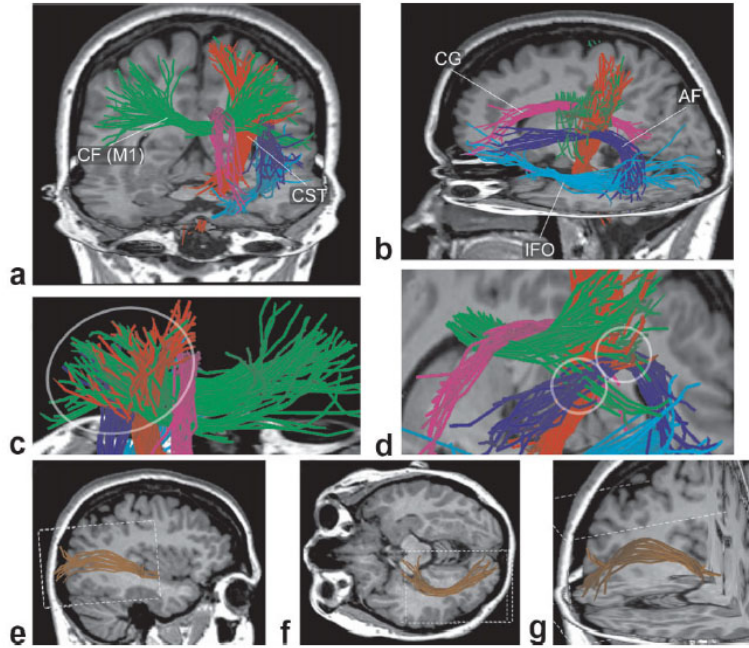
Figure 3.6: Example of fiber tracts computed with the Gibbs tracking. a-b: Callosal fibers (CF), corticospinal tract (CST), cingulum (CG), arcuate fasciculus (AF) and inferior fronto-occipital fasciculus (IFO). c: Spreading fibers of the CST and callosal fibers. d: Fiber crossing between AF, CF, and CST. e-g: The optic radiation. This figure is reproduced from [131].

their inherent global optimization strategy, the energy minimization techniques are less affected by noise. In the case of DTI, the deterministic algorithms are also subject to the problem of fiber crossings. Indeed, as shown previously the diffusion tensor is strongly altered in voxels containing multiple fiber orientations. Depending on the type of deterministic algorithm, the fibers reaching such voxels either follow a wrong trajectory or stop. In this case, the approaches that consider the whole diffusion tensor instead of the principal eigenvector only, can potentially overcome this limitation. Some probabilistic algorithms and energy minimization techniques have shown to be able to deal with fiber crossings using DTI data [131, 198]. Finally, we also have to mention that the deterministic algorithms do not assign a probability of connection to the produced fibers, and therefore there is no possibility to distinguish between fibers resulting from the real diffusion contrast from those resulting from partial volume effects or noise. In contrast, the probabilistic algorithms and the energy minimization techniques provide maps of the probability of connection, which allow to evaluate the confidence we have in the produced tracts.

Although deterministic algorithms may seem to suffer from many limitations related to noise and partial volume effects, they are still largely used by the scientific community. Several studies have shown that despite these limitations, the FACT algorithm and the related streamline-based techniques have the possibility to accurately map the major fiber tracts [50, 182]. Moreover, the energy minimization techniques also have their specific limitations. First, the set of parameters that have to be tuned in order to produce

realistic fiber tracts is difficult to estimate, and thus requires a lot of investigation, whereas deterministic algorithms are nearly button-press applications. Next, these techniques of high complexity often require several days to produce a whole-brain tractography result, whereas it can be achieved in a couple of minutes with the FACT algorithm. The recently developed Gibbs tracking consists in a one-month process [131], which is by far too long to be considered for clinical applications. Finally, the most critical limiting factor is undoubtedly the fact that an energy minimization technique can potentially connect every pair of points in the brain. If this may be useful if we have a strong a priori about the true connectivity, the high quantity of false positives it introduces may dramatically alter the interpretation of the tractography results. Although some criterions may help to distinguish fibers likely to reflect true anatomical connectivity from those arising from partial volume effects or noise, the selection of the most likely fibers remains far from trivial.

3.5 Conclusion

As a conclusion, what is important to remember is that the choice of the tractography algorithm depends on several factors, such as the type of study, the a priori we have about the true connectivity or the type of diffusion data. Each algorithm produces a unique representation of the anatomical connectivity, and can be seen as a specific diffusion contrast. As we will see in this thesis, the validation of the tractography is far from trivial since we have no gold standard to compare the produced results, and it is consequently difficult to estimate which algorithm performs better.

It is however striking to see that the energy minimization techniques have to our knowledge never been applied to high angular resolution diffusion imaging such as DSI. Recently, a simple deterministic algorithm was used with DSI on a macaque monkey brain, and showed significant improvements compared to DTI tractography, especially in crossing fibers areas [228]. Given the interesting results obtained with energy minimization techniques on DTI, we can reasonably suppose that the combination of DSI with such approaches may enhance the possibilities of tractography, especially for non-dominant fiber populations [21].

As mentioned in the preface, tractography is a helpful tool to analyze and characterize specific fiber pathways. Nevertheless, the connectivity profile of the entire brain is also of high interest. When studying whole-brain connectivity, tractography is not sufficient and has to be combined with other techniques and/or other imaging modalities. Our first contribution, discussed in the next chapter, presents a methodology to map the human connectome at multiple scales with diffusion MR tractography.

Mapping the Human Connectome with DSI

<div align="right">4</div>

4.1 Introduction

As shown in the previous chapters, important advances have been made with diffusion MRI. Tractography has allowed imaging of a large number of fiber bundles [50,96,150,182, 225]. These techniques have induced an innumerable quantity of studies related to normal or pathologic neuroanatomy. Some years ago, it became however clear that beyond the aim of characterizing individual fiber bundles, the connectivity profile of the entire brain is of the highest importance in neuroscience.

Unfortunately, the study of neuronal connections in the brain is a difficult and demanding task. Our current knowledge of brain connectivity is largely based on the study of the relationship between symptoms and lesions [28,229] as well as on post-mortem dissections of large fiber tracts [74]. More recently, however, great strides have been made regarding chemical tracing methods in the macaque [181] as well as in humans [47, 201, 223, 232], which have allowed identifying not only gross fiber tracts but also individual white matter (WM) connections. These efforts have resulted in the definitive mapping of a few tens of connections in humans and several hundreds in the macaque. Thanks to the pioneering work based on chemical tracing of Felleman and Van Essen [59] and others [106,107,197], connection matrices representing brain anatomical connectivity have been built.

Although such tracing studies are immensely useful and of perfect resolution, they are confined to post-mortem material and limited to a few connections only. Therefore, new high throughput techniques are needed. Tractography circumvents the drawbacks mentioned above by allowing not only post-mortem but also *in vivo* mapping of the major fiber pathways of the brain, this, however at the cost of lower resolution. Anatomically-based connection matrices have been built from MR tractography [78, 111, 112, 204]. Diffusion-

<div align="center">27</div>

based connectivity has also been used in some studies [20, 126, 206] to parcellate the gray matter (GM).

In what follows, we present a multi-scale approach to map the human connectome. We proceed by constructing normalized whole-brain structural connection matrices derived from DSI tractography at different scales. Those matrices are built using a template-based approach to bring cortical landmarks into register between different subjects. After presenting the method, we extensively test its reliability and reproducibility.

4.2 Cortex parcellation into regions of interest

In order to build the human connectome based on diffusion MRI, two essential steps have to be combined. On one hand, we have to perform whole-brain tractography by using one of the approaches presented in Chapter 3. On the other hand, we have to parcellate the cortex into regions of interest (ROIs). Those ROIs have to be placed in the same anatomical location for each subject, such that the connectivity can be compared locally. Once these two steps are performed, we can identify the fiber bundle connecting each pair of ROIs, by taking all fibers produced by tractography whose end points are located in the corresponding pair of ROIs. Based on this information, a connection matrix can be built such that every row and column correspond to a particular ROI. The information contained in the connection matrix can for example be a connection density, a connection probability, or a scalar value computed along the fiber bundles.

Whereas tractography is discussed in Chapter 3 and the construction of the connection matrix is straightforward, we focus here on the parcellation of the cortex, which is a critical and crucial step towards the mapping of the human connectome.

Inter-subject cortical surface registration

Since we need a precise matching between the ROIs of each subject, a precise inter-subject cortical surface registration is needed. This is a particularly difficult task because of the complexity and variability of brain cortical structures (sulci and gyri). It can be achieved by using a non-rigid registration technique. There are two different types of non-rigid registration techniques: the voxel-based and the feature-based approaches [140, 205].

Voxel-based approach in the voxel-based approach, the objective of the transformation is to optimize a global intensity-based measure, such as gray-level correlation or mutual information. Whereas it is an interesting approach e.g. for subcortical structure registration, it is not appropriate for cortical surface registration because of the complexity and variability of sulci and gyri. [49, 103].

Feature-based approach In this case, identifiable anatomical elements are extracted in both the reference and moving images, and the transformation is determined such that the correspondence between these elements is maximal. Various anatomical features can be extracted, such as representations of the cortical sulci by a point-based [45] or active-contour-based [219] technique, or the surface of identifiable brain structures [203].

Because the cortex is highly convoluted, the alignment of cortical surfaces is a challenging task. In order to tackle this issue, the cortical surface is often projected on a spherical manifold, that preserves both topology and connectivity [101]. Mesh inflation

allows coarse registration after partial cortical flattening [209], and gives rise to spherical feature maps, either after further inflation [64] or conformal mapping [9]. This simplified shape allows registration by powerful registration techniques.

Recently, a set of automated tools called *Freesurfer* (http://surfer.nmr.mgh.harvard.edu) allowing inter-subject cortical surface registration was developed [63,64]. The registration is based on an inflated representation of the cortical surface of each hemisphere, which is aligned onto an average cortical surface generated from 40 individuals.

Multi-scale cortex parcellation

Freesurfer also allows to parcellate the cortex into 66 anatomically typical cortical parcels, defined using curvature-based information [54,61]. The power of the registration technique combined with the automated cortex parcellation make Freesurfer a natural choice for the construction of the human connectome. However, these 66 cortical parcels are not small enough to obtain a high-resolution connection matrix. Ideally, the size of the ROIs should be close to the size of a voxel. But noise, partial volume effects, variance in the registration and brain anatomical variability would hamper reproducibility. With these facts in mind, we propose a minimal ROI size of 1.5 cm^2, resulting in a parcellation of the whole cortex into approximately 1000 ROIs.

Our multi-scale cortex parcellation approach is based on the cortex parcellation proposed by Freesurfer. To avoid any ambiguity in the text, we call the original gyral-based ROIs produced by Freesurfer *parcels*. Those parcels constitute the low-resolution parcellation. Then, we propose to use a partitioning heuristic to generate small and compact ROIs in every parcel of the template cortex. Next, those ROIs are successively aggregated in order to provide five embedded cortical parcellations. Once these parcellations are done, they can be transferred to the subject's cortex by means of cortical surface-based registration. The partitioning heuristic and the creation of the intermediate parcellations are explained in what follows.

Parcellation of the template cortical surface   First, the number of ROIs per parcel, denoted by N_p, is calculated based on the relative surface area of each template parcel, as well as the desired total number of ROIs. This ensures that the variation of the ROI surface area between different parcels remains minimal. Then, for each parcel p, we perform a region growing from a randomly chosen point of p by aggregating the neighboring voxels, until it reaches the desired surface area. This creates the first ROI of parcel p. Next, other ROIs are generated from starting points located close to the already existing ROIs, until the parcel is fully covered with ROIs. In the second phase, we identify the N_p biggest ROIs of the parcel and compute their centers of gravity. We start a second growing process from these points, but this time with all ROIs growing simultaneously. Using this two-phase partitioning heuristic, we obtain ROIs that are compact and of similar size. As we force the template ROIs to reach the same size, the resulting number of ROIs generated on the template cortex is actually 998 and not 1000. It is also important to emphasize that each parcel is subdivided individually, thus preventing the ROIs from overlapping on different parcels. An example of such parcellation is shown on the pre-central and post-central gyri in Figure 4.1.
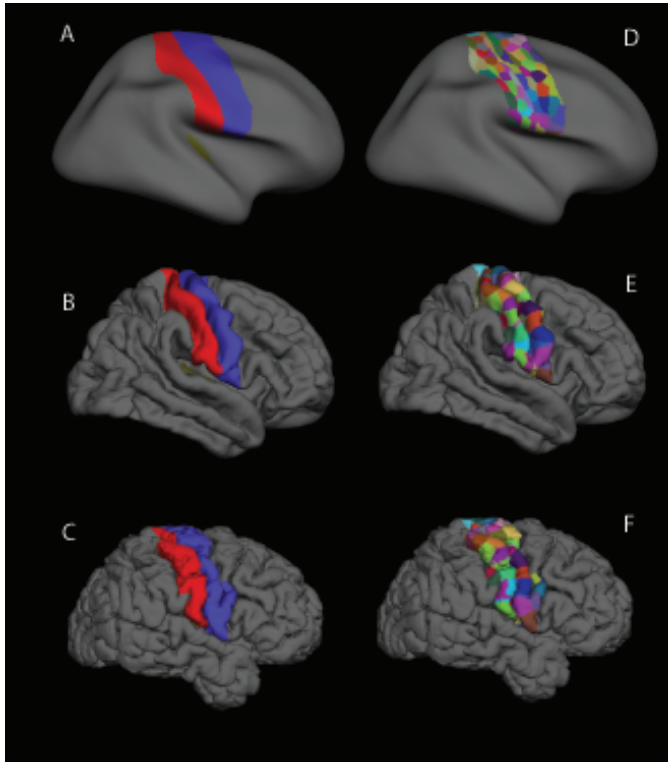
Figure 4.1: Example of subdivisions of two parcels (pre-central and post-central) into small ROIs. The rows show respectively these gyri on the inflated template brain, on the template brain, and on one individual subject. Columns are respectively the original parcels and their subdivision into small ROIs.

Creation of the intermediate resolutions The original cortical partition is made up of N=998 ROIs. However, the most suitable resolution between 998 and 66 ROIs actually depends on the application. Therefore, we create a hierarchical decomposition between 66 and 998 ROIs by successive grouping. On the template brain, 2 or 3 neighboring ROIs at the 998 scale are manually grouped into one ROI to build a partition into 483 ROIs. This grouping operation is repeated several times until the 66 parcels are recovered. Using this heuristic, we end up with 5 embedded cortical parcellations with $N = \{998, 483, 241, 133, 66\}$. In practice, this means that every vertex of the mesh representing the cortex in the freesurfer environment has 5 labels (one per resolution), identifying which ROI it belongs to. An example of this grouping is shown in Figure 4.2.

4.3 From tractography to connection matrices

The overview of the methodology is shown in Figure 4.3. The processing pipeline is divided into two pathways. On one side, the cortical surface is extracted from a high-resolution T1-weighted image and parcellated accorded to the above-mentioned technique. On the other side, whole-brain tractography is performed, resulting in millions of virtual fibers spread over the brain. The combination of these two procedures allows the construction
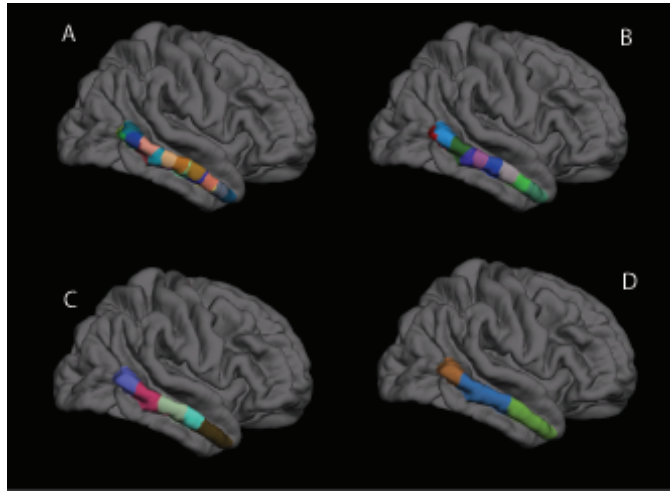
Figure 4.2: Example of grouping for the 20 ROIs of the middle temporal gyrus (A). The ROIs of the same gyrus are grouped into 10 ROIs (scale 483) by successive fusion of neighboring ROIs at the scale just above (B). The operation is repeated yielding 5 ROIs at scale 241 (C) and 3 ROIs at scale 133 (D).

of connection matrices at multiple scales, by computing the connection density between each pairs of ROIs.

Tractography

In order to obtain consistent tractography results, the segmentation of the brain into white matter, cortex and deep cerebral nuclei is an essential step. Actually, the virtual fibers should be generated only in the white matter. To construct the tractography mask, the cortical surface obtained from Freesurfer is first filled. Next, the deep gray nuclei (thalamus, pallidum, putamen, caudate nucleus) as well as the hippocampus, the amygdala and the ventricles are removed from the mask. The location of these structures is obtained by an atlas-based segmentation [62], using the same software. Although other segmentation tools may be more adequate, Freesurfer is chosen here in order to limit the dependency to other softwares, an exhaustive review of brain segmentation techniques going beyond the scope of this thesis.

The choice of the tractography algorithm is far from trivial. In this thesis, we decided to focus on DSI because we strongly believe in the high potential of this diffusion acquisition scheme. The tractography algorithms adapted to such data are however rare, therefore we rely on the streamline approach developed by our group [89, 95] (see Section 3.2). This choice is motivated as follows. First, as discussed in Chapter 3, a line propagation technique is probably more adequate in the case of whole-brain tractography since the limitations of energy minimization techniques, such as the difficulty to tune the parameters or the propensity of those techniques to generate false positive connections, may potentially lead to a wrong interpretation of the connection matrix. Second, we have a strong knowledge about the behavior of the streamline algorithm since it has been extensively tested by our group, which may be a valuable help towards the interpretation of the produced results.
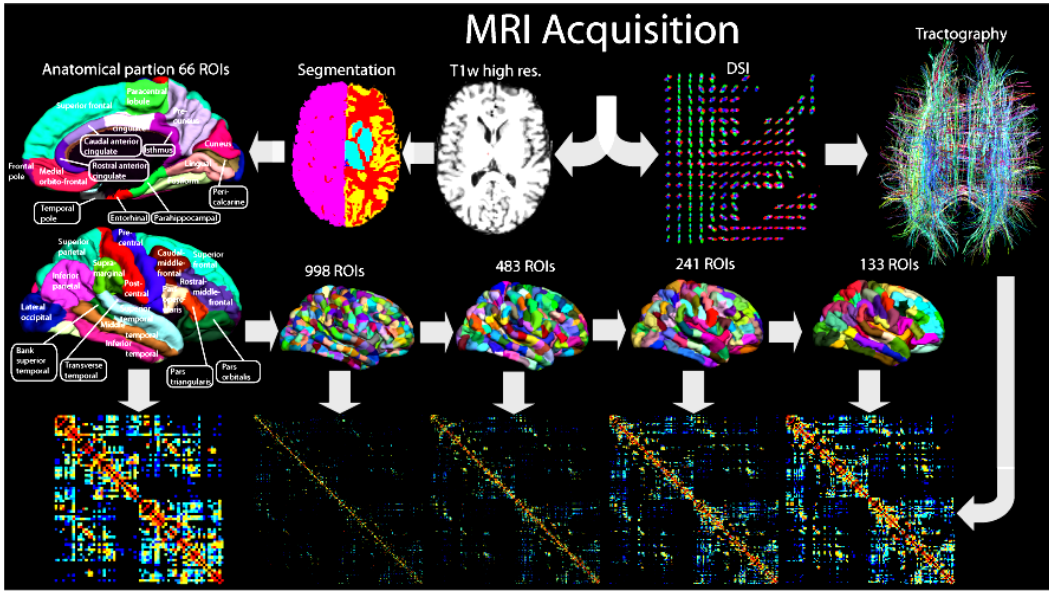
Figure 4.3: Construction of normalized connection matrices. After the acquisition of the diffusion and high-resolution T1-weighted images, the ODF map is calculated from diffusion MRI and used to perform tractography. The T1-weighted image, registered onto the space of diffusion data, is segmented and parcellated into 66 cortical parcels. Each parcel is subdivided into smaller ROIs of approximately identical surface, such that the total number of ROIs is 998. The 998 ROIs are grouped iteratively into bigger ROIs such that 5 scales of cortex parcellation are made available (66, 133, 241, 483, 998). Each set of ROIs is combined with the tractography result to create connection matrices of successive scales.

Using the streamline algorithm, we create a set of fibers for the whole brain (approximately 3 million fibers), as summarized below.

1. At each voxel, the ODF is reduced into a set of normalized direction vectors corresponding to the local maxima of the ODF (i.e. vectors $\mathbf{u}_i$ such that $\phi(\mathbf{u}_j) < \phi(\mathbf{u}_i)$ for all $\mathbf{u}_j$ adjacent to $\mathbf{u}_i$ in the sampled tessellated sphere).

2. We choose a set of initialization points uniformly distributed in each brain WM voxel. The number of points is proportional to the number of direction vectors in the corresponding voxel. For example, in a voxel with 3 directions we initiate 25 fibers along each direction, total 75. The starting points are chosen at random within the voxel.

3. From each initialization point a fiber starts growing in two opposite directions with a fixed step size of 1mm. On entering a new voxel, the fiber growth continues along the direction of the vector $\mathbf{u}_i$ (in the new voxel) whose orientation is the closest to the current direction of the fiber. If this results in a change of direction sharper than 0.25 radian/mm, the fiber is stopped. The growth process of a valid fiber finishes when its both ends leave the WM. Fibers that do not reach the WM-GM interface are eliminated.

Construction of the connection matrix

Considering the cortical parcellation and the WM tractography described previously, the fiber bundle $B(i, j)$ connecting each pair of ROI i and j can be identified. The value of the connection matrix cell $M(i, j)$ is defined as the connection density between this pair of ROIs, defined as follows:

$$M(i, j) = \frac{\sum_{f \in B(i,j)} \frac{1}{l_f}}{S_i + S_j}, \tag{4.1}$$

where S_i is the surface of ROI i and l_f is the length of fiber f along its trajectory. The correction term l_f in the denominator is needed to eliminate the linear bias towards longer fibers introduced by the tractography algorithm. Indeed, let us assume that an axonal bundle B exists in reality and has got a length l_B. The tractography algorithm starts in some voxel of the WM and follows the most probable direction of a bundle. If it happens to start in a voxel that is traversed by the bundle B, the algorithm is likely to follow B until it reaches the WM-GM interface. As every voxel in the WM is chosen as a starting point the same number of times, the longer the bundle B, the more voxels it traverses and the more often it is followed by the tractography algorithm. Consequently, we have to add the correction term l_f to eliminate this bias.

To facilitate the visual interpretation, we organize the connection matrix by taking into account as much as possible the ROI neighborhood. Inspired by the brain development, we arrange the 33 parcels of each hemisphere in a fronto-caudal order. Then, we intuitively define a linear order of the ROIs inside a parcel corresponding to the direction of 'previous parcel to next parcel'. Since this organization is set up only once on a template brain, it remains identical when applied to different subjects. As a result, we obtain for each individual brain a set of 5 matrices (one per resolution) that are embedded in each other. The lowest resolution matrix entails as many entries as parcels in the standard FreeSurfer output, i.e. 66. The highest resolution matrix has 998 entries corresponding to 998 small ROIs (Figure 4.3).

Figure 4.4 represents a typical connection matrix at resolution 133. The connection matrix is organized such that the upper left quadrant (with the red border) represents the connections in the right hemisphere and the lower right quadrant (with the green border) represents the left hemispheric connectivity. The off-diagonal quadrants map the inter-hemispheric connections. This matrix is symmetric since the measured connectivity is not oriented. The color bars at the left and bottom of the matrix help making the correspondence between the matrix entries and the 66 cortical parcels as displayed on the insert images. The color bar on the right codes the connection density seen in the matrix itself in the logarithmic scale.

4.4 Material

After written informed consent and in accordance with our institutional guidelines and ethics committee, fifteen healthy volunteers were scanned with a Siemens TimTrio 3T scanner and a 32-channel receive head matrix coil. We used a diffusion weighted single shot spin echo EPI sequence with the following timing parameters: TR/TE = 6000/138 ms. The maximal b-value was 8000 s/mm^2. Q-space was sampled over a hemisphere using 258 different encoding gradients, and the data were reconstructed following a classical DSI scheme [226] (see Section 2.6), producing a 3D diffusion probability density function (pdf)
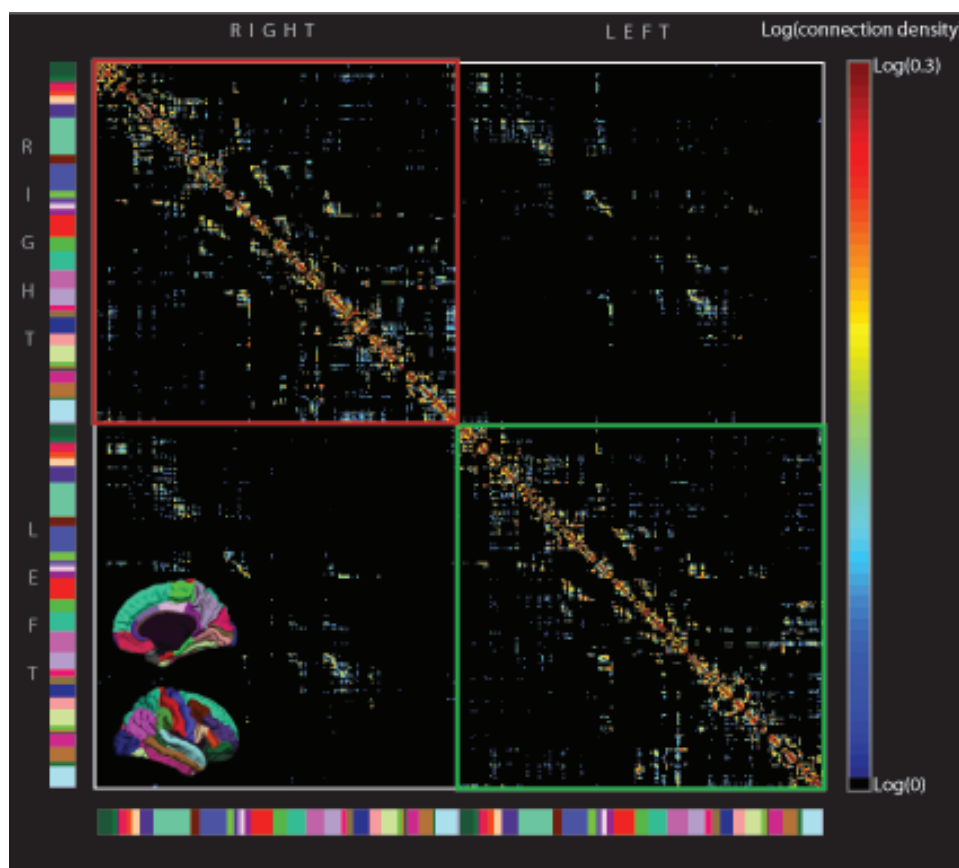
Figure 4.4: Example of a connection matrix at resolution 133, representing the fibers density between every pair of ROIs in the logarithmic scale. The red and green squares correspond respectively to right and left intra-hemispheric connections. Off-diagonal squares represent the interhemispheric connections. X and Y axis color bars represent the parcels with the same color as the template brain (see insert). The right side color bar indicates the logarithm of the fiber density.

in every voxel. The acquisition block was made of 34 slices of a 96 x 96 matrix, with a spatial resolution of 2.21 x 2.21 x 3 mm^3. The acquisition time was approximately 26 minutes. We simplified the data by computing for each voxel the orientation density function (ODF), a radial integration of the resulting diffusion pdf [226], as presented in Section 2.6. In addition, a high-resolution T1-weighted (MP-RAGE) MRI was performed in a matrix of 256 x 256 x 128 voxels of isotropic 1mm resolution. This acquisition was then registered on the diffusion images using an affine registration method [192, 230] (http://www.fmrib.ox.ac.uk/fsl/). For five subjects, the protocol was performed twice on two separate days, in order to test the reproducibility.

4.5 Results

Normalized connection matrices at multiple scales

Figure 4.5 shows some of the connection matrices in different resolutions as they were computed in one subject. It is possible to identify known bundles from the connection matrix. In Figure 4.5 we give several examples. We have selected groups of ROIs that are expected to correspond to language areas (Wernicke's and Broca's areas). The connections between these areas can easily be identified on the matrix and correspond to the arcuate fasciculus. The latter with the uncinate, the occipito-frontal, the middle longitudinal and the superior longitudinal fasciculi form long-distance connections, which are accordingly far from the diagonal of the matrix. The cingular bundle, which is made up mainly of sets of alternating short connections, is located close to the diagonal of the matrix. Another example is the pathways connecting the homotopic primary visual cortices, which are represented in the off-diagonal blocs. The occipito-frontal connection is represented by two squares in the matrix because not all the ROIs belonging to the frontal cortical area are neighbors in an arbitrary linear arrangement of the matrix entries.

It is worthwhile analyzing the empty part of the matrix located in the off-diagonal bloc. As expected from current anatomical knowledge, the inter-hemispheric fronto-temporal, temporo-temporal as well as the fronto-occipital and fronto-parietal connections are not mapped.

Robustness

Since the ultimate aim of the methodology presented here is to study connectivity in groups of subjects, it is essential at this stage to evaluate its robustness. The evaluation is done at the level of the connection matrix itself. We proceed in 3 steps: (i) we process five data sets twice and compare both results, (ii) we scan five subjects twice, process the twin data and compare both outputs, and (iii) we scan, process and compare the fifteen healthy subjects.

Same scan processed twice   In order to evaluate the reproducibility of the methodology, we run the ROI registration two times on the same scan, for five subjects. We then evaluate the reproducibility of the method for the 5 scales by computing the Pearson correlation coefficient between the connection matrices resulting from the double processing of the same data set. The Pearson correlation coefficient is expressed as follows:

$$R(x,y) = \frac{\sum_i (x_i - \bar{x})(y_i - \bar{y})}{\sqrt{\sum_i (x_i - \bar{x})^2 \sum_i (y_i - \bar{y})^2}}, \; i = \left\{1, ..., N^2\right\}, \tag{4.2}$$

where $x = \{x_i\}$ and $y = \{y_i\}$ are the elements of both matrices.

We see in Table 4.1 that the matrices resulting from the two independent processing are highly correlated, since the correlation coefficients range between 0.998 and 0.978 on average depending on the resolution of the matrix. The correlation decreases with the increasing number of ROIs, which can be expected since the precision of the segmentation and cortical ribbon fitting is limited and the resulting errors are more strongly perceptible on small ROIs.
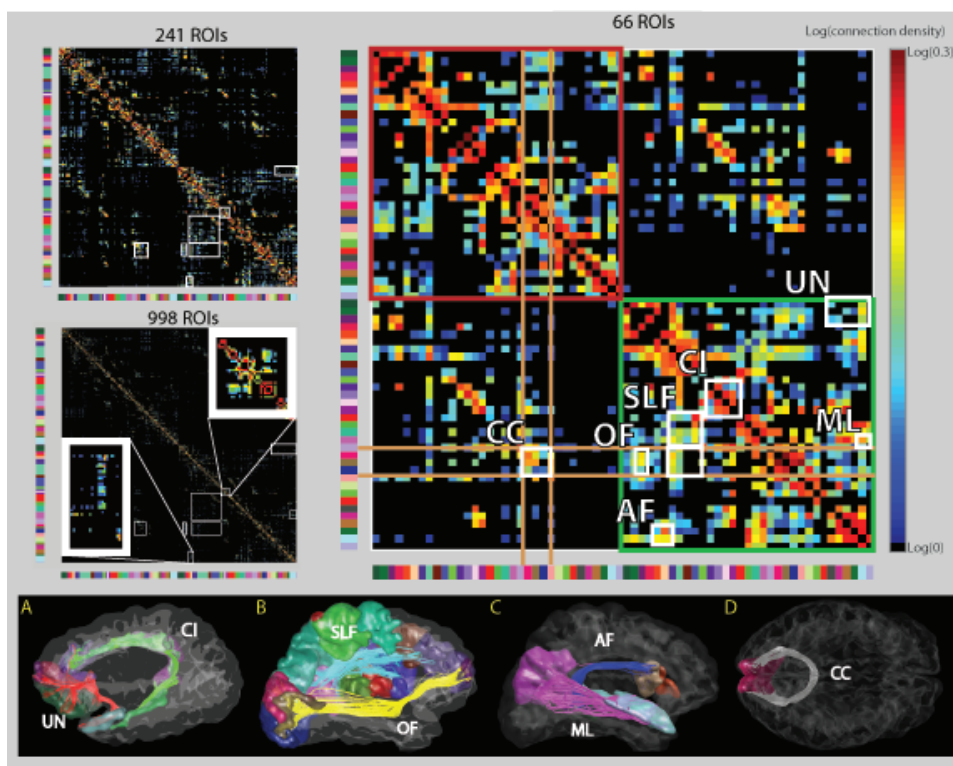
Figure 4.5: Identification of various fiber bundles on the different connection matrices. The identified bundles are: Cingular (CI) and Uncinate (UN) (A), Superior Longitudinal Fasciculus (SLF) and Occipito-frontal (OF) (B), Arcuate Fasciculus (AF) and Middle Longitudinal (ML) (C), and Cuneus homotopic connection (CC) (D). These bundles are represented on all the matrices.

	ROIs				
Subject	66	133	241	483	998
1	0.9991	0.9977	0.9952	0.9892	0.9816
2	0.9987	0.9952	0.9912	0.9850	0.9801
3	0.9978	0.9969	0.9933	0.9875	0.9803
4	0.9978	0.9958	0.9924	0.9875	0.9808
5	0.9969	0.9911	0.9858	0.9742	0.9653
average	**0.9981**	**0.9953**	**0.9916**	**0.9847**	**0.9776**

Table 4.1: The correlation coefficients between the connection matrices of the same scan processed twice, for five subjects. All the p-values are $\ll 0.001$.

			ROIs		
Subject	66	133	241	483	998
1	0.9738	0.9406	0.9025	0.8596	0.8145
2	0.9882	0.9704	0.9560	0.9408	0.9303
3	0.9590	0.9219	0.8970	0.8607	0.8389
4	0.9685	0.9459	0.9207	0.8964	0.8786
5	0.9881	0.9699	0.9498	0.9270	0.9079
average	**0.9755**	**0.9497**	**0.9252**	**0.8969**	**0.8740**

Table 4.2: The correlation coefficients between the connection matrices of the five subjects scanned twice. All the p-values are ≪0.001.

Same subject, scanned twice Given that additional perturbation factors related to the MRI acquisition need to be taken into account, such as noise, head positioning, susceptibility artifacts and head-coil sensitivity, five subjects were scanned a second time, about one month later, following the same protocol. These two scans are processed independently.

The Pearson correlation coefficients between the resulting connection matrices are calculated. The results presented in Table 4.2 show a high correlation ranging from 0.976 to 0.874, though slightly lower than in the previous section. This is expected since additional perturbation factors are introduced.

Robustness over several subjects When the Pearson correlations between all combination of connection matrices of the fifteen subjects are computed, we obtain values ranging from 0.68 to 0.79 for 998 ROIs, and between 0.90 and 0.97 for 66 ROIs. Figure 4.6 presents the correlation coefficients with respect to the scale. We also show on that plot the results of Tables 4.1 and 4.2.
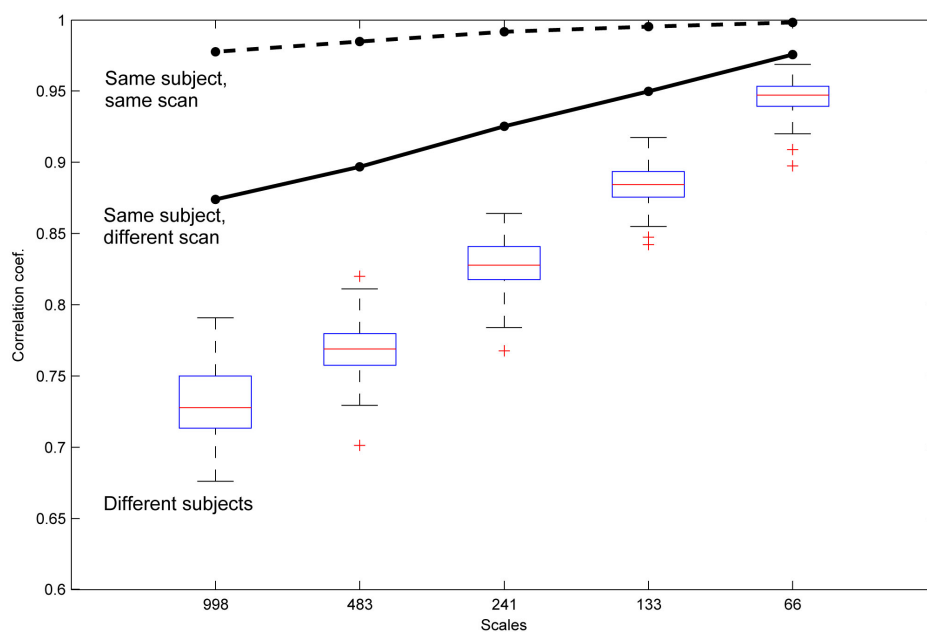
Figure 4.6: Intra-subject and inter-subject connection matrices comparison for each of the 5 scales. The dashed line shows the average correlation coefficients between the matrices of the five scans processed twice. The solid line shows the average correlation coefficients between the matrices of the five subjects scanned twice. The box plot presents the inter-subject's correlations.

4.6 Discussion

Over the last years it has become clear that MR based connectomic techniques are of the highest interest for the neuroscience community [33, 85]. The presented method is an answer to this growing interest. We step by step show how to partition the cortex in a standard way such that ROIs are identically placed across subjects. This allows the construction of whole-brain normalized connection matrices at multiple scales, which can be averaged and compared over population of subjects. It is worth noting that defining a connection matrix as presented here with a connection density measure, is only one way to characterize the connectivity. Other tract properties can be computed and used to construct the matrix, such as the Fractional Anisotropy, the Mean Diffusion, other values measured by MRI such as the T2 or the magnetization transfer ratio measured along the tracts, or even functional connectivity based on functional MRI.

The quantitative assessment of the performance of our methodology allows us to estimate what can and cannot be achieved. The level of correlation between two successive processing of the same scan is very high, which tends to indicate that our methodology is highly reproducible. The correlation coefficients for the two scans of the same subject may seem lower than what could be expected. However, we must not forget the level of complexity and the number of steps that are required to compute the connection matrix from the raw images. With this remark in mind, we see that the correlations between the two scans of the same subject with resolutions up to 133 or 241 ROIs are indeed high. This implies that in all likelihood, the optimal scales for point to point connectivity measurements are the right ones with the technology used. It is very likely that with expected improvement of cortical registration techniques and diffusion imaging, these numbers will significantly improve.

Depending on the study, going to smaller matrices might be beneficial because inter-subject correlation is higher. However, significant changes in connectivity may be lost due to large spatial averaging. On the other hand, using matrices that are too large may have as a consequence that the variability due to registration errors and MRI noise is larger than the effective connectivity difference between two groups. Nevertheless, it will be shown in Chapter 7 and 10 that even the highest resolution connection matrices have the capacity to be at the source of powerful analysis a) if one wants to study the connectivity in one single subject b) if connectivity has to be characterized through local and global network measures, in which case averaging occurs through the network measure itself. In conclusion, the right scale depends on the particular question being investigated. This is the reason why a multi-scale approach may be valuable.

The fact that the correlation coefficients between different subjects are systematically lower than the correlations between two scans of the same subject is not surprising. Indeed, different brains certainly exhibit differences in connectivity, which should be picked up by our matrices. But different brains are also folded differently, thus degrading the registration performance, inducing ROI misplacement and, accordingly, imprecise connectivity. Distinguishing between these two parameters will only be possible if in the future we manage to show significant differences between two groups. Actually, this normalized connection matrix opens up a whole range of clinical studies; either for longitudinal healthy development analysis such as the development of connectivity with age, or for the investigation of connectional disturbances in disease. Indeed, in many pathologies such as schizophrenia or epilepsy the connectivity in some specific bundles is suspected

to be affected, whereas inflammatory processes may affect connectivity more globally. To investigate this kind of pathologies, the connection matrix provides a promising tool to perform group versus group comparisons, if the differences in connectivity are expected to be in the same brain areas, or all over the brain.

4.7 Conclusion

In this chapter, we have proposed a multi-scale approach to map the connectome by constructing normalized whole-brain structural connection matrices derived from diffusion spectrum MRI tractography at five different scales. Using a template-based approach to bring cortical landmarks into register between different subjects and fully automating the post-processing steps necessary to build such matrices, we have proposed a robust method that allows a) the selection of identical cortical ROIs of desired size and location in different subjects with identification of the associated fiber tracts and computation of the related connection densities, b) straightforward construction and interpretation of anatomically organized whole-brain connection matrices and c) statistical inter-subject comparison of brain connectivity at various scales. The proposed framework is highly flexible, and can be modified depending on the application. For example, the anatomical parcellation used in this chapter could be replaced by any other parcellation, e.g. functional-based parcellation. Whereas we have used a deterministic tractography algorithm, more complex tractography approaches can be integrated in this framework, such as energy-minimization-based tractography algorithms, as it is shown in the next chapter.

Fast-marching Tractography for Connection Matrix (Fast-TraC)

5

5.1 Introduction

As we have seen in the previous chapters, diffusion MRI has been widely used to study brain anatomical connectivity because of its ability to probe the tissue microstructure [25]. For this purpose, the most common technique is probably the Diffusion Tensor Imaging (DTI) [14], which models the diffusion of water molecules as a second-order tensor. Since the discovery of DTI, there has been an increased interest in the development of tractography algorithms, inferring the trajectories of the axonal bundles directly from the diffusion measurements, and thus allowing the study of the fiber tract architecture (see Chapter 3 or [152] for review).

We can classify the tractography algorithms into two main types: the line propagation techniques and the energy minimization techniques. Among the line propagation techniques, we find the largely used deterministic approaches based on a step-by-step expansion of virtual fibers [50, 151], and the probabilistic approaches based on the modelling of the uncertainty associated with the local maxima of the diffusion [22, 96, 129, 159] (for more details see Chapter 3). If the deterministic algorithms are computationally simple, they are not able to accurately map complex fiber arrangements in DTI because of the low anisotropy found in fiber crossing areas, leading to a loss of directionality of the tensor [228]. Moreover they are very sensitive to noise, since it accumulates along the trajectory. The probabilistic approach, by characterizing the uncertainty in the main direction of the fibers, can partially solve the problem of fiber crossing areas, but is also affected by other issues such as partial volume effects or cumulative noise. Because of

these limitations, the scientific community has put a lot of effort into the development of global approaches, such as the energy minimization techniques.

The success of energy minimization techniques is mainly due to Parker et al. [160], who are among the first to have adapted Sethian's fast-marching algorithm [184] to tractography. This methodology is based on front propagations from seed voxels throughout the brain white matter, followed by a back propagation of the fibers using a gradient descent. It has given interesting results on well known tracts such as the pyramidal tracts, the optic radiations, and the anterior callosal fibers [46], and has shown to be more efficient than line propagation approaches in fiber crossing areas [198]. Recently, Jbabdi et al. [114] have proposed a tractography algorithm for DTI based on the anisotropic fast-marching technique, a modification of the standard fast-marching suited to perform front propagations in an anisotropic media [170].

Because DTI is based on the Gaussian model and thus can only map a single preferred direction in each imaging voxel, it fails to correctly map regions where the axons have more than a single preferred direction. In a recent work, Behrens et al. have estimated to one third the proportion of white matter voxels being affected by this problem [21]. In order to tackle this issue, higher angular resolution diffusion MRI methodologies have been designed, such as Q-ball [215] or spherical deconvolution [210]. Another interesting methodology is the diffusion spectrum imaging (DSI) [92, 226, 227] (see also Chapter 2), which allows to map the diffusion of water molecules by reconstructing the spectrum of the spin displacement. The scientific community has put a lot of effort into the search for the optimal tractography algorithm for DTI. Consequently, a lot of promising techniques have been proposed to compensate for the limitations of the DTI acquisitions. With the advent of DSI, we dispose of a technique that has the ability to resolve crossing fibers at the scale of a single voxel. By adapting classical deterministic tractography algorithms to DSI [89,95], complex fiber crossings regions have been accurately mapped with a precision that goes well beyond the possibilities of DTI data [182, 228]. However, the potential of these new high angular resolution data combined with the mathematical power of advanced energy minimization tractography algorithms should theoretically improve the accuracy of the results. Unfortunately, apart from some attempts [111, 158, 214], the adaptations of such techniques to DSI are still largely missing.

In this study, we propose an adaptation of the anisotropic fast-marching algorithm [170] to create a new tractography algorithm for DSI. We proceed by reducing the complexity of the orientation distribution function (ODF) in order to provide an analytical solution for the cost function used during the front propagation. We integrate the obtained tractography algorithm into the global framework allowing the creation of whole-brain connection matrices presented in Chapter 4. The resulting methodology is called Fast-marching Tractography for Connection matrix (Fast-TraC). After a short introduction on the anisotropic fast-marching, we make a step-by-step presentation of our Fast-TraC algorithm. Next, we compare the performance of Fast-TraC versus a classical deterministic approach, by analyzing several well-known fiber tracts. Finally, we discuss the influence and the choice of the algorithm parameters, and we analyze the advantages and shortcomings of the methodology.

5.2 Theory

Minimum-cost path problems

Minimum-cost paths problems are present in many applications such as geographic information systems, robotics or wire routing. A simple form of this problem is the case of a finite graph where a weight is assigned to every edge linking a pair of nodes. Finding the optimal path between two nodes can be solved using the well-known shortest path algorithm proposed by Dijkstra in 1959 [55]. This algorithm is still largely used for many applications, such as car's navigation systems or internet routing.

A typical minimum-cost path problem can be formulated as follows: it consists in finding a path $C(s)$ that minimizes the cumulative cost from a given starting point A to a given destination point B. Let us consider for a while the case where the cost τ only depends on the position $\mathbf{x}$ in the space. In this configuration, the minimal cost at $\mathbf{x}$ is given by:

$$u(\mathbf{x}) = \min \int_0^L \tau(C(s))ds, \qquad (5.1)$$

with L the length of the path connecting the starting point A to $\mathbf{x}$. The minimum of the integral has to be found among all the possible paths connecting A to $\mathbf{x}$. The path that minimizes the integral is the minimum-cost path. The solution of Equation 5.1 satisfies the Eikonal equation $\|\nabla u\| = \tau$, which describes a front propagation with a speed given by $1/\tau(\mathbf{x})$. $u(\mathbf{x})$ is therefore often called the arrival time. In order to compute $u(\mathbf{x})$, Sethian developed the fast-marching algorithm, a single-pass technique based on the Dijkstra algorithm [184, 185].

Fast-Marching algorithm

The fast-marching algorithm relies on a front propagation principle. The idea consists in dividing the grid nodes into three categories: the accepted set, the trial set and the far set, as depicted in Figure 5.1. The accepted set contains all the grid points for which the value $u(\mathbf{x})$ is determined and will not be changed. The trial set contains the grid points to be examined, whose u-values have already been computed. All the other points are in the far set. The algorithm works as follows. First, the starting point $\mathbf{x}_0$ is put in the trial set, with $u(\mathbf{x}_0) = 0$, and all the other grid points are put in the far set. Then, at each iteration, the trial point with the smallest u-value is put in the accepted set, all its neighbors are put in the trial set (if it was not already the case) and their u-values are computed (or updated if they were already in the trial set). The process ends when all the grid points are in the accepted set. This algorithm is summarized below.
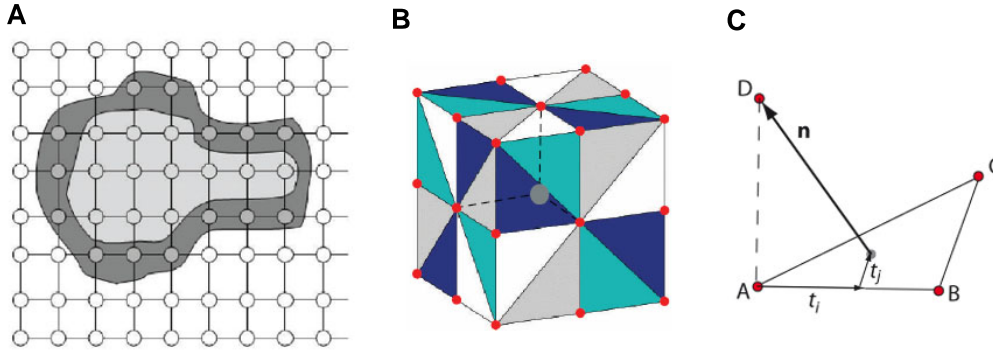
Figure 5.1: A: Principle of the fast-marching algorithm. The voxels are divided into three categories during the front evolution: the accepted points for which the u-value is determined (light gray), the trial points that are examined (dark gray) and the far points (white). B: The 48 triangles surrounding a specific grid point (central grey dot). Each red dot is a neighboring grid point. C: For each triangle ABC the values of t_i and t_j that minimize $u_{ABC}(D)$ have to be found. Part A and B are reproduced from [114].

The fast-marching algorithm

- Initialization:

    - Put the starting point $\mathbf{x}_0$ in the trial set, with $u(\mathbf{x}_0) = 0$;
    - Put all the other points in the far set;

- Loop:

    - Move the trial point with the smallest u-value, $\mathbf{x}_m$, into the accepted set;
    - Update the u-value of all the neighbors of $\mathbf{x}_m$ that belong to the trial set;
    - Put all the neighbors of $\mathbf{x}_m$ that belong to the far set into the trial set and compute their u-value;

As the reader might expect, the key step in the front evolution is the computation of the u-value. Let us consider a grid point D for which we want to compute the u-value $u(D)$. The fast-marching is based on the assumption that the updating of $u(D)$ is restricted to the immediate neighbors of D. Considering a 26-voxel neighboring scheme, we notice that the minimal path can be coming from any of the 48 triangles depicted in Figure 5.1B. Let us denote by A, B and C the three vertices of one of these triangles, and let $u_{ABC}(D)$ be the u-value at point D for the minimum-cost path coming from the triangle ABC. The final u-value at point D, $u(D)$ is the minimum of $u_{ABC}(D)$ among all the set of grid points ABC such that these points are the vertices of one of the 48 neighboring triangles. In other words, finding $u(D)$ consists in computing $u_{ABC}(D)$ for each of the neighboring triangles and selecting the minimum value.

Let us now describe the computation of $u_{ABC}(D)$. Considering the triangle ABC depicted in Figure 5.1C, we define $u_{ABC}(D)$ as follows:

$$u_{ABC}(D) = \min_{t_i, t_j}((1 - t_i)u_A + (t_i - t_j)u_B + t_j u_C + \|\mathbf{n}\| \cdot \tau_{ABCD}) \qquad (5.2)$$

s.t.

$$t_j \geq 0, \quad t_i \geq t_j, \quad t_i \leq 1, \qquad (5.3)$$

with u_A, u_B, u_C the u-values at points A, B and C respectively, and $\mathbf{n}$ the direction vector. Considering a specific direction vector $\mathbf{n}$, the u-value is given by the sum of two components: the u-value of the origin point obtained by linear interpolation in the triangle (i.e. the weighted sum of u_A, u_B and u_C), and the cost τ_{ABCD} associated to the octant $ABCD$ weighted by the travelling distance $\|\mathbf{n}\|$. $u_{ABC}(D)$ is found by searching the parameters t_i and t_j that minimize this expression.

Diffusion MR data and fast-marching

Tractography can be seen as a minimum-cost path problem. Suppose that diffusion MR data are used to define a cost function τ on a three-dimensional Cartesian grid. The aim of tractography consists in finding a path $C(s)$ that minimizes the cumulative cost from a given starting point A to a given destination point B. The problem is thus similar to the typical minimum-cost path problem presented above. However, since diffusion MR data contains orientational information, one would expect the cost function τ to be not only dependent on the location $C(s)$, but also on the direction $C'(s)$. In that case, the minimal cost has to modified as follows:

$$u(\mathbf{x}) = \min \int_0^L \tau(C(s), C'(s))ds. \qquad (5.4)$$

Unfortunately, solving Equation 5.4 is much more difficult than solving Equation 5.1. Indeed, the classical fast-marching algorithm is not able to use directly the orientational information. An ordered upwind method was proposed by Sethian to compute numerical solutions [186]. However, this method is computationally very expensive and can therefore not be applied to complex problems such as 3D tractography. Recently, Qingfen presented a modification of the fast-marching algorithm called the anisotropic fast-marching [170], which provides a good approximation to the exact scheme proposed by Sethian while being computationally more efficient.

Front evolution with the anisotropic fast-marching algorithm

The anisotropic fast-marching relies on the same front propagation principle as the classical fast-marching approach. The process is rigourously identical, and it also relies on the assumption that the updating of $u(D)$ is restricted to the immediate neighbors of D. The only difference is that the cost function depends not only on the position, but also on the orientation. Consequently, Equation 5.2 has to be modified as follows:

$$u_{ABC}(D) = \min_{t_i, t_j}((1 - t_i)u_A + (t_i - t_j)u_B + t_j u_C + \|\mathbf{n}\| \cdot \tau_{ABCD}(\mathbf{n})). \qquad (5.5)$$

We can see that the updating cost results from the product of the norm of $\mathbf{n}$ and the value of the cost function for this direction, $\tau_{ABCD}(\mathbf{n})$.

Choice of the cost function

In both the classical and anisotropic fast-marching algorithms, the choice of the cost function is crucial for several reasons. First, it defines the relation between the measurement (e.g. the diffusion in the case of tractography) and the evolution of the front and is therefore a key parameter. Second, with the anisotropic fast-marching algorithm the minimization of Equation 5.5 usually has to be solved iteratively by exploring the set of parameters $\{t_i, t_j\}$. However, by choosing particular cost functions, it is sometimes possible to find an analytical solution to the minimization problem, thus dramatically reducing the computational cost. One of these cost functions is presented in Section 5.3.

Back propagation

Once the front evolution is achieved, it is possible to find minimum-cost paths between the starting point and any other point reached by the front. In classical fast-marching methods, this can be performed by a gradient descent through the time of arrival map u [185]. In the anisotropic case, there is no guarantee that the characteristic direction coincides with the gradient direction, although a one-to-one mapping can be found for strictly convex speed profiles. However, the gradient descent is often used in practice since it provides reasonable solutions.

   In this work, we follow a slightly different approach, as proposed in [15, 160]. When a point is put in the accepted set, the direction **n** that gives the minimal u-value is stored. The resulting vector field is then used as an approximation of ∇u.

5.3   Methods

The proposed tractography algorithm is integrated in the methodology proposed in Chapter 4. After a description of the material and a brief summary of the steps leading to the creation of the connection matrix, we focus on the adaptation of the anisotropic fast-marching algorithm for tractography.

Material

After written informed consent and in accordance with our institutional guidelines and ethics committee, a healthy right-handed male volunteer was scanned with a Siemens TimTrio 3T scanner. A diffusion weighted single shot spin echo EPI sequence was used with TR = 6000 ms, TE = 136 ms and a maximal b-value of 8000 s/mm^2. Q-space was sampled over a hemisphere using 258 different encoding gradients, and the data were reconstructed following a classical DSI scheme [226] (see Section 2.6), producing a 3D diffusion probability density function (pdf) in every voxel. The acquisition block was made of 34 slices of a 96 x 96 matrix, with a spatial resolution of 2.21 x 2.21 x 3 mm^3. The acquisition time was approximately 26 minutes. Next, in each voxel the diffusion data were reduced into the ODF (see Section 2.6). In addition, a high-resolution T1-weighted (MP-RAGE) MRI was performed in a matrix of 256 x 256 x 128 voxels of isotropic 1mm resolution. This acquisition was then registered on the diffusion images using an affine registration method [192, 230] (http://www.fmrib.ox.ac.uk/fsl/).
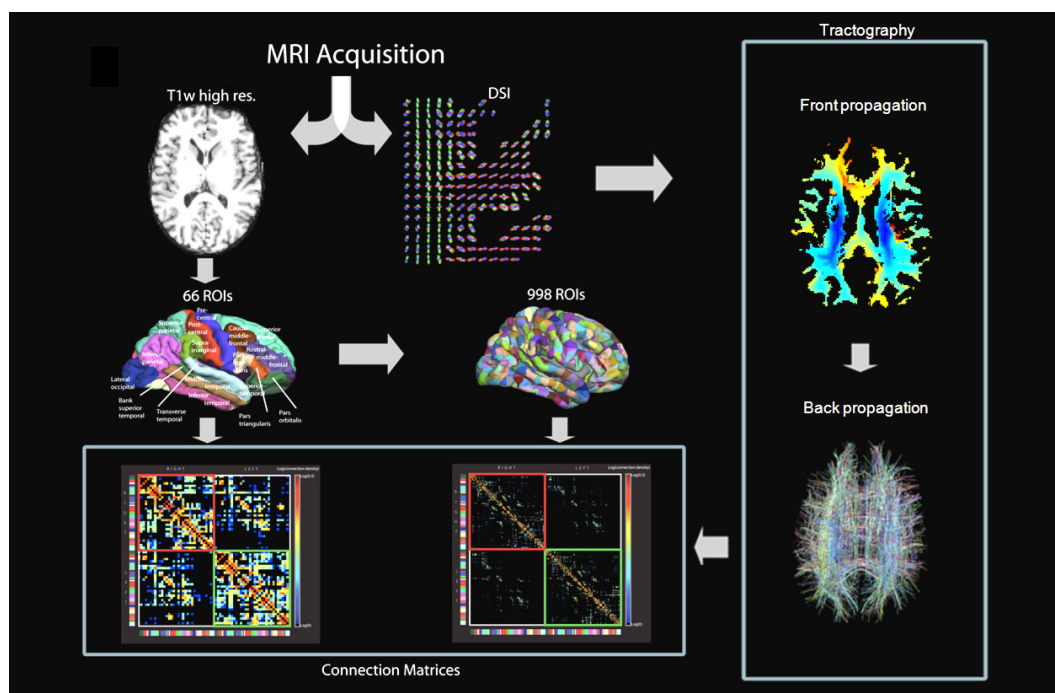
Figure 5.2: Overview of the Fast-TraC methodology. First, the diffusion MR and high-resolution T1-weighted images are acquired. Next, the cortex is partitioned into small ROIs. Then, tractography is performed in the brain WM, using an anisotropic fast-marching algorithm. Finally, the connection matrices are created using the results of the two previous steps.

Whole-brain tractography process

As already mentioned, the Fast-TraC algorithm benefits from the recent developments on the connection matrices (see Chapter 4), and therefore the methodology is very similar, as shown in Figure 5.2. First, the diffusion MR images are acquired using a typical DSI scheme and processed in order to obtain an ODF in every WM voxel. Then, we use the high-resolution T1-weighted acquisition to identify and partition the cortical surface into small regions of interest (ROIs). We remember from Section 4.2 that this partitioning is based on an atlas-based cortical registration method using the curvature information, i.e. sulcus and gyrus [36, 54, 61], which provides an automatic labelling of the cortex into 66 gyral-based parcels. By a recursive subdivision of these parcels, the cortex is then partitioned into 998 small ROIs, compact and of similar surface (approx. 150mm^2). Note that in this study we only use the lowest (66 ROIs) and highest (998 ROIs) resolutions. Moreover, we label the brainstem, the deep gray nuclei such as the putamen, globus pallidum, caudate and accumbens nuclei, the hippocampus, the amygdala and the thalamus. Those structures are identified by using Freesurfer's subcortical segmentation tools [62]. Next, tractography is performed using the anisotropic fast-marching algorithm (the detailed procedure is described in the following). Finally, the resulting fibers are used to build connection matrices representing the density of connection between every pair of ROIs.
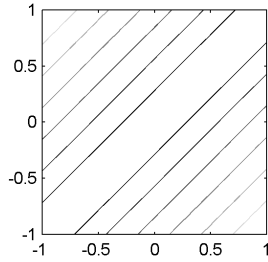
Figure 5.3: Two-dimensional iso-curves of arrival time for the cost function defined by Equation 5.6 and characterized by a single local maxima whose direction is (1,1).

Tractography using the anisotropic fast-marching

Cost function   In order to find a convenient cost function, we have to take two precautions with our diffusion data. First, we use a shifted grid (from a half-unit) for the diffusion data relatively to the front evolution grid [170]. Indeed, if the diffusion data and the front evolution were defined on the same grid, then the path from the triangle ABC to the point D (see Figure 5.1C) would cross at least two different voxels, resulting in a variable speed along the path. The shifted grid allows to solve this problem and ensures that the speed along a given direction is constant inside the volume $ABCD$. Second, we reduce the ODF of each voxel into a set of normalized vectors $\{\mathbf{s_1}, ..., \mathbf{s_N}\}$ corresponding to the local maxima of the ODF. That way, the orientational information contained in the ODF is preserved, and the search for analytical solutions is tremendously simplified.

We propose the following cost function:

$$\tau_{ABCD}(\mathbf{n}) = \min_i \left(\frac{\|\mathbf{n} \times \mathbf{s_i}\|}{\|\mathbf{n}\|} \right), \tag{5.6}$$

with $\mathbf{s_i}$ being the i-th local maxima of diffusion in the voxel that contains the volume $ABCD$. From Equation 5.6, we understand that if the direction $\mathbf{n}$ is collinear to one of the local maxima of the diffusion, the cost is zero, ensuring a fast propagation of the front along that direction. On the other hand, the higher the angle between the direction and the local maxima and the higher the cost, and consequently the slower the evolution of the front. Consequently, this cost function is particularly well suited for tractography. As an illustration, Figure 5.3 shows the iso-curves of arrival time in the case of a single local maxima. Theoretically, there exist a lot of other cost functions with a similar behavior. However, this one provides us with an analytical solution to the minimization problem, as explained in what follows.

Suppose for a while that we are located in a voxel where there is a single local maxima of diffusion, $\mathbf{s}$. When $\tau_{ABCD}(\mathbf{n})$ is inserted in Equation 5.2, we obtain:

$$u_{ABC}(D) = \min_{t_i, t_j} ((1 - t_i)u_A + (t_i - t_j)u_B + t_j u_C + \|\mathbf{n} \times \mathbf{s}\|). \tag{5.7}$$

Considering Figure 5.1C, we can express the vector $\mathbf{n}$ as a function of the parameters t_i and t_j, as follows: $\mathbf{n} = (-t_i, -t_j, 1)$. Equation 5.7 thus becomes:

$$
u_{ABC}(D) \quad = \quad \min_{t_i, t_j}((1 - t_i)u_A + (t_i - t_j)u_B + t_j u_C +
$$

$$
+\sqrt{(t_j s_3 + s_2)^2 + (t_i s_3 + s_1)^2 + (t_i s_2 - t_j s_1)^2}), \tag{5.8}
$$

s.t.

$$
t_j \geq 0, \quad t_i \geq t_j, \quad t_i \leq 1, \tag{5.9}
$$

with $\mathbf{s} = (s_1, s_2, s_3)$. In the space of parameters $\{t_i, t_j\}$, the function to minimize is the sum of a plane (the weighted sum of u_A, u_B and u_C) and a revolution cone (the norm of the vectorial product of $\mathbf{n}$ and $\mathbf{s}$) whose orientation is given by $\mathbf{s}$. Therefore, it is a convex function, and two cases have to be considered: the case where the apex of the revolution cone is located inside the triangle ABC (see Figure 5.4A), and the case where it is located outside the triangle ABC (see Figure 5.4B). In the first case, we are sure that the minimum is found precisely at the apex of the revolution cone, with coordinates $(-s1/s3, -s2/s3)$. In the other case, the minimum can be located either at the vertices A, B and C, or along the edges AB, BC and AC. For the edges, the coordinates of the potential minimum points can be computed by using the partial derivatives of the expression to minimize with respect to t_i and t_j. In the case of the edge AB, we have to solve:

$$
\begin{cases}
-u_A + u_B + \dfrac{t_i s_3^2 + s_1 s_3 + t_i s_2^2 - t_j s_1 s_2}{\sqrt{(t_j s_3 + s_2)^2 + (t_i s_3 + s_1)^2 + (t_i s_2 - t_j s_1)^2}} = 0 \\
t_j = 0
\end{cases} \tag{5.10}
$$

Similarly, The coordinates along the edges BC and AC are found by solving the systems of equations 5.11 and 5.12, respectively.

$$
\begin{cases}
-u_B + u_C + \dfrac{t_j s_3^2 + s_2 s_3 + t_j s_1^2 - t_i s_1 s_2}{\sqrt{(t_j s_3 + s_2)^2 + (t_i s_3 + s_1)^2 + (t_i s_2 - t_j s_1)^2}} = 0 \\
t_i = 1
\end{cases} \tag{5.11}
$$

$$
\begin{cases}
-u_A + u_B + \dfrac{t_i s_3^2 + s_1 s_3 + t_i s_2^2 - t_j s_1 s_2}{\sqrt{(t_j s_3 + s_2)^2 + (t_i s_3 + s_1)^2 + (t_i s_2 - t_j s_1)^2}} = 0 \\
t_i = t_j
\end{cases} \tag{5.12}
$$

In Table 5.1, we report the coordinates of the seven possible solutions to Equation 5.8. Note that the coordinates of the points corresponding to the other triangles can be found by some index and sign permutations.

Finally, the computation of $u_{ABC}(D)$ is a four-step process, as follows: (i) compute the coordinates of the potential minimum points, (ii) keep only the points whose coordinates satisfy condition 5.9, i.e. those that are located into the triangle ABC, (iii) compute the u-value for each of these points, and (iv) select the minimum. The extension to multiple local maxima of diffusion is straightforward: the process is repeated for every local maxima and the minimum is selected among all the computed u-values.
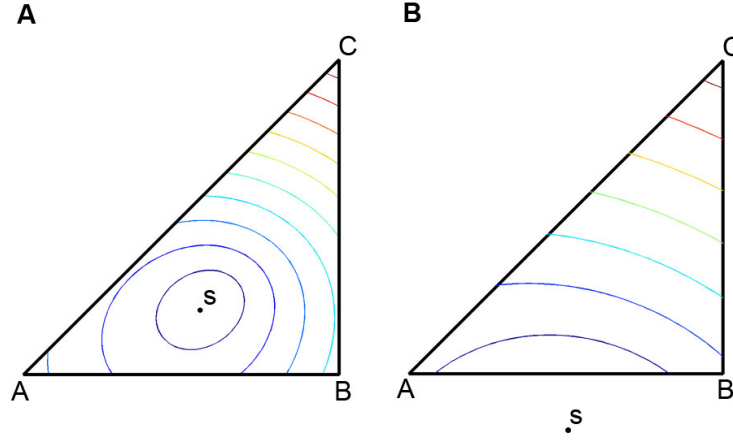
Figure 5.4: Iso-curves of $u_{ABC}(D)$ using the expression defined in Equation 5.8. A: the apex of the revolution cone is located inside the triangle ABC. The minimum of $u_{ABC}(D)$ under condition 5.9 is thus located at s. B: the apex of the revolution cone is located outside the triangle ABC. The minimum of $u_{ABC}(D)$ has to be searched along the edges AB, BC and AC or at the vertices A, B and C.

ABC	$t_i = -\frac{s_1}{s_3}$	$t_j = -\frac{s_2}{s_3}$
AB	$t_i = \frac{1}{1-s_1^2}\left(-s_1 s_3 + \frac{(u_A - u_B)|s_2|}{\sqrt{1-s_1^2-(u_A-u_B)^2}}\right)$	$t_j = 0$
BC	$t_i = 1$	$t_j = \frac{1}{1-s_2^2}\left(s_2(s_1 - s_3) + \frac{(u_B - u_C)|s_1+s_3|}{\sqrt{1-s_2^2-(u_B-u_C)^2}}\right)$
AC	$t_i = t_j = \frac{1}{2s_3^2+(s_2-s_1)^2}\left(-s_3(s_1+s_2) + \frac{(u_B-u_C)|s_1-s_2|}{\sqrt{2s_3^2+(s_2-s_1)^2-(u_B-u_C)^2}}\right)$	
A	$t_i = 0$	$t_j = 0$
B	$t_i = 1$	$t_j = 0$
C	$t_i = 1$	$t_j = 1$

Table 5.1: Solutions to Equation 5.8 corresponding to points located inside the triangle ABC, along the edges AB, BC and AC and at the vertices A, B and C. Those solutions are valid for the triangle depicted in Figure 5.1C. The solutions for the other triangles are obtained by index and sign permutations.

Front evolution Ideally, one should be tempted to start a front evolution from every voxel of the cortex in order to have a high spatial resolution. However, in practice this approach is not adequate because of the extreme amount of computation time it would require. Therefore, we decide to perform a front evolution from every ROI of the high-resolution connection matrix (approx. 1000 front evolutions). The voxels belonging to the ROI are all considered as starting points, i.e. their u-value is zero.

The front evolution is limited to WM voxels only, so that we ensure that no propagation is done in restricted areas such as the ventricles. The front evolution is also admitted in the voxels of the cortex if the front comes from the WM. However, no propagation is allowed from GM voxel to GM voxel, in order to prevent minimum-cost paths travelling inside the cortex. We introduce two parameters that limits the evolution of the front: (i) the maximum deviation and (ii) the maximum curvature. The maximum deviation is the maximum cost admitted during the front evolution. It restricts the front evolution to regions where the cost is low. In practice, this parameter limits the partial volume effects by preventing the front to evolve in directions that strongly differ from the local maxima of diffusion. The maximum curvature checks for the coherence of the front evolution, as follows. When computing the minimal u-value for a given voxel D, we compare the associated direction vector **n** with the direction vectors already stored in the accepted neighbors A, B and C. If the angular deviation is higher than the maximum curvature threshold, the u-value corresponding to the triangle ABC is not computed. This parameters prevents the front evolution to perform abrupt changes of direction, which (i) limits the partial volume effects and (ii) generates a smooth gradient map and consequently smoothed fiber trajectories. Another advantage of these parameters is that when correctly adjusted, they limit the number of cortex voxels reached by the front, thus providing a more realistic map of brain connectivity.

Fiber generation by back propagation For each front evolution, we perform the back propagation of the fibers, as follows. We initialize one fiber per voxel of the cortex reached by the front. The fibers expand by a fixed step size (arbitrarily fixed to 0.5mm) along the directions stored during the front evolution until they reach the origin ROI. Fibers that do not reach the origin ROI are eliminated. We also introduce a curvature threshold, to prevent the abrupt changes of direction that may arise from partial volume effects. The set of fibers produced for all the front evolutions are then used to build the connection matrix, as described in Section 4.3.

5.4   Results

In this section, we compare the results of the Fast-TraC algorithm to those obtained with the streamline approach presented in Chapter 4. The comparison is based on the visual aspect of several well-known tracts of the brain, such as association fibers and projection fibers. Unless stated otherwise, the Fast-TraC results are obtained with the following parameters: maximum deviation: 0.6 (corresponding to a maximum angle of approx. 36°), maximum curvature: 36° and curvature threshold for back propagation: 36°/mm.
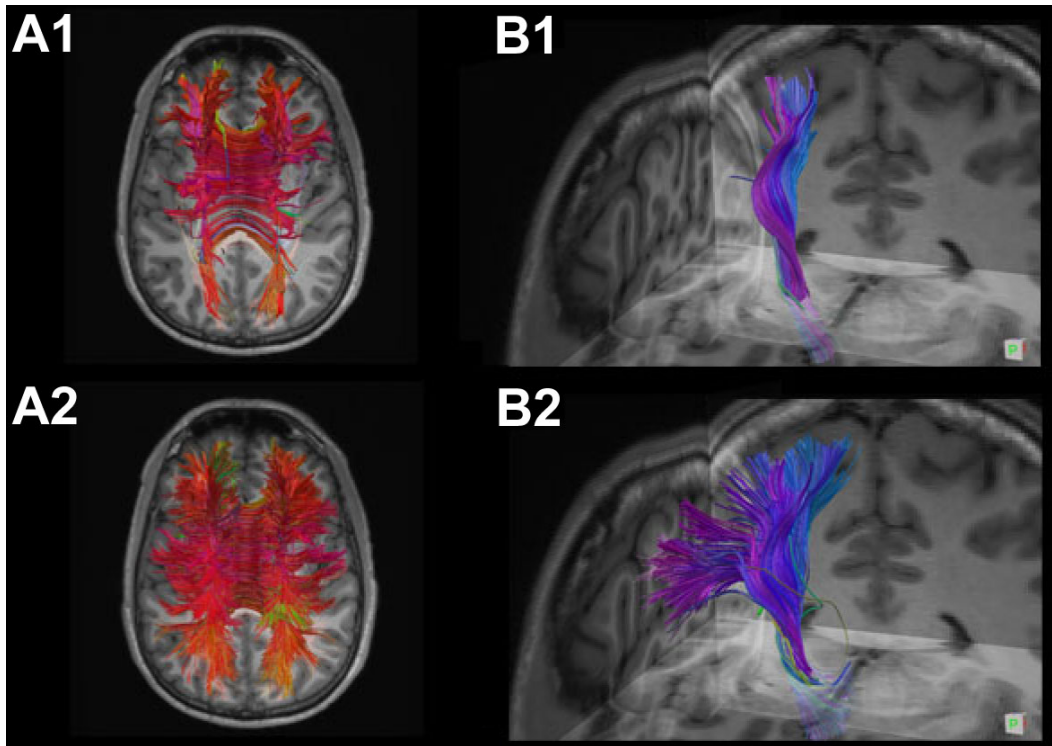
Figure 5.5: Corpus callosum fibers (A) and corticospinal tract (B) obtained with streamline (top) and Fast-TraC (bottom) algorithms.

The centrum semi-ovale

We start our analysis by focussing on two well-known and extensively investigated fiber tracts that cross in the centrum semi-ovale: the corpus callosum and the corticospinal tract.

Callosal fibers, presented in Figure 5.5A, are selected by placing a ROI in the midsagittal plane centered on the corpus callosum. With the Fast-TraC approach, the fibers of the corpus callosum are widely distributed throughout the parietal cortex from the apex down to its lower limit at the lateral sulcus. It also widely connects the frontal cortex. Using the streamline algorithm, only the apical part of the parietal cortex is connected. This is mainly due to the region of the centrum semi-ovale where a complex fiber intermixing occurs between the corticospinal tract and the corpus callosum. In such structurally complex areas, classical deterministic approaches are unable to accurately reconstruct trajectories. The Fast-TraC approach overcomes this limitation by a better exploitation of the information contained in the DSI data.

The corticospinal tract (Figure 5.5B) is mapped by capturing the fibers running through the internal capsule and ending in the precentral gyrus. For this bundle, the parameters of the Fast-TraC algorithm are adapted to take into account the higher curvature of the tract ($45°$ is used instead of $36°$). The streamline approach allows to map only the connections that take their origin between the superior and inferior genu of the central sulcus, corresponding to the motor fibers for the arm and hand. Again, this is due to the complex crossing which occurs in the centrum semi-ovale. In contrast, with
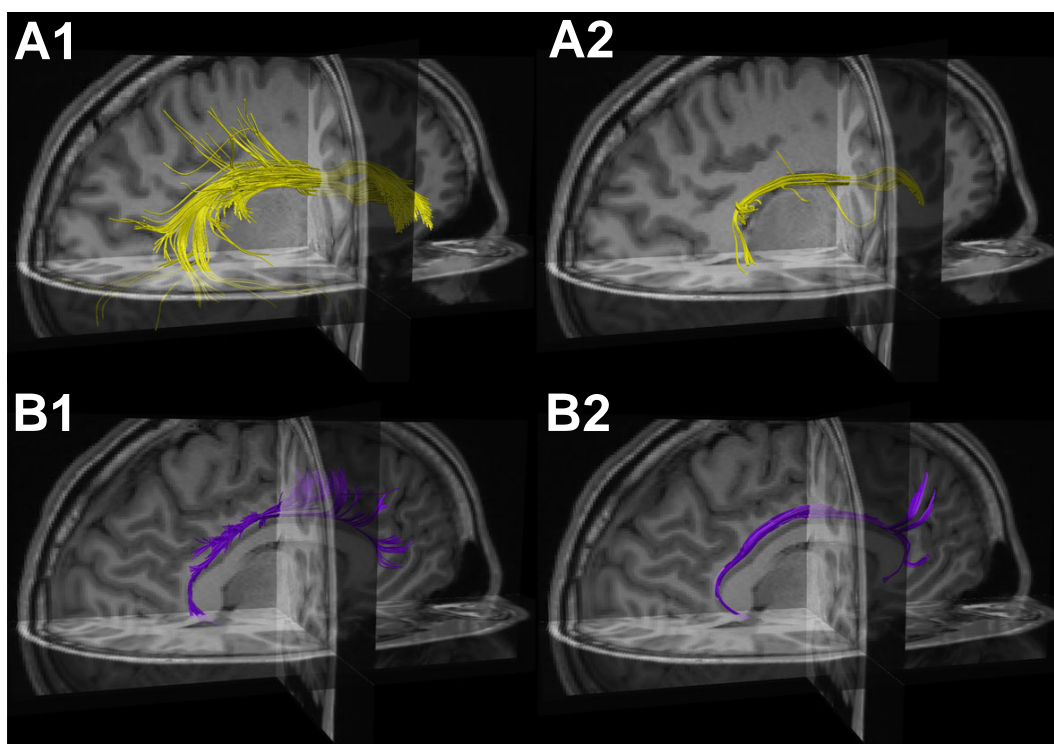
Figure 5.6: Association bundles obtained with Fast-TraC (left) and streamline (right) algorithms: A: arcuate fasciculus and B: cingulum bundle.

the Fast-TraC approach the part of the pyramidal tract starting in the apical part of the precentral gyrus and middle part of the paracentral lobule, corresponding to the motor function of the trunk and legs, becomes visible. Similarly, the more lateral projections corresponding to the motor function of the head and the mouth are well mapped.

Association fibers

Five major association bundles are captured by both the streamline and the Fast-TraC algorithms: the arcuate fasciculus, the cingulum bundle, the extreme capsule, the inferior longitudinal fasciculus and the uncinate fasciculus, as depicted in Figures 5.6 and 5.7 [183]. The arcuate fasciculus (Figure 5.6A) is extracted by selecting fibers originating from pars triangularis and ending in the superior temporal gyrus. The cingulum bundle is obtained by capturing fibers running through the cingulum gyrus (Figure 5.6B). For this bundle, the parameters of the Fast-TraC algorithm are adapted to take into account the higher curvature of the tract (45° is used instead of 36°). The extreme capsule (Figure 5.7A) connects the parietal and posterior temporal cortex with the frontal ventrolateral cortex and is obtained by selecting fibers running through a manually defined ROI in the extreme capsule. The inferior longitudinal fasciculus (Figure 5.7B) is obtained by selecting fibers originating from the inferior temporal gyrus and ending in the occipitoparietal junction (orange) or in the occipital lobe (blue). The uncinate fasciculus (Figure 5.7C) is extracted by selecting fibers connecting the temporal pole to the inferior frontal cortex.

For the cingulum bundle and the arcuate fasciculus, we can see that the streamline
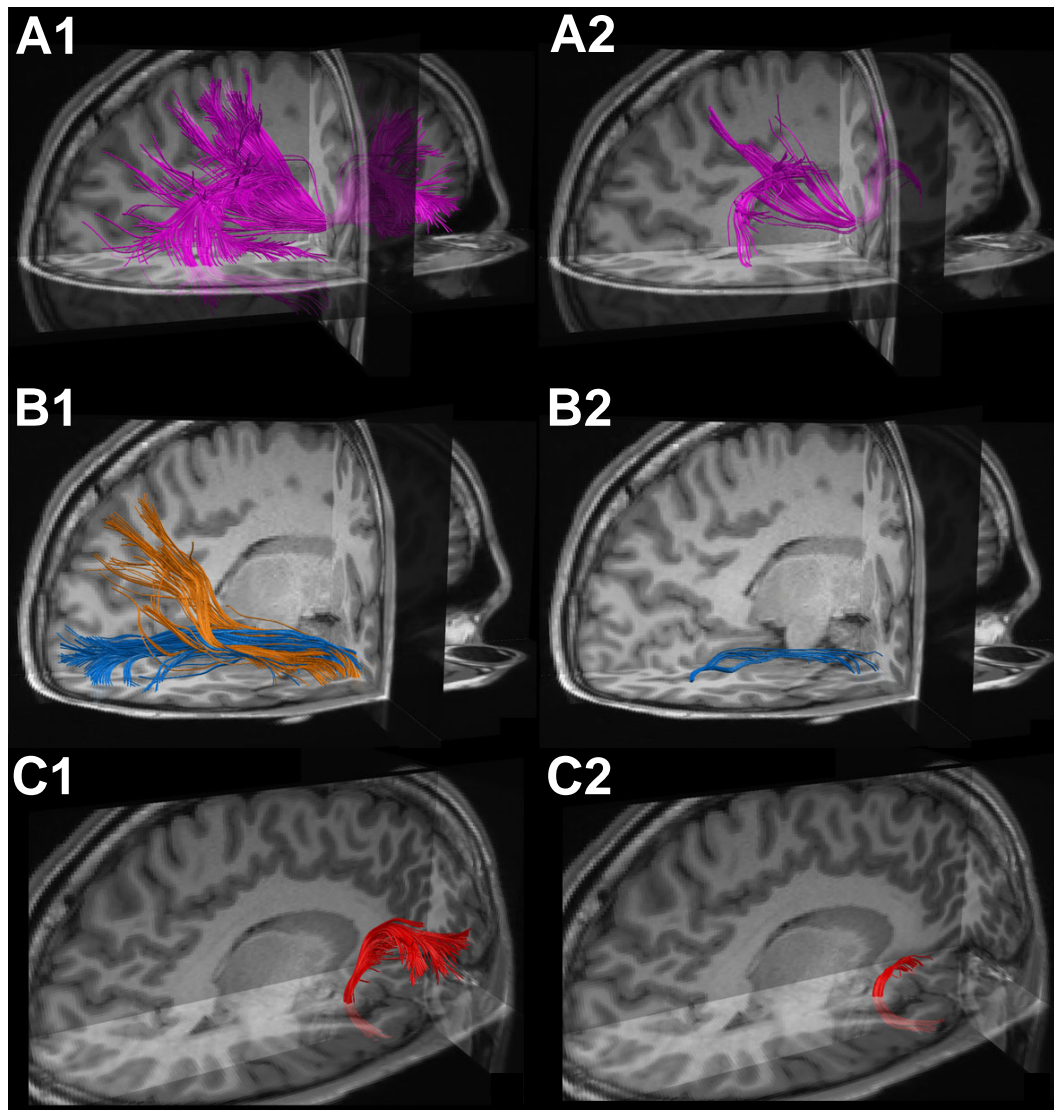
Figure 5.7: Association bundles obtained with Fast-TraC (left) and streamline (right) algorithms: A: extreme capsule, B: inferior longitudinal fasciculus and C: uncinate fasciculus.
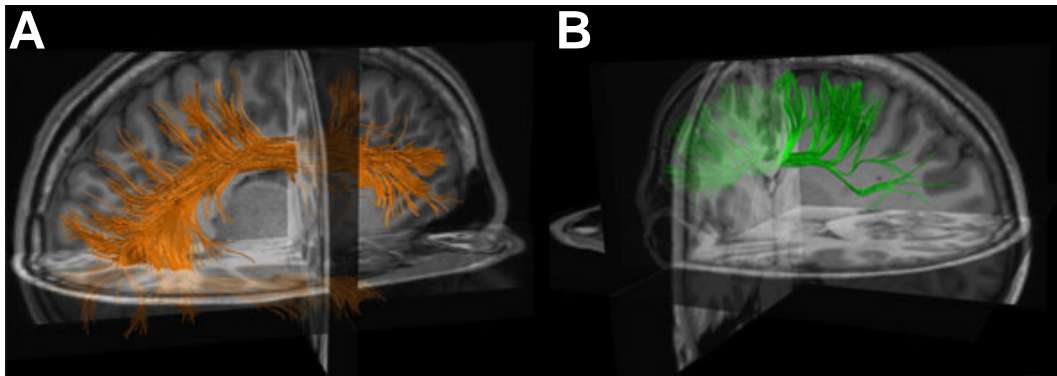
Figure 5.8: Association bundles obtained with Fast-TraC and not captured by the streamline algorithm: A: superior longitudinal fasciculus and B: fronto-occipital fasciculus.

approach is able to capture the global shape of the tract. The Fast-TraC algorithm shows similar bundles, although the fibers are more widely spread throughout the origin and destination regions. For the extreme capsule however, the streamline approach fails to map most of the projections of the parietal and ventrolateral cortices. The result obtained with the Fast-TraC approach is much more convincing. This difference is particularly striking when considering the inferior longitudinal fasciculus and the uncinate fasciculus. For the inferior longitudinal fasciculus, the streamline algorithm provides us with only a partial representation of the horizontal limb (blue), whereas both the horizontal and vertical limbs are well captured with Fast-TraC. The uncinate fasciculus mapped with the streamline algorithm presents a hooked shape which projects to the lateral orbital frontal cortex only, whereas with Fast-TraC additional projections are found in the inferior frontal cortex (pars opercularis, pars triangularis and pars orbitalis).

In addition, the Fast-TraC approach allows us to map two association bundles that are not captured by the streamline approach. The superior longitudinal fasciculus II (Figure 5.8A) connects the inferior parietal lobule with the middle frontal gyrus through the centrum semi-ovale. The fronto-occipital fasciculus (Figure 5.8B) is obtained by selecting fibers originating from the medial parieto-occipital lobe and ending in the superior frontal gyrus. The classical deterministic approaches usually fail to map these tracts because they run through large fiber crossing regions. In these conditions, a more complex method is required to accurately perform tractography. These results demonstrate the high potential of the Fast-TraC approach to map fiber tracts in complex fiber crossing areas. It is however important to note that these observations are based on a single subject study, and that further work has to be done in order to check whether the mapping of these tracts is systematic.

5.5 Discussion

The method proposed in this work provides two main advantages compared to the fast-marching tractography proposed in [160]. First, Parker et al. used a standard fast-marching process, which is inherently limited to front propagations with an isotropic cost function. The use of such a technique for tractography is however not intuitive, since the tractography process is essentially based on the orientational information contained

in the diffusion MR data. In order to overcome this limitation, Parker et al. proposed to integrate the orientational information in a location-dependent only cost function using some computational hacks. Here we propose a different approach based on the anisotropic fast-marching algorithm, which is suited to perform front evolutions with an anisotropic cost function. The integration of the orientational diffusion information in the cost function is therefore straightforward, and provides us with an elegant solution for the front propagation in the brain white matter. Second, the method proposed by Parker et al. is restricted to diffusion tensor imaging. In contrast, the Fast-TraC is based on the main directions of diffusion, and can therefore be used with any diffusion MR technique without modification of the methodology. The only requirement consists in extracting the local maxima of diffusion from the measurements prior to tractography.

As mentioned earlier, with such a fast-marching approach it is theoretically possible to find a path between any pair of ROIs. However, we know from anatomical and tracing studies that only a small proportion of these connections exists. Therefore, there is a great need for automated selection methods that only retain the most probable connections. In this work, we propose a three-step automated selection method. First, the maximum deviation criterion ensures that the front propagates in directions that are close to the local maxima of diffusion. Indeed, several studies have shown that we can be relatively confident in the diffusion measurements (see for example [182]). The maximum deviation criterion is therefore chosen such that the uncertainty associated to the main directions of diffusion is minimal. Second, the maximum curvature threshold prevents the front to perform abrupt changes of direction, that would not correspond to the real axonal trajectories in the brain. Third, an additional curvature threshold is included in the back propagation process. At first sight this parameter may seem useless since we already control for the smoothness of the front evolution. However, we remember that the back propagation is a discrete process. Due to the fixed step size of the fibers, the trajectory may slightly deviate from the optimal path, which can potentially lead in abrupt changes of direction. This third criterion thus ensures that the fibers generated by the back propagation are smooth.

The Fast-TraC algorithm is among the first energy minimization-based tractography approaches to be applied to DSI. As expected, it provides us with enhanced tractography results as compared to classical deterministic tractography approaches. This is due to the fact that the energy minimization-based techniques consider the uncertainty associated with the local maxima of diffusion through the choice of an adequate cost function. In contrast, the streamline approach only consider the measured local maxima, without estimation of the associated uncertainty. Consequently, the tractus already mapped with the streamline tractography are better defined with Fast-TraC. This is particularly striking for the corticospinal tract, for which the entire range of projections are captured, from the apex down to the lateral sulcus. Moreover, it allows us to investigate the trajectory of fiber tracts that can not be captured with the streamline approach, due to the presence of complex fiber crossings. This is the case for the superior longitudinal fasciculus, the fronto-occipital fasciculus and the vertical limb of the inferior longitudinal fasciculus. Further investigation will probably allow us to find other tracts that were never observed with conventional tractography techniques. Globally, we can say that the Fast-TraC algorithm provides a more complete and more convincing representation of the true axonal connectivity.

Furthermore, the Fast-TraC methodology has several advantages over classical trac-

tography approaches. First, it is based on a global energy minimization technique and is therefore less sensitive to noise in the diffusion MR data, as compared to a line propagation technique for which the noise accumulates along the computed trajectory. Second, its integration in the connection matrix framework provides us with an easy and fast way of selecting the desired fiber tracts. By having a simple look at the connection matrix and the associated cortex labelling, it is possible to select the tract connecting two particular ROIs. Third, depending on the application the parameters can be adjusted to provide the user with the desired level of brain connectivity. In this work, the default parameters are adjusted so that they are restrictive enough to limit the partial volume effects, while keeping a small amount of uncertainty in the orientation of the local maxima of diffusion. This set of parameters can be considered as a kind of fair compromise between these two aspects. By raising or lowering the maximum deviation threshold and/or the maximum curvature, it is possible to obtain more permissive or more restrictive tractography solutions.

However, we have to keep in mind that although the Fast-TraC has an increased sensitivity compared to line propagation techniques, it is at the cost of a decrease in specificity. Indeed, the energy minimization techniques are particularly sensitive to partial volume effects, which leads to the creation of aberrant fiber tracts resulting from the mixing of two or more distinct fiber populations. Although we introduce several criterions to reduce the partial volume effects, the produced tracts have to be interpreted with caution. In this work, we focus on well-known fiber tracts for which we have strong prior information about their existence and their trajectory. Therefore, the potential false positive tracts are suppressed manually by choosing the adequate ROIs. Unfortunately, for more general studies about brain connectivity these undesired trajectories are not systematically suppressed. There is therefore a great need for automated fiber selection methods aiming at increasing the specificity, that could be applied as a post-processing step after any tractography algorithm. However, the problem of fiber selection remains far from trivial and goes beyond the scope of this work.

5.6 Conclusion

In this chapter, we have presented a new energy minimization technique to perform tractography with DSI data, based on the anisotropic fast-marching algorithm. The presented results show an enhanced sensitivity compared to traditional tractography approaches. The high flexibility of the methodology, obtained through the adjustment of two front evolution parameters, allows to map the connectivity of the brain to any level of complexity. This can be seen as a contrast adjustment for the tractography solution. As any energy minimization technique, it is highly sensitive to partial volume effects, and thus requires some particular attention when interpreting the results.

Throughout the following chapters, we focus on the validation of the human connectome, as well as on its whole-brain applications. In this type of study, we have no prior information about the investigated connections. Consequently, the proposed approach is not directly applicable, since it would require a powerful and automated fiber selection method that is currently unavailable. Therefore, in the next chapters, we use a classical streamline algorithm instead.

Part II

Validation

Estimating the Confidence Level of WM Connections

6

6.1   Introduction

As seen in Chapter 3, the increased interest in Diffusion MRI has led to the development of various tractography algorithms, whose aim consists in inferring from the diffusion measurement the trajectories of the axonal bundles in the brain, allowing the study of the fiber tract architecture. However, diffusion MR data contain noise that systematically affects the tractography [8,142], regardless of the method used to generate fiber tracts. Angular and spatial resolution, brain shape and of course the MRI acquisition methodology, as well as the tractography algorithm itself, are potential sources of errors in the mapping of brain connectivity [37,89,137]. This immediately raises the question of validation of the results. There exist several approaches to address this difficult problem. First, the tractography algorithms can be tested on synthetic data, where all the parameters of the underlying model are known [142]. Another approach is to correlate the reconstruction of a small set of tracts with some gold standard methods [91,142,182]. These methods are nonetheless partial validation and therefore complementary studies which analyze other aspects of the problem, such as the reliability of computed white matter connections across the whole brain, are welcome. In this study, we address the following question: How do we know that a given tractography solution is a result of the underlying diffusion coherence and not of some other effect? Indeed, performing tractography on a data set with completely random and incoherent diffusion would produce many fibers that look improbable, but may also produce some fibers that, by chance or due to the brain geometry or a limited resolution, look "real". In this context, it is essential to identify and to quantify the source of error, not only for a specific tract, but for a whole-brain tractography experiment.

A straightforward way to tackle this issue is to evaluate the effects of noise on the

diffusion MR data. For example, several studies focus on the impact of noise on diffusion tensor eigenvalues, as well as on the derived fiber trajectories [8, 137, 143]. Others try to model the eigenvector dispersion by assuming various probability density functions [22, 159]. Another approach consists in measuring the uncertainty associated with the reconstructed fiber trajectories. Probabilistic algorithms particularly well suit this task, since they allow to assign a probability to the produced tracts, either by integrating a cost-function along the paths [214], or by counting the occurrence of the paths obtained using a Monte Carlo random walk [129, 160]. In contrast, deterministic algorithms suffer from the lack of information on the probability of the reconstructed trajectories. In [138], a bootstrap approach is proposed to estimate the dispersion associated with tractography results. Recently, this method was extended to use any deterministic tractography algorithm in a probabilistic way [118].

In this study, as in [118], we try to address the shortcomings of the deterministic approach. However, instead of transforming deterministic algorithms into probabilistic ones, we rather add some information about the reliability of the produced tracts. For this purpose, we present a method specifically aiming at differentiating connections likely to be built by diffusion coherence contrast from those potentially resulting from non-diffusion effects, such as noise, resolution or brain geometry. We proceed by comparing the fiber density of every connection with a set of equivalent connections generated in systems where diffusion coherence contrast is removed by randomly reshuffling the orientation distribution functions (ODFs). First, we study the statistical differences between connections in data sets with and without diffusion coherence contrast. We show that on an individual basis some connections are clearly different in the two types of data sets, while others cannot be differentiated. Then, we define a confidence level in order to quantify the difference between the data sets with and without diffusion coherence contrast. We show that the confidence level greatly varies from one connection to another. We analyze the factors responsible for this high variability and emphasize the fact that one cannot trust all fibers equally in tractography. Finally, we propose a method to reduce the computation time of the estimation of the confidence level, based on the apparent correlation between confidence level and connection distance. This methodology is expected to add useful information to any tractography study.

6.2 Material and Methods

This research was conducted in agreement with the ethics comity for clinical research of the University of Lausanne and informed written consent was obtained from the subjects before performing the study, in accordance with institutional guidelines. The proposed method consists of six steps, as described in Figure 6.1, and follows the method used in Chapter 4. First, we acquire the diffusion MR images and process them in order to get a map of the diffusion in the brain (A). Next, we perform the tractography in the brain white matter (WM) (B). Independently from the tractography solution, we partition the WM-gray matter (GM) interface, i.e., the cortex for simplification, into small regions of interest (ROIs) (C). Once these steps are performed, we build a graph in which every ROI of the WM-GM interface constitutes a node. If there are some fibers linking a pair of ROIs, we build an edge between the corresponding nodes of the graph. That way, we obtain a graph reflecting the connectivity of the brain, that we call graph of brain connectivity (D). Next, we use a similar procedure (steps B to D) to construct randomized versions
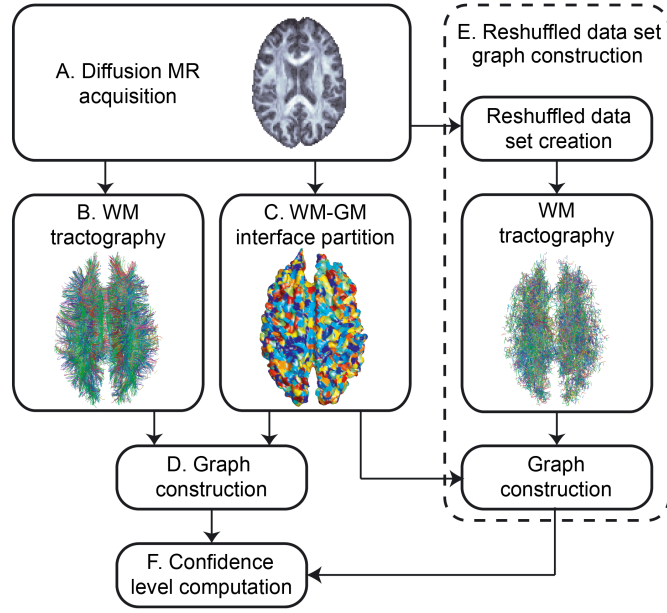
Figure 6.1: Overview of the whole process. (A) Acquisition of the diffusion MR images. (B) Tractography in the brain WM. (C) Partitioning of the WM-GM interface into small regions of interest (ROIs). (D) Creation of the original brain connectivity graph using the results of steps B and C. (E) Construction of randomized versions of the original brain connectivity graph (the same partition into ROIs is used). (F) Computation of the confidence level of every edge in the original brain connectivity graph.

of the connectivity graph (the same partition into ROIs is used); the only difference is that now the diffusion map is randomized by reshuffling arbitrarily the ODFs. Finally, we compute the confidence level of the connections using the graphs derived from both the original and reshuffled data sets. We describe each of these steps below.

A. Diffusion MRI acquisition

The images from a diffusion MRI experiment of a human brain were acquired on four healthy volunteers with an Achieva 3T Philips scanner. We used a diffusion weighted single shot spin echo EPI sequence with the following timing parameters: $\text{TR/TE}/\Delta/\delta = 4200/89/43.5/32.5$ ms, where Δ is the diffusion time interval and δ the diffusion gradient duration [35]. With maximal diffusion gradient intensities of 80mT/m this yielded a maximal b-value of 9000 s/mm^2. Q-space was sampled over a hemisphere using 129 different encoding gradients, and the data were reconstructed following a classical DSI scheme [226] (see Section 2.6), producing a 3D diffusion probability density function (pdf) in every voxel. The acquisition block was made of 36 slices of a 112 x 112 matrix, with a spatial resolution of 2 x 2 x 3 mm^3. The acquisition time was approximately 18 minutes. Next, we simplified the data by computing for each voxel the ODF. Moreover, a high-resolution T1-weighted (MP-RAGE) MRI was performed on the same volunteers. This acquisition was then registered on the diffusion images using the affine registration method based on maximization of mutual information of Maes et al. [139, 145].

B. White Matter tractography

DSI tractography is performed in WM using the algorithm presented in Section 4.3 [89, 95]. Briefly, the ODF of each voxel is reduced into a set of normalized direction vectors corresponding to the local maxima of the ODF. Then, we choose a set of initialization points uniformly distributed in each brain WM voxel. From each of these points a fiber starts growing with a fixed step size in two opposite directions, locally following the direction of the diffusion maximum which is the closest to the fiber trajectory. The growing process ends when the end-points of the fiber have reached the WM-GM interface, or when a sharp change of direction occurs (more than 0.25 radian/mm). Fibers that do not reach the WM-GM interface are eliminated. In this work, approximately 1 million fibers are generated in the brain WM.

C. WM-GM interface partition into ROIs

The procedure used here is the same as the one described in Section 4.2. Let us briefly remind the basic principles of this methodology. It is based on an atlas-based cortical registration method using the curvature information, i.e. sulcus and gyrus [36, 54, 61]. It provides an automatic labelling of the cortex into 66 gyral-based parcels, as well as a recursive subdivision of these parcels into small ROIs. Using this procedure, we divide the cortex into 998 ROIs, compact and of similar size, and with a surface of about 150mm^2. In this study, we only use the highest resolution, and therefore the connection matrices at the other scales are not computed.

D. Construction of the original brain connectivity graph G_O

In what follows, we will use the term *fiber* when referring to a single tractography fiber connecting two ROIs. The abstract link between two nodes in a graph will be denoted by the term *edge*. We create the original brain connectivity graph G_O by combining the output of the two previous steps (B and C) [89, 94]. Every ROI becomes a node of the graph. We build an edge e between every pair of nodes. Its weight represents the fiber density in terms of number of fibers per unit surface, as defined by Equation 4.1. If no fiber exists between two ROIs, a zero weight is assigned to the corresponding edge.

In order to analyze the properties of the brain connectivity graphs, the distance between the nodes might reveal useful. We therefore introduce the edge distance l_e, defined as the geodesic distance in the brain WM (i.e., the shortest path being confined in the WM mask) separating the two ROIs corresponding to the end-nodes of the edge in the graph.

E. Construction of the randomized brain connectivity graphs G_{R_i}

Remember that we want to compare the original tractography solution with others where diffusion coherence contrast has been lost. This is achieved as follows. Starting from the original acquisition data set, we find and randomly reshuffle the voxels corresponding to the brain WM, i.e., we randomly permute the ODFs of these voxels. In other terms, this is a re-sampling of the data, or more particularly of the WM voxels, without replacement. Note that the reshuffling we perform is fundamentally different from the bootstrapping method used for example in [118]. Indeed, bootstrapping techniques are generally used in

order to assess the accuracy of an estimator. In this work, we perform a re-sampling only in order to loose the diffusion coherence contrast in the data. It results in a data set whose geometrical properties, such as the WM tractography mask and the WM-GM interface, are identical to the original one. Similarly, the number and orientation of the main diffusion directions are preserved, but, what is crucial, the information about diffusion coherence is lost. We generate 30 reshuffled data sets (this choice will be discussed in the following). Next, we perform tractography to generate a solution on every reshuffled data set. Finally, as in D, we construct the connectivity graphs G_{R_i} based on the tractography results on the i-th randomized data set and the same partition into ROIs as obtained for the original data set (C).

F. Confidence level computation

Let $w_{e,O}$ and w_{e,R_i} denote the weight of the edge e in G_O and G_{R_i}, respectively. Considering the set of I randomized brain connectivity graphs $G_R = \{G_{R_1}, ..., G_{R_I}\}$, for every edge e we have a set of edge weights $W_{e,R} = \{w_{e,R_1}, ..., w_{e,R_I}\}$ coming from a specific distribution. This set of edge weights $W_{e,R}$ provides us with an empirical distribution, which is an estimate of the true underlying distribution.

Let $Y = \{y_1, y_2, ..., y_N\}$ be some real data and let p be a proportion between 0 and 1. A quantile is a value such that a proportion p of the observations Y is smaller than $\hat{q}(p)$. In our case, we have $Y = W_{e,R}$, and the edge weight in G_O corresponds to a quantile of $W_{e,R}$, with $w_{e,O} = \hat{q}_e(p_e)$. We define the confidence level c_e as the proportion p_e of $W_{e,R}$ being smaller than $w_{e,O}$. The confidence level is computed for every edge whose weight in G_O is strictly positive (called a non-zero edge in the following). It is important to note that the confidence level is computed for each edge, independently from the other edges in the graph.

6.3 Results

Before we analyze the confidence level described previously, it may be interesting to briefly analyze some of the properties of the brain connectivity graphs G_O and G_R. We focus on two basic node characteristics: the degree d_n, i.e. the number of edges incident on the node n, and the strength s_n, which is the weighted sum of edges incident on the node n [12]. We also look at two edge statistics: the edge distance l_e distribution and the edge weight w_e distribution. After a short comparison between the original brain connectivity graphs G_O and the set of randomized equivalents G_R, we analyze, with the help of the constructed confidence level, the contribution of the diffusion coherence contrast to every connection. In the third part, we show as an illustration how to integrate the confidence level into the connectivity matrix. Finally in the last part, we introduce a way to optimize the computation.

Comparison of G_O with G_R

In what follows, the plots compare the original graph G_O with a single randomized brain connectivity graph G_{R_i}. Since the variations observed among the set of randomized graphs G_R are not significant (data not shown), these plots are valid for the set of randomized graphs G_R. Therefore, we will speak of G_{R_i} to refer to any single randomized brain
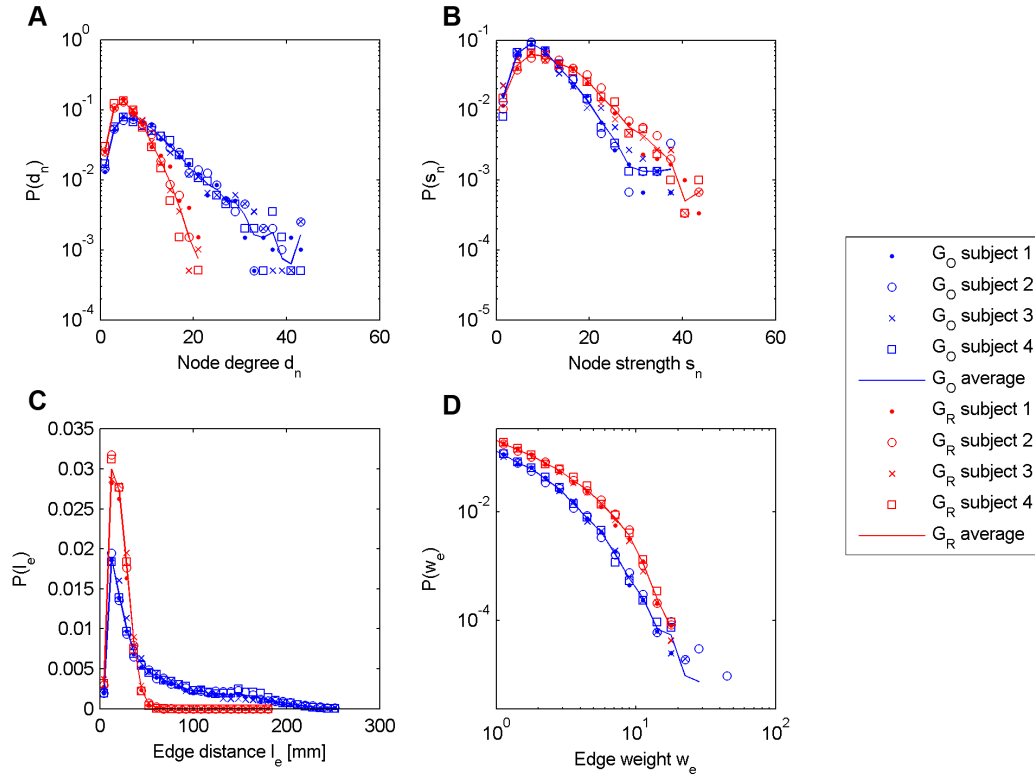
Figure 6.2: Node and edge statistics for G_O and G_R. A: Node degree distribution. B: Node strength distribution. C: Edge distance distribution. D: Edge weight distribution.

connectivity graph. It is also important to note that all these experiments were performed for one subject at three different scales of the connectivity graph: 500, 1000 and 2000 nodes. As the results were similar for the three scales, we decided to only work with the graphs with 1000 nodes.

In Figure 6.2, we report the node degree (A) and node strength (B) distributions for both G_O and G_{R_i}. We also plot the edge distance l_e distribution (C) and the edge weight w_e distribution (D) (computed on non-zero edges only). We can see that G_O presents a node degree distribution with a heavier tail than G_{R_i}, indicating that some nodes are more connected in the original brain connectivity graph. This is explained by the fact that the number of connections is higher in G_O (9926 edges in average) than in G_{R_i} (5686 edges). In Figure 6.2C, we can see that the edge distance is much shorter in G_{R_i} than in G_O, indicating a loss of long-range connectivity in G_{R_i}, which explains this difference in the number of connections. In Figure 6.2B, we can see that there are slightly more nodes with a high node strength in G_{R_i} than in G_O. This can be explained by the fact that the edge weight is higher in G_{R_i} than in G_O, as shown in Figure 6.2D. A more complete evaluation of these brain connectivity graphs is presented in Chapter 9.

Next, we focus on the evolution of the connectivity with respect to the edge distance. In Figure 6.3A, we plot the number of non-zero edges as a function of the edge distance. Figure 6.3B represents the mean edge weight as a function of the edge distance. These plots lead us to the following observations.
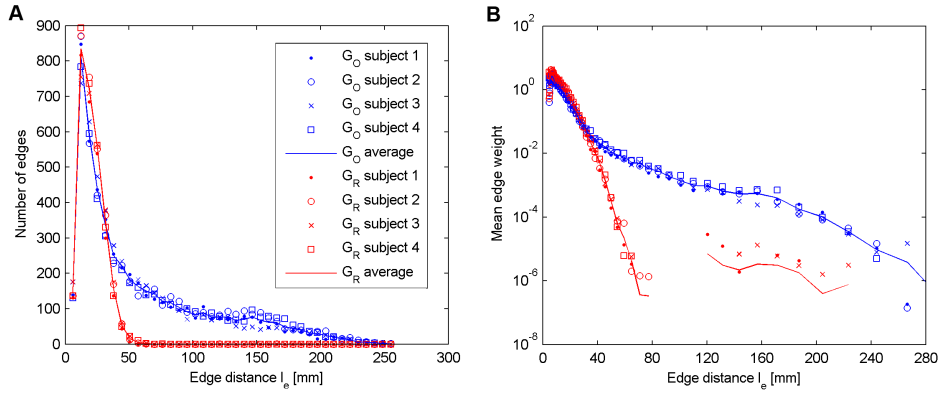
Figure 6.3: (A) Distribution of non-zero edges in G_O and G_R as a function of the edge distance l_e. (B) Mean edge weight in G_O and G_R as a function of the edge distance l_e.

Short connections The tractography algorithm produces quite accurately the same number of short non-zero edges (typically below 40mm) in both G_O and G_{R_i} (Figure 6.3A), and the mean edge weight for edges of short edge distance is almost identical (Figure 6.3B). Since a fiber between two given ROIs is found by the tractography algorithm only if a path of coherently aligned directions of maximal diffusion exists, we deduce that for two closely located ROIs the chance of finding such a path of coherent diffusion in the reshuffled data set is non negligible. It is also important to note that for short connections the standard deviation of the edge weight is almost identical in both G_O and G_{R_i}, and the edge weight distribution for a given edge distance is similar in both cases (data not shown). Furthermore, in Figure 6.3B, in the short range, there seems to be a clear dependence between mean edge weight and edge distance.

Mid- and long-range connections Unlike for short connections, it seems that for mid- and long-range connections some fundamental differences appear between the original and the reshuffled data sets. We remember that the tractography is run in exactly the same way and with the same parameters in all cases (particularly with the same number of fiber initializations). However, we see that the original brain connectivity graph G_O contains more non-zero edges than G_{R_i}, and that these additional edges are mid- and long-range. Similarly as in the short range, the mean edge weight in G_{R_i} continues to decrease with increasing distance, following an exponential law. This is because when the edge distance l_e increases, the chance of finding a path of coherent diffusion sharply decreases. On the other hand, the mean edge weight in G_O changes its behavior at around an edge distance of 40mm by decreasing very slowly with increasing edge distance. The fiber density (i.e. edge weight) of an edge in G_O seems thus not to be dependent from its distance. Interestingly, it turns out that the limit of 40mm is consistent across the subjects and is not dependent on the scale of the connectivity graphs, since similar results were found for graphs with 500, 1000 and 2000 nodes (data not shown), but might change with other parameters as we discuss below.
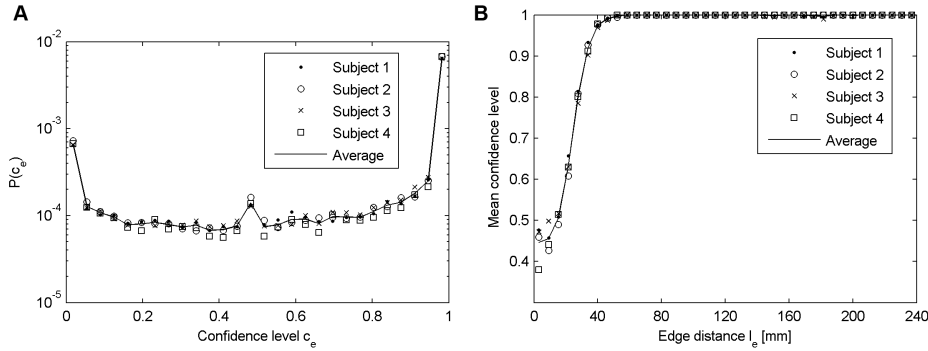
Figure 6.4: (A) Distribution of the confidence level computed for non-zero edges. (B) Mean confidence level as a function of the edge distance l_e.

Confidence level analysis

In this part, we focus on the analysis of the confidence level. First, we show in Figure 6.4A the distribution of the confidence levels. According to the definition of the confidence level, a zero value $c_e = 0$ means that the edge has a lower weight than all the realizations of the same edge in G_R. On the other hand, $c_e = 1$ corresponds to edges whose weight is higher than all the realizations of the same edge in G_R. In the middle range, $c_e = 0.5$ indicates that the edge weight obtained in G_O is comparable to the median of the measures obtained in G_R. We can see in Figure 6.4A that most of the distribution is close to the maximum value, meaning that the tractography globally produces tracts that are the result of the measured diffusion coherence contrast. However, the peak near the minimum value indicates that some of the edges produced by the tractography have a stronger weight in G_R than in G_O, and are thus probably due to non-diffusion effects.

Next, we investigate the evolution of the confidence level with respect to the edge distance. In Figure 6.4B, we plot the mean confidence level as a function of the edge distance. We can see that the confidence level rapidly increases with the edge distance. From a distance of around 60mm the mean confidence level reaches the maximum value and stays constant. We can then say that short edges globally present a low confidence level. In contrast, we can have a strong confidence in mid- and long-range connections.

Example of application

A representative example of a high-resolution structural connection matrix of an individual human brain is shown in Figure 6.5. The matrix is organized as follows: the upper left block represents the connections in the right hemisphere and the lower right block shows the connections in the left hemisphere. The off-diagonal blocks map the inter-hemispheric connections. The color bars at the left and bottom of the matrix help to make the correspondence between the matrix entries and the cortical parcels as displayed on the left part of the figure. Since the connections are not oriented the matrix is symmetric. Therefore, we can show simultaneously two parameters for every connection in the matrix. The upper triangular part of the matrix represents fiber densities between pairs of single ROIs. The lower triangular part shows the confidence levels associated to the connections. The confidence level which is added in this matrix is a valuable help
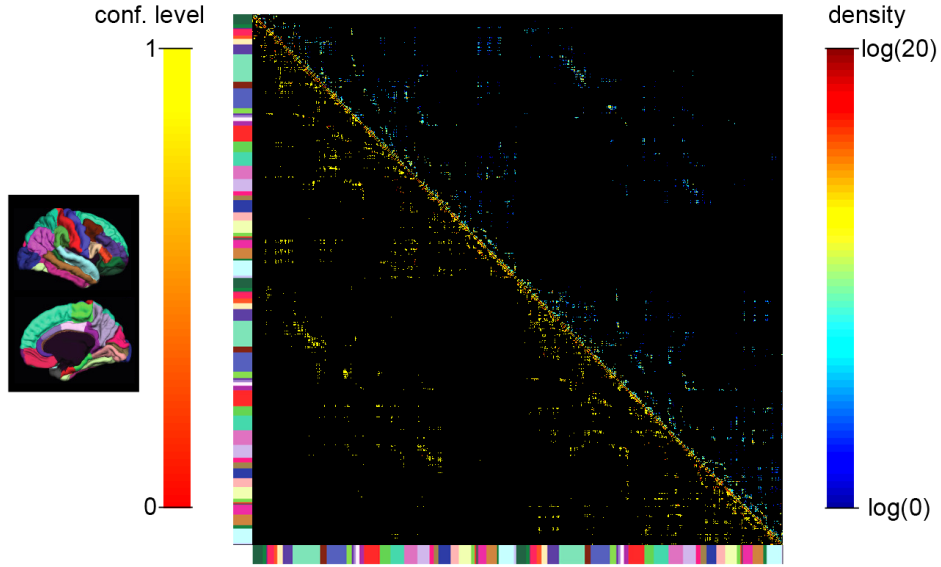
Figure 6.5: High-resolution structural connection matrix, representing the fiber density (upper triangular part) and the confidence level (lower triangular part). The matrix is organized as follows: the upper left block represents the connections in the right hemisphere and the lower right block shows the connections in the left hemisphere. The off-diagonal blocks map the inter-hemispheric connections. The color bars at the left and bottom of the matrix help to make the correspondence between the matrix entries and the cortical parcels as displayed on the left part of the figure.

towards the interpretation and the assessment of the whole-brain connectivity. We can see that the connections which present a low confidence level are mainly located very close to the diagonal, which corresponds to intra-parcel connections. This is not surprising since those connections are mainly composed of short fibers. On the contrary, longer connections such as the inter-hemispheric connections (off-diagonal blocks of the matrix) present a very high confidence level.

Optimization of the computation

For a given edge e, the more samples we have in $W_{e,R}$, the better the estimation of the true underlying distribution, and thus the more accurate the confidence level. Therefore, one would be tempted to create a lot of randomized brain connectivity graphs, but unfortunately their generation is computationally very expensive. In this context, there is a need for optimization of the computation.

In Figure 6.3B we see that the mean edge weight in G_{R_i} depends on the edge distance l_e. Let us suppose for a while that the other factors, such as the brain geometry or the tractography algorithm, do not significantly influence the mean edge weight in G_{R_i}, or at least affect the edges uniformly regardless of the edge distance l_e. In this case, the sets of edge weights $W_{e_1,R}$ and $W_{e_2,R}$ produced by two different edges, e_1 and e_2 with the same edge distance l_e, are sampled from the same underlying distribution. Therefore,
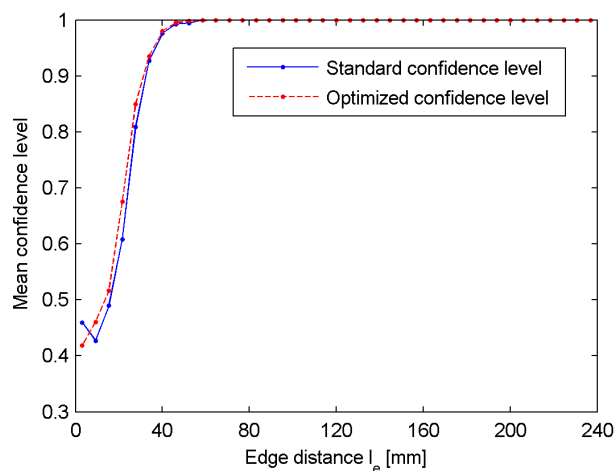
Figure 6.6: Mean standard and optimized confidence levels as a function of the edge distance l_e.
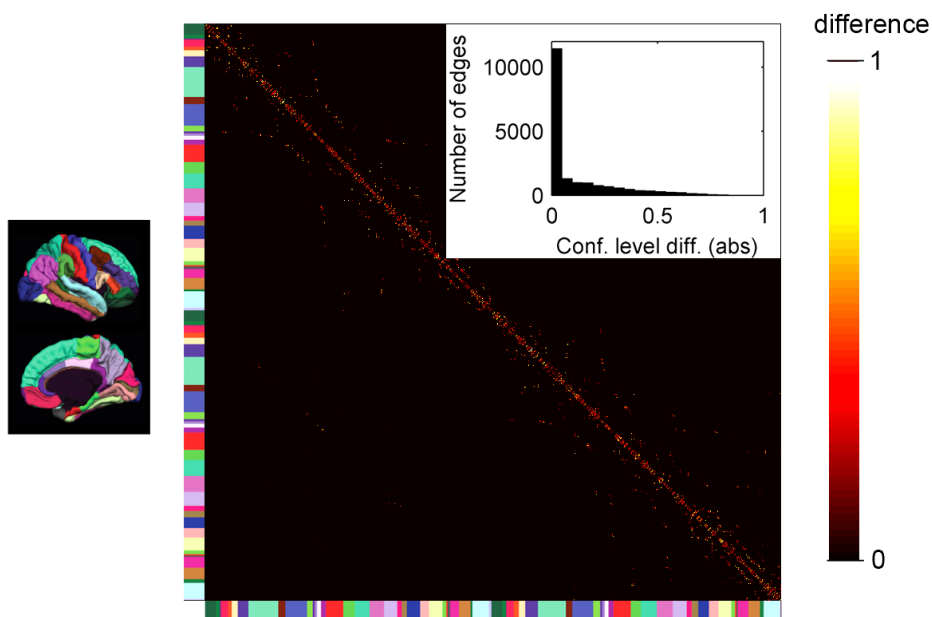
Figure 6.7: High-resolution matrix, representing the differences between the standard and optimized confidence level (absolute values). Insert: distribution of the differences between standard and optimized confidence level (absolute values).

by grouping the edges according to their edge distance l_e, we can increase the size of the sets $W_{e,R}$. From a practical point of view, this means that instead of generating 30 reshuffled data sets which is very time-consuming, producing for each edge e a set $W_{e,R}$ of size 30, we create only one reshuffled data set. Next, we group the edge weights having a similar edge distance l_e and create sets of edge weights dependent on the edge distance only. Denote by $W_{d,R}$ the set of all edges whose edge distance l_e is close to d, that is $W_{d,R} = \{e|l_e \in [d - \epsilon; d + \epsilon]\}$, with ϵ a tolerance value. The confidence level is then computed as described above, by replacing $W_{e,R}$ with $W_{d,R}$.

We compare the confidence level computed on the set of 30 reshuffled data sets G_R, called standard confidence level, with the proposed method, denoted by optimized confidence level. In Figure 6.6 we report the mean confidence level as a function of the edge distance, for both methods and for a single subject (the results obtained with the other subjects are similar, data not shown). It turns out that the mean confidence level is very similar for both the standard and the optimized methods. This observation is confirmed by a correlation of 0.79 (averaged over the four subjects) between the standard and optimized confidence levels. In Figure 6.7, we report the matrix containing the absolute value of the differences between the two confidence levels. We can see that the difference is only rarely higher than 0.2, which is confirmed by a distribution very close to zero, as shown in the insert of Figure 6.7.

6.4 Discussion

The rational behind the method

How can we be sure that a given computed connection is due to diffusion coherence contrast (i.e., underlying neuronal architecture) and not to noise, limited resolution (aliasing), brain geometry or to the properties of the tractography algorithm itself? In other words, how can we know that a given image feature (i.e., a connection) comes from a specific physical process (diffusion) and not from other uncontrolled imaging parameters? Given that we have an adequate image model, the straightforward method is to study the behavior of the imaging feature in an identical data set from which the specific physical process has been removed (i.e. in which the diffusion coherence contrast is removed). In practice, we can obtain such a data set by randomly reshuffling the voxels in the WM mask with their associated ODFs. Then, we can perform the tractography and compute the associated connectivity graph. By creating a large number of reshuffled data sets, we can finally compute the confidence level of a given edge in G_O with respect to the estimate of the weight distribution of the same edge obtained in G_R. This method provides us with a measure of how unlikely it is that the measured edge weight comes from something else than diffusion coherence contrast.

However, we have to keep in mind that tractography is a method that maps lines of diffusion coherence inside the white matter. The relation between real or anatomical fibers and pseudo-fibers produced by the tractography is conceptual and experimental to some extent [142, 182]. Consequently, the confidence level does not give information about the existence of fibers. Instead, as mentioned in [118], it refers to the *amount of confidence we can place in the tract realization not being a spurious one off occurrence that has been unusually corrupted by noise, motion, or other sporadic artifacts.* We also insist on the fact that the confidence level does not improve the tractography quality.

It just gives additional information about the tractography solution in order to help its interpretation.

One of the issues of this work is related to the number of reshuffled data sets. Indeed, the more reshuffled data sets we produce, the more accurate the empirical quantiles, and thus the more accurate the confidence level. This raises the following question: Are the 30 reshuffled data sets used in this work sufficient to have an accurate estimate of the confidence level? Since the reshuffled data sets are generated independently, the samples constituting the set of edge weights $W_{e,R}$ are also independent. This means that the empirical distribution provided by $W_{e,R}$ is an unbiased estimate of the true underlying distribution. The confidence levels are thus not biased by the number of reshuffled data sets. Consequently, increasing the number of data sets would of course improve the accuracy of the confidence level, but would not significantly modify the results we obtained. Finally, we should insist on the fact that generating a reshuffled data set is very time-consuming. Thus, generating more than 30 data sets is practically not reasonable.

The effect of the spatial resolution

When we consider the relation between the mean edge weight and the edge distance in the original data set (Figure 6.3B), we notice that it is bimodal. In the range of short distances (below 40mm), the plot follows a similar behavior as the reshuffled data set, while for longer distances the mean edge weight decreases very slowly. The relative constancy of the mean edge weight with respect to the edge distance is a very important observation. It tells us that our way of measuring connectivity is not biased by distance. The initial bump for edges shorter than 40 mm may be explained in two ways. First, we know that the brain performs most communication locally (functionally associated cortical areas are nearby) [106,127], yielding possibly stronger connectivity in a short range. Second, which is in our opinion the most likely explanation, is that for short-range edges there is no big difference between principal diffusion orientations that are coherently versus randomly oriented given the small number of tracking steps. This difference is a consequence of a low spatial resolution. Indeed, the shorter the distance between two distinct ROIs, the lower the number of voxels separating these ROIs, and thus the higher the probability of finding a path of coherent diffusion linking these ROIs by chance. Therefore, the only way to keep track of the short-range connections would be to increase the spatial resolution of the diffusion MRI acquisition, which would in turn decrease the chance of connection at random. This also means that we potentially overestimate the number of short connections due to the additional effect of true and "by chance" diffusion coherence over short distances.

Considering Figure 6.3B, one may be tempted to consider the ratio between the mean edge weight in the original and the reshuffled data sets as a measure of the signal to noise ratio (SNR). Presented that way, we directly notice that the SNR is too low for fibers below 40mm to make any statement. In particular, a low confidence level in these connections does not mean that they do not exist, but only that they cannot be faithfully distinguished from connections created by the unpredictable effects.

Optimized versus standard confidence level

The optimized confidence level is based on the assumption that the mean edge weight in G_R depends mainly on the edge distance l_e. The other factors, such as the brain geometry or the tractography algorithm parameters, are supposed to have only a minor influence on the edge weight, or at least to affect the edges uniformly regardless of l_e. Of course, this assumption is very restrictive, and practically not really verifiable. However, the similar results produced by both the standard and the optimized method seem to confirm the hypothesis. We do not pretend that the brain geometry does not play a role on the edge weight, but we believe that its effect is limited. Thus, we think that the optimized confidence level is an adequate method to dramatically reduce the computation time, although more investigations have to be performed to confirm our results.

As stated before, the probability of finding a path of coherent diffusion is rather low in a reshuffled data set, and therefore a large proportion of edges in G_R have a zero weight. Due to the limited number of reshuffled data sets, the confidence level of long-range connections tends to be slightly over-estimated. Apart from the computation time, another advantage of the optimized confidence level is that the grouping of edges increases the number of samples per estimated distribution. Consequently, the optimized confidence level partially solves the issues raised by the limited number of reshuffled data sets.

Advantages, drawbacks and future work

In this study we present a method to associate a confidence level with a connection measured with tractography. This confidence level allows us to quantify the contribution of the diffusion coherence contrast to the produced tracts. We observe that tractography maps well the diffusion coherence contrast over long distances but that for short-range trajectories it is impossible to say whether their source is the diffusion coherence or chance. The direct consequence is important for all studies that aim at mapping and characterizing short-range connections; their results should be interpreted with enormous care.

However, it is worthwhile to point out that very important contributors to aberrant connectivity mapping are not filtered out with the presented methodology. Indeed, even if the diffusion MRI experiment is performed properly, i.e. ideally without susceptibility artifacts or other systematic biases, there are in our opinion, two sources of errors: noise and aliasing or insufficient resolution. The effect of noise is rather straightforward: it produces unwanted principal directions of diffusion, yielding aberrant and missing connections [118,138]. The question of aliasing is more difficult to analyze and would justify an article on its own. Schematically, insufficient angular and spatial resolutions yield 1) biased principal directions of diffusion (e.g. smoothing of two diffusion peaks into one) 2) partial volume effects [5] which can be the cause of constructing aberrant fiber tracts. Indeed, when the spatial resolution is insufficient relatively to the maximal curvature radius of fiber bundles, tracts that cross in reality may kiss in the tractography reconstruction and vice versa, thus creating aberrant solutions.

The confidence level computed in this work is based on the edge weight only. However, it is highly likely that other features could help in the evaluation of short-range connections. A possible way to improve the quality of the confidence level would be to include a measure of the dispersion of the trajectories, as follows. Let us consider an edge connecting two close ROIs. In the reshuffled data sets the fibers constituting this specific edge should present various trajectories, which can be captured by a high variability of

the fiber length. In contrast, in the original data set, if a path of maximal diffusion exists between the two ROIs, most of the fibers constituting the corresponding edge should roughly have the same trajectory, and therefore have the same length. Consequently, the variance of the fiber length could help in the evaluation of the confidence level of short-range connections.

Conclusion

In this work, we have proposed a method to evaluate the confidence level of every connection obtained by tractography, in order to discriminate the fibers resulting from the diffusion signal itself from those due to some non-diffusion effects. According to the presented results we can say that the tractography, as it is performed in this work, is well suited to map mid- and long-range connections with a high confidence level. On the contrary, the low confidence level found for the short-range connections indicates that some precautions must be taken when mapping the brain short-range connectivity. In our opinion spatial resolution is one of the main factors that affect the accuracy of short-range connections in tractography.

As mentioned previously, the confidence level does not confirm or infirm the existence of the produced fiber tracts. For this particular purpose, Several approaches can be considered. Synthetic data can be used to validate the tractography algorithm [142]. Tractography results can also be compared to tracing studies [142, 182]. Unfortunately, those methods are limited to either phantoms or *ex-vivo* material. Another validation approach consists in comparing the results of tractography to another imaging modality. For example, it has been shown that functional networks can be mapped with resting-state functional MRI [172, 222]. Those functional networks must to some extent be related to the underlying structural connectivity. The study of the relationship between structure and function may not only help us to understand the architecture of the brain, but also may prove the relevance of tractography measurements. This is the topic of the next chapter.

Predicting Resting-State Functional Connectivity from Structural Connectivity

7

7.1 Introduction

As mentioned in the previous chapters, the validation of diffusion MR tractography is difficult because of the lack of a gold standard. Current validation studies are limited to *ex vivo* material [182] or synthetic data [142]. In Chapter 4, we have presented a methodology to map the human connectome, a representation of the whole-brain structural connectivity. On the other hand, functional MRI has enabled the mapping of functional networks [172, 222]. In the present chapter, we combine structural connectivity obtained from diffusion MR tractography and functional connectivity obtained from functional MRI, in order to study the relationship between brain structure and function.

Populations of neurons in the mammalian cerebral cortex are continuously active during purposeful behavior, as well as during resting and sleep [87]. Activity levels are modulated across time by the internal dynamics of each neuronal population and by signals received from cortical, subcortical, and peripheral elements of the nervous system. In the past decade, there has been intense interest in the patterns of correlated activity ("functional connectivity" [71]) in the human brain, because these patterns are believed to reflect the patterns of interaction between neuronal populations. A set of functionally connected regions is referred to as a "functional network." Some functional networks are most commonly detected when participants are not performing any demanding task (in the resting state); others are observed in the context of task-focused behavior; and some networks persist across both behavioral states [13, 83, 97, 221]. A set of regions including posterior medial, anterior medial, and lateral parietal cortices comprise the

default mode network (DMN) [82, 172], a functional network that is particularly robust
across participants and cognitive states. It has been suggested that the more persistent
functional networks may be involved with ongoing organizational processes in the brain
[66, 88], and that disruptions in reliably present correlations are indicative, and potentially
diagnostic, of neuropathology [81, 98].

Because the propensity for two areas to interact should vary in proportion to the
density and efficacy of the projections connecting them, it is widely assumed that the
repertoire of functional configurations assumed by the cerebral cortex is reflective of
underlying anatomical linkage [48, 53, 146, 164, 176, 222]. However, the nature of this
structure-function relationship is only beginning to be revealed. A general correspon-
dence between functional connectivity (measured using functional MRI) and structural
connectivity (measured using diffusion tractography) has previously been demonstrated in
adjacent gyri in a single axial slice [130]. However, several questions remain. First, given
that structural and functional connectivity are correlated, is it possible to infer structural
connectivity from functional connectivity? Second, how does the structure-function re-
lationship vary as we increase the distance between neuronal populations, and what are
the contributions of indirect structural connections to functional connectivity? Third,
to what extent does functional connectivity vary across time, and which anatomical fea-
tures distinguish persistent functional networks from those that are more transient? To
address these questions, we compare structural and functional connectivity maps to one
another. We then use the structural connectivity maps as couplings in a computational
model of the large-scale dynamics of the cerebral cortex [27, 108], and from these dynamics
we extract simulated blood-oxygenation level dependent (BOLD) signals and functional
connectivity, which can be quantitatively compared against empirical observations.

7.2 Material and methods

The proposed procedure consists of two main steps. First, we measure non-invasively
the structural connectivity (SC), i.e. the human connectome, in 5 individual participants
using diffusion spectrum imaging (DSI) and tractography. The methodology is similar to
the one described in Chapter 4, and is summarized in what follows. Next, we record resting
neural activity in the same participants using functional MRI. Resting-state functional
connectivity (rsFC) maps are based on the Pearson correlations between the BOLD time
series in all possible pairs of the 998 cortical regions.

Extraction and Topology of Structural Networks

DSI Acquisition The study protocol was reviewed and approved by the Institutional
Review Board at the University of Lausanne. After obtaining written informed consent
in accordance with institutional guidelines, 5 healthy right-handed male participants (age
29.4 ± 3.4 years) were scanned on an Achieva 3T Philips scanner. A high-resolution
T1-weighted gradient echo sequence was acquired in a matrix of 512 x 512 x 128 voxels of
isotropic 1mm resolution. Diffusion spectrum was performed using a diffusion-weighted
single-shot echo planar imaging sequence (TR = 4200 ms, TE = 89 ms) encoding 129
diffusion directions over a hemisphere. The maximum diffusion gradient intensity was
80 mT/m, the gradient duration δ was 32.5 ms, and the diffusion time Δ was 43.5 ms,
yielding a maximal b-value of 9000 s/mm^2. The acquisition matrix was 112 x 112, with

an in-plane resolution of 2 x 2 mm. Thirty-six contiguous slices of 3-mm thickness were acquired in 2 blocks, resulting in an acquisition time of 18 min. The reconstruction of the data is performed as follows [226] (see also Section 2.6). Following diffusion spectrum and T1-weighted MRI acquisitions, the segmented gray matter is partitioned into 66 anatomical regions according to anatomical landmarks using Freesurfer and 998 ROIs. White matter tractography is performed with a classical streamline algorithm and finally, fiber connectivity is aggregated across all voxels within each of the 998 predefined ROIs. For more details please refer to Chapter 4.

Resampling The fiber densities measured by streamline tractography are exponentially distributed and span several orders of magnitude (see Chapter 9). Since interregional physiological efficacies would not span such a large range, we resample the fiber densities into a Gaussian distribution as follows: given N raw data values $x_1, x_2, ..., x_N$, we generate N random samples $r_1, r_2, ..., r_N$ from a unit Gaussian distribution. We then replace the smallest raw data value with the smallest randomly sampled value, the second-smallest raw data value with the second-smallest randomly sampled value, and so on until all raw data values are replaced. This produces a set of N resampled data values distributed according to a standard Gaussian, which we then rescale to a mean of 0.5 and a standard deviation of 0.1 dimensionless units. Note that the empirical results we report in this study remain strongly significant when SC is not resampled (data not shown). In what follows, the term fiber strengths will be used to refer to the resampled fiber densities.

Fiber Distance and Euclidean Distance The fiber distance between two ROIs is calculated as the average length of all of the connecting fibers found using streamline tractography. The Euclidean distance between two ROIs is calculated using the mean Talairach coordinates of voxels comprising an ROI. We use the fiber distance where possible, as it more closely reflects the distance along the cortical surface. However, fiber distance is only known where SC is present, and so for analyses in which we compare the effects of SC absence and presence while controlling for distance we use Euclidean distance.

Extraction and Topology of Functional Networks

BOLD Acquisition The same 5 participants were scanned in eyes-closed resting state using a Siemens TimTrio 3T system using a gradient echo EPI sequence (TR = 2000 ms, TE = 30 ms). Participants were instructed to keep their eyes closed and to remain alert. An axial plane was used with a field of view of 211 x 211 mm (64 x 64 voxels, each 3.3 x 3.3 mm in-plane). Thirty-five slices of 3 mm thickness with a 0.3 mm gap were acquired. All participants were scanned twice on separate days (scan 1: 20 min, scan 2: 15 min).

Signal Preprocessing and Correlations Raw BOLD signals are registered and resampled onto the b0 image of the diffusion scan using rigid-body registration (SPM5, www.fil.ion.ucl.ac.uk/spm). Following slice-time correction BOLD time series are then computed for each of the 998 ROIs by averaging across all voxels within the ROI mask. ROI BOLD time series are then piecewise-linearly detrended (every 50 s) and mean cortical, ventricular, and white matter signals are regressed from each time series. The results we report are essentially unchanged if we regress out only the white matter and ventricu-

lar signals, and not the global mean. Finally, Pearson correlations are calculated between all ROI-pairs.

High- and Low-Resolution Matrices

The 66 anatomical regions are defined according to an automated landmark-based registration algorithm [54]. The 998 ROIs are chosen to provide a roughly uniform tiling of the cerebral cortex (each ROI = 1.5 cm2) so that their borders aligned with those of the 66 anatomical regions (see Chapter 4 for details). BOLD and DSI-fiber counts are captured at voxel resolution and then voxel-averaged to provide ROI-average values. BOLD correlations are calculated using the ROI time series and then down-sampled to the 66-region map by averaging across all ROIs with a region. When averaging SC, structural connections are deemed absent overall if they are absent in more than 3 participants (high resolution) or more than 1 participant (low resolution). The SC map for Participant A is an average of 2 separate DSI scans.

Computational model

Neuronal population dynamics are simulated at a resolution of 0.2 ms for 16 min using a system of 998 neural masses with coupling strengths linearly proportional to the resampled fiber strengths at each edge. Each neural mass represents a population of densely interconnected excitatory and inhibitory neurons, in which the effects of both ligand- and voltage-gated membrane channels are accounted for. This model has previously been described in detail [27] and used in an anatomically informed model of large-scale functional connectivity in the macaque monkey [108].

7.3   Results

Overall structure-function relationship

Low resolution (66 Regions)   After averaging low-resolution data across participants, the SC and rsFC strengths across all region-pairs are found to be highly significantly correlated (r = 0.66). When excluding ROI-pairs with absent or inconsistent structural connections (see Material and Methods), this correlation strengthens to r = 0.82. Note that all correlations reported in this work are $P \ll 1e^{-3}$.

High resolution (998 ROIs)   Because of interparticipant variability in cortical morphology, averaging data at the high resolution does not produce as much of a de-noising effect as at the low resolution. For data averaged across participants (Figure 7.1), the SC-rsFC correlation is r = 0.36 and increases to r = 0.53 when excluding absent or inconsistent structural connections. For individual participants, the SC-rsFC correlations range from r = 0.39 to 0.48 (Figure 7.2A).

Computational model (998 Nodes)   A comparison of empirical SC (from participant B) and simulated rsFC derived from a single run of the computational model is shown in Figure 7.2B. For individual participants, the SC-rsFC correlations (single simulation) range from r = 0.32 to 0.44 when excluding absent connections. For data averaged across participants, the overall correlation between SC and simulated rsFC is r = 0.46 and
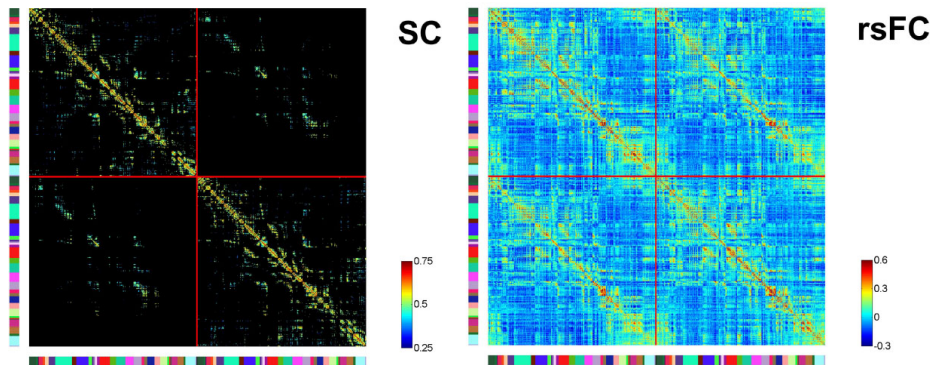
Figure 7.1: Matrices of SC and empirical rsFC at the high resolution. Both plots represent averages across all 5 participants, including 2 structural scans for participant A, and 2 repeat functional scans for all 5 participants.
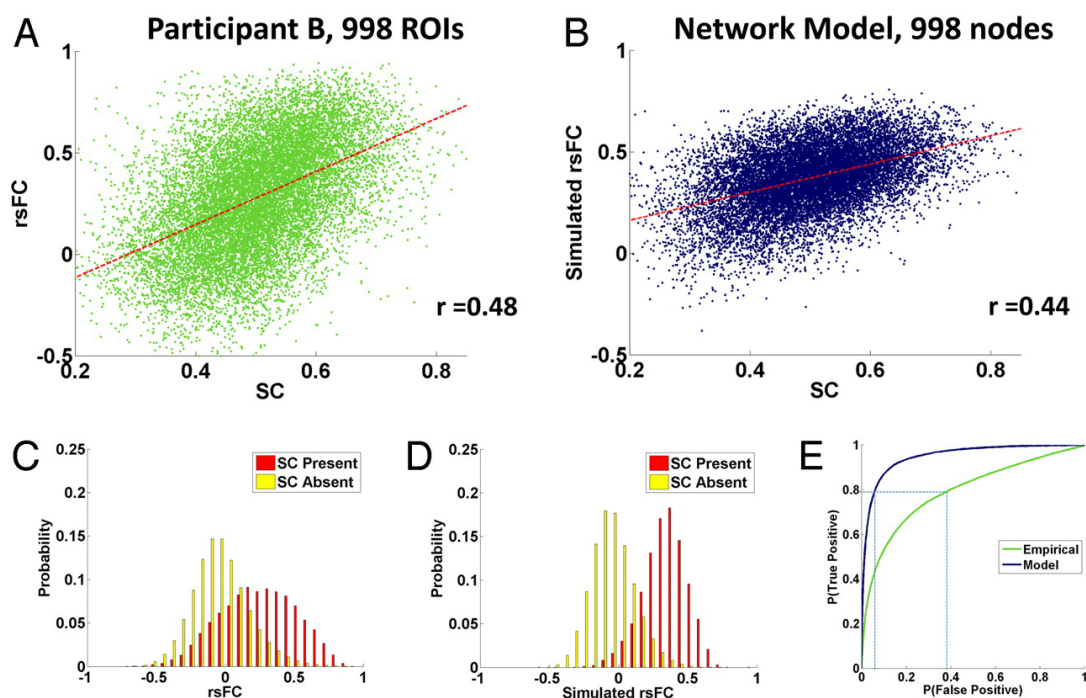
Figure 7.2: Overall SC-rsFC relationships. (A) Scatter plot (single acquisition, 20 min) of rsFC against SC at high resolution for participant B, showing edges with nonzero SC. (B) Scatter plot (single run, 16 min) of simulated rsFC against SC (from participant B) at high resolution, showing edges with nonzero SC. (C) The probability densities of rsFC values between structurally connected and unconnected region pairs, data for participant B at the high resolution. (D) Same as (C), but for simulated rsFC. (E) ROC curves, indicating the signal detection performance when inferring SC by thresholding empiricial (green) and simulated (dark blue) rsFC maps at the high resolution.

| Participant | Pearson correlation with rsFC | | | | Model R^2 SC and fiber bivariate |
	SC(All)	SC(Present)	Inverse fiber distance	Distance residuals	
66 regions					
A	0.59	0.74	0.57	0.61	0.59
B	0.56	0.70	0.54	0.59	0.54
C	0.45	0.64	0.50	0.50	0.44
D	0.59	0.71	0.46	0.61	0.50
E	0.60	0.77	0.46	0.70	0.60
Avg participant	0.66	0.82	0.67	0.67	0.69
998 ROIs					
A	0.24	0.42	0.39	0.24	0.20
B	0.24	0.48	0.47	0.23	0.27
C	0.18	0.39	0.40	0.18	0.19
D	0.23	0.42	0.40	0.23	0.20
E	0.22	0.42	0.39	0.24	0.21
Avg participant	0.36	0.53	0.47	0.30	0.30
998 Nodes					
A	0.30	0.34	0.24	0.25	0.12
B	0.39	0.44	0.28	0.35	0.19
C	0.35	0.44	0.31	0.33	0.20
D	0.33	0.37	0.28	0.26	0.15
E	0.35	0.32	0.21	0.25	0.11
Avg participant	0.46	0.52	0.41	0.37	0.28

Table 7.1: Individual participant SC-rsFC and rsFC-distance correlations (Top 2 sections), and corresponding values from individual runs of the computational model (Bottom section). Empirical rsFC is from the first fMRI scan; simulated rsFC is from a single 16 min simulation. The first 2 columns show the SC-rsFC correlations for all region pairs and for region pairs with SC, respectively. The third column shows the correlation between rsFC and the inverse of fiber distance, and the fourth column shows the correlation between SC and the residuals of the distance-regression. The fifth column provides the full model R^2 of a bivariate linear regression of rsFC on SC and inverse fiber distance. The bottom row shows the results of each calculation performed using data averaged across participants (it is not the average of the rows above). All correlations are $P \ll 1e^{-3}$.

increases to r = 0.52 when excluding absent or inconsistent structural connections. For high- and low-resolution correlations in individual participants and in the model, see Table 7.1.

Inference of structure from function   When structural connections are present, the relationship between the strength of SC and rsFC is robust in both the empirical data and computational model. When direct structural connectivity is absent, however, the rsFC

values will still vary over a wide range (Figure 7.2C and 7.2D), a finding consistent with [130]. Thus, although the presence of strong SC at an edge is predictive of strong rsFC, the reverse inference is less reliable. When inferring SC by thresholding rsFC, one obtains, for each given threshold value, some number of false-positives and some number of true-positives. The receiver-operating characteristic (ROC) curves in Figure 7.2E show how the false-positive and true-positive rates vary as this threshold is adjusted. The area under the ROC curve is greater for the modelled data than the empirical data (0.95 versus 0.79). However, in both cases, thresholding of rsFC yields highly inaccurate prediction of SC. For example, in the empirical data, the threshold at which 80% of structural connections are correctly detected is one at which more than 40% of the unconnected region pairs are incorrectly detected (see Figure 7.2E). Because structurally unconnected pairs are about 30 times as numerous as connected pairs within our high-resolution data, only 6% of inferred structural connections would be genuine at this threshold. This percentage is improved in the computational model, but still too low for practical inference. For the threshold at which 80% of structural connections are correctly detected, only 28% of the inferred SC would correspond to the true structural couplings that underlie the model dynamics.

The role of distance

On average, both structural connectivity [120, 141] and functional connectivity [177] between cortical regions decrease with the distance between those regions. This effect could result from a combination of factors, including (i) spatial autocorrelation of cortico-cortical connectivity, (ii) spatial autocorrelation of subcortico-cortical projections, (iii) activation spread along the surface of the cortex via local circuitry [58, 175], (iv) spatial blurring of the BOLD signal because of vascular drainage, and (v) MRI acquisition or data preprocessing artifacts [189]. Because most of the structural connectivity we observe is short range (as shown in Chapter 6), the structure-function relationship we report here could result artifactually if both SC and rsFC are spatially autocorrelated, but for entirely unrelated reasons. To rule out this possibility we first confirm that average rsFC is linearly related to the inverse of the fiber distance between regions (r = 0.67) (Figure 7.3A, low resolution). Then, after regressing rsFC on fiber distance, we check that structural connectivity is robustly related to the residuals of that rsFC-fiber distance relationship (r = 0.47) (Figure 7.3B). This is equivalent to calculating a partial correlation between SC and rsFC, controlling for interregional fiber distance. Although the SC-rsFC relationship is weaker when we control for distance, it remains highly significant in all participants in both high- and low-resolution analyses. A bivariate linear regression using SC and (inverse) fiber distance to predict rsFC can explain 69% of the variance in participant-averaged rsFC at the low resolution, and 30% at the high resolution (see Table 7.1 and Figure 7.3C). In the computational model, 29% of the variance in rsFC is explained by the combination of SC and inverse fiber distance at high resolution.

Indirect connections and network effects

We next seek to examine the potential role of multisynaptic anatomical structures in explaining the presence of rsFC between ROIs without direct SC. We assign indirect connections to region-pairs that are not directly connected, but for which there exists at least one 2-edge path connecting them. For each such region pair ij, the indirect structural
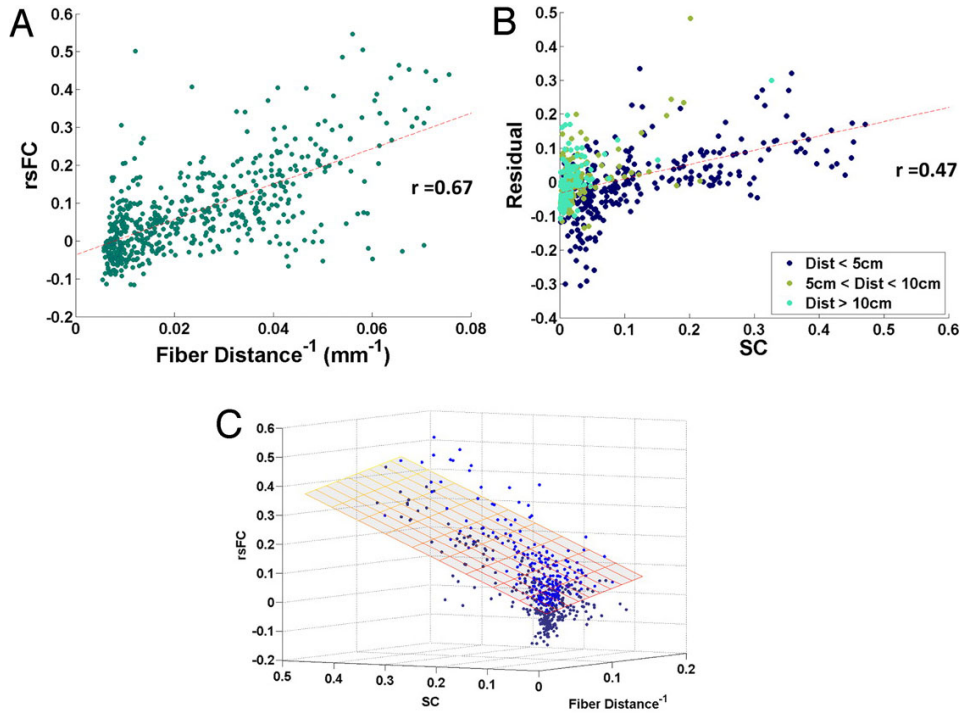
Figure 7.3: Role of distance. (A) Scatter plot of interregional rsFC against the inverse of the inter-regional fiber distance. (B) Scatter plot of residuals from (A) plotted against SC, at the low resolution. (C) Three-dimensional scatter plot, showing the relationship between SC, rsFC, and inverse fiber distance. The superimposed plane shows the fit of the bivariate linear model. Points above the plane of best-fit are light blue, points below are dark blue.

connection has strength equal to the sum of all of the multiplicatively weighted SC paths from i to j (i.e., Indirect $SC_{ij} = \sum w_{ik} w_{kj}$ where w_{ab} is the direct SC between regions a and b). When we consider only region pairs linked by a shortest path of 2 edges, the Pearson correlation between the indirect-SC values and rsFC values is found to r = 0.29 for the average data at the high resolution. This effect can not be accounted for by the Euclidean distance between region pairs, and is significant in each individual. These data suggest that indirect cortico-cortical linkage does induce some of the rsFC seen between regions lacking direct linkage.

Within the computational model, indirect connections are also observed to induce functional connectivity. When considering participant-averaged rsFC matrices, the correlation between simulated rsFC and empirical rsFC at direct links in the high-resolution network is at r = 0.46, and for indirectly connected nodes is at r = 0.37, indicating that the model is capturing network-level influences of SC on rsFC. In the low-resolution networks, the correlation between simulated and empirical rsFC increases to r = 0.70 for directly linked pairs (Figure 7.4A), but drops to r = 0.23 between indirectly linked edges.
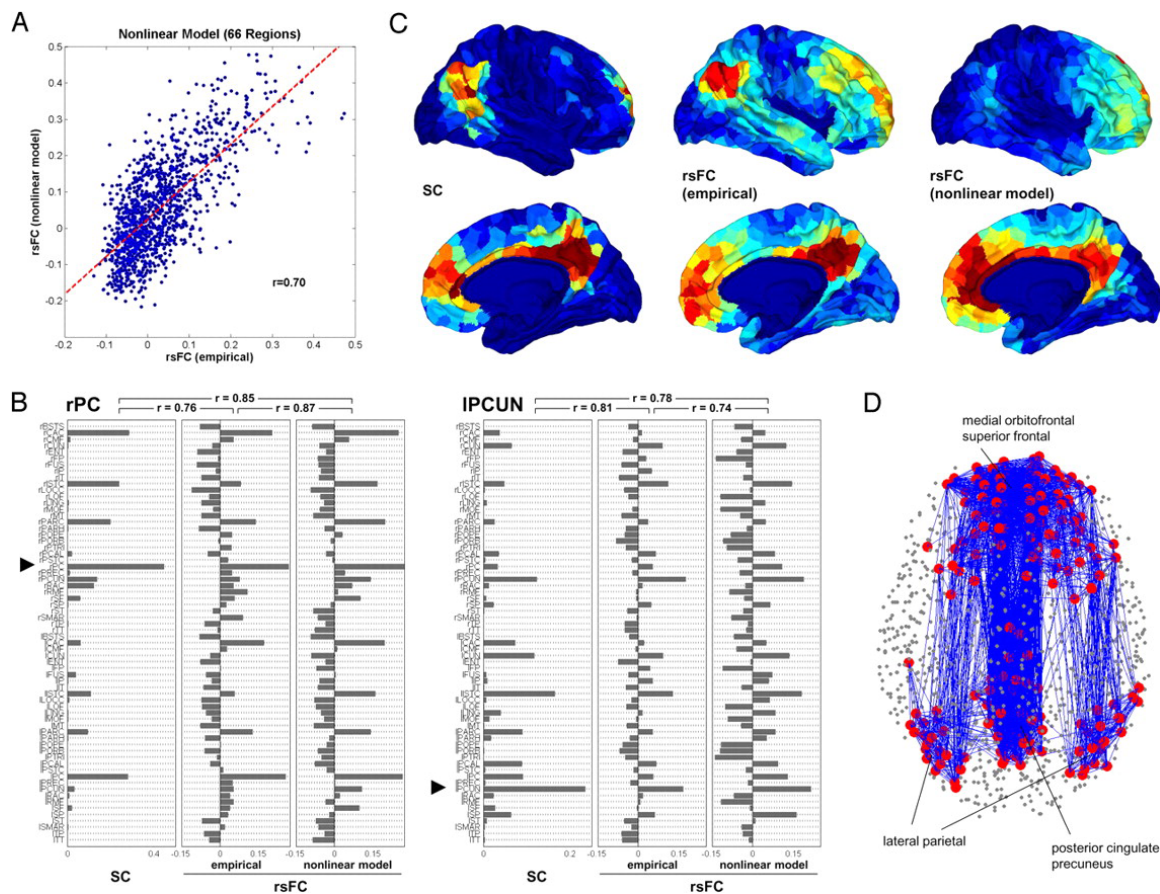
Figure 7.4: Computational model of functional connectivity. (A) Scatter plot of empirical rsFC versus simulated rsFC obtained from the nonlinear model, down-sampled to the low resolution. (B) Comparison of SC, rsFC (empirical), and rsFC (nonlinear model) for 2 single-seed regions, the posterior cingulate in the right hemisphere (rPC) and the precuneus in the left hemisphere (lPCUN). The plot displays SC and rsFC values for the seed regions in relation to all 66 regions within the corresponding low-resolution matrices. (C) Mapping of SC, rsFC (empirical), and rsFC (modeled) within the DMN. Warmer colors indicate stronger SC and rsFC. Within the posterior cingulated/precuneus, medial orbitofrontal cortex and lateral parietal cortex in both hemispheres we select a cluster of 5 ROIs at positions that most closely match the coordinates of peak foci of the DMN [67]. These 30 ROIs serve as the seeds from which SC and rsFC are determined. (D) Structural connectivity within the DMN. We select the top 200 most correlated ROIs within the DMN and plot all structural connections among them.
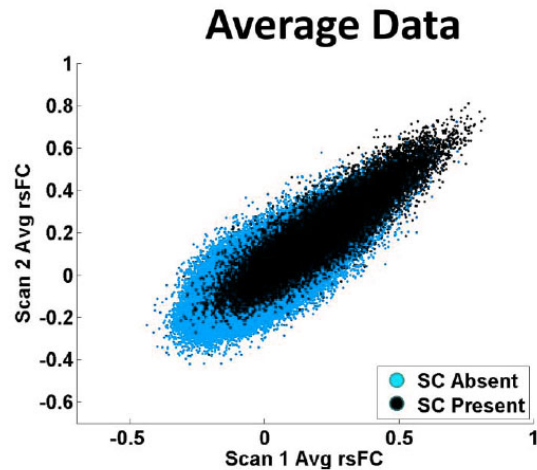
Figure 7.5: Increased reliability of rsFC mediated by SC. The scatter plot shows rsFC from Scan 1 against rsFC from Scan 2, using high-resolution data for participant-averaged SC and rsFC maps. Region-pairs with present SC in black, region-pairs without SC in blue.

Reliability of rsFC

As rsFC is acquired from each participant on two separate occasions (20- and 15-min scans), we are able to examine the reliability of rsFC. Reliability is operationalized as the correlation between 2 sets of rsFC values. For individual participants at the high resolution, reliability across scans ranges from r=0.38 to r=0.69, and reliability across two 10-min windows within the first scan ranges from r=0.39 to r=0.61. Unexpectedly low reliability is also observed in our computational model: across two consecutive 8-min windows within a single run, the simulated rsFC reliability ranges from r=0.69 to r=0.80 for individual maps at the high resolution. In models and in data the observed reliability is lower than would be expected based on the sample size (at least 200 time points per window) and distributions of rsFC. Some of the empirical variability is likely because of acquisition and registration artifacts. However, we note that both empirical [233] and simulated rsFC time series exhibit very long-range temporal autocorrelations (or, equivalently, substantial power in very low frequencies), which effectively reduce the number of independent measurements captured within a time window. The values of rsFC measured in this study, as well as more generally in the field, may therefore not reflect a static underlying entity. We also note that ROI pairs with SC exhibit significantly less variability in empirical rsFC (both across and within sessions) than do ROI pairs without SC (see Figure 7.5). In the present data we cannot distinguish whether rsFC between these ROIs is more persistent because it is stronger (and therefore, statistically, less subject to sampling variability in finite samples), or whether it is stronger because it is more persistent (that is, because the underlying interaction is more stable). In either case, the effect is mediated by the strength of the anatomical connections between pairs.

SC and rsFC in the DMN

On an area-by-area basis (Figure 7.4B), correlations between simulated and empirical rsFC are highest for many regions located in the posterior medial cortex, including the precuneus and posterior cingulate cortex, and the medial orbitofrontal cortex. Using previously published focal coordinates of the DMN [67] within the precuneus/posterior cingulate, the medial prefrontal cortex, and the lateral parietal cortex as seed points, we extract a subset of ROIs most strongly correlated with ROIs located in the DMN. Figures 7.4C and 7.4D portray the relationship of SC to rsFC within the DMN. We find strong SC linking the 2 medial portions of the precuneus/posterior cingulate and medial prefrontal cortex, both interhemispherically and along the medial walls of the cerebral cortex. Lateral parietal cortex is linked through parieto-frontal pathways, while anatomical links to medial parietal cortex are less dense (see Figure 7.4D). Connections between lateral and medial aspects of the posterior parietal cortex are observed in tracer studies [162], and the weakness of this connection in the DSI data likely reflects the difficulty of tracking fibers perpendicular to bundles such as the superior longitudinal fasciculus. Consistent with the structural DSI data supplied to the model, the simulated rsFC seeded in the DMN reproduces empirical rsFC patterns along the medial axis, but largely fails to include lateral parietal cortex.

7.4 Discussion

Computational work has suggested that the underlying anatomical architecture of the cerebral cortex, including its cluster structure, shapes resting-state functional connectivity on multiple time scales [75, 108]. Advances in diffusion imaging [78, 112] now enable us to empirically examine this structure-function relationship in individual humans at high spatial resolution across the cerebral cortex, and to compare a variety of systems-level features of resting-state functional connectivity against the predictions of computational models informed by the underlying anatomical network.

Earlier work had shown that interhemispheric rsFC is diminished in cases of callosal agenesis [171], is related to callosal integrity in healthy individuals [169], and is almost entirely abolished acutely after callosotomy [117, 217]. Structural and functional connectivity were also shown to be correlated in adjacent cortical regions in a single axial slice [130]. The robust SC-rsFC relationship we now report at high spatial resolution provides further evidence that functional connectivity is reflective, at least in part, of interactions between distant neuronal populations. However, because anatomically unconnected edges exhibit a wide range of rsFC values, one cannot simply infer SC by thresholding maps of rsFC. The difficulty of inferring SC from rsFC arises because (i) rsFC can result from mechanisms other than direct SC, and (ii) the base rate of direct SC between 2 randomly selected ROIs at the high resolution is very low. This difficulty is not simply a reflection of the practical limitations of fMRI, because inference is nearly as difficult within our computational model, in which SC provides the exact coupling matrix, as in empirical data.

Our second finding is that both SC and rsFC tend to decrease with interregional distance (consistent with previous studies of SC [120, 141] and rsFC [177]) and that a significant portion of the rsFC variance unexplained by SC alone is explained when distance information is combined with SC information in a bivariate model. Because interregional

distance can be expected to influence sources of rsFC that are neuronal (e.g., the strength of SC, and activation spread across the cortical surface [175]) as well as nonneuronal (e.g., cardiac, vascular, acquisition and preprocessing artifacts [189]), we cannot definitively determine the origin of this distance-related residual variability in rsFC. We note, however, that although our computational model incorporates only topological (and not explicitly spatial) coupling, it exhibits a distance-associated decrease in rsFC that resembles the empirically observed fall-off. It is therefore not necessary to invoke mechanisms beyond the topology of cortico-cortical projections in explaining the distance effects.

None of the results we report in this study can be fully accounted for by interregional distance, but many are mediated by it, and the prevalence of nearest-neighbor (i.e., lattice-like) anatomical connectivity of the cerebral cortex is fundamental to its small-world [2, 17, 78, 157] (see also Chapter 9) and hierarchical [89, 119] properties. Another factor contributing to the local clustering in rsFC networks is that indirect SC induces rsFC between region pairs that lack direct anatomical linkage. The relationship between indirect SC and rsFC is weaker than that between direct SC and rsFC, but is highly significant.

Our third finding is that rsFC exhibits unexpectedly low reliability within and across scanning sessions. This phenomenon is observed in each participant, as well as in our model, which is not susceptible to physiological or acquisition artifacts. In empirical data, we also observe that ROI pairs linked by SC exhibit more reliable rsFC, so that highly interconnected systems such as the DMN are nevertheless quite persistent. Within our data we cannot determine whether the shifts in rsFC reflect reconfiguration of neuronal interactions, are the result of low-frequency signal components of unknown origin, or result from a combination of the two. It is clear, however, that the proportion of the variance in rsFC that is explained by SC must be understood in light of the fact that fMRI rsFC is not static on the timescales used in this and other resting-state fMRI experiments. Studies which compare fMRI FC against FC in modalities with higher sampling rates [99, 146, 220] remain crucial in determining the potential cognitive and behavioral significance of slow correlated fluctuations in the BOLD signal.

The rsFC of some highly connected regions is matched with high fidelity (see Figure 7.4B), and this is found in particular within the posterior medial components of the default mode network (see Figure 7.4C and 7.4D). This is likely a consequence of the fact that there is a dense anatomical subnetwork linking DMN member regions [30, 84]. In future modelling work it may be fruitful to investigate how dynamical properties of individual nodes vary as a function of the nodes network embedding. Large-scale cortical models will also be improved when we have access to interregional physiological efficacies, rather than fiber strengths, which only approximate the effective couplings between neuronal populations. It is also important that future models include the thalamus [113, 193] as well as the basal ganglia, which likely mediate diverse cortico-cortical interactions. By limiting ourselves in the present model to aggregate neural dynamics at each node, and by only including cortico-cortical couplings, we have been able to identify systems-level features of empirical rsFC that can be explained without recourse to subcortical input or specialized local circuitry.

The robust correspondence between SC and rsFC measured in independent imaging modalities provides a degree of mutual methodological validation for our SC and rsFC acquisition methods. Nevertheless, the potential for interregional variability in the reliability of these methods limits our ability to examine interregional differences in the

strength of the structure-function relationship. While DSI tractography is often successful in resolving crossing fibers, the detection of relatively small fiber bundles running perpendicular to major fasciculi, as well as the reliable detection of very long fiber bundles, remains a technical challenge. Functional MRI is subject to susceptibility artifacts, especially in baso-temporal regions and near the frontal pole, and BOLD correlations can be contaminated by vascular, respiratory, and preprocessing artifacts [233].

Structural connectivity of the adult mammalian brain is essentially constant from day to day, but functional connectivity can substantially reconfigure [17] within a few hundred milliseconds. In this study we confirm [108,130] at high resolution that the organizations of SC and of rsFC are strongly interrelated: structurally connected cortical regions exhibit stronger and more consistent rsFC than structurally unconnected regions. However, we also demonstrate, and capture in quantitative models, the fact that robust functional connectivity can be found between regions not linked by cortico-cortical projections, that spatial auto-correlation in functional connectivity likely results from underlying anatomy, and that functional networks continually reconfigure around the underlying anatomical skeleton. The timescales on which rsFC changes, and the relation of these changes to cognition, are important questions for future inquiry.

7.5 Conclusion

In this chapter, we have investigated the relationship between the structural connectivity obtained from diffusion MR tractography and the functional connectivity obtained from resting-state functional MRI. We have observed that although resting-state functional connectivity is variable and is frequently present between regions without direct structural linkage, its strength, persistence, and spatial statistics are nevertheless constrained by the large-scale anatomical structure of the human cerebral cortex.

The correlation between resting-state functional connectivity and structural connectivity can be seen as a partial validation tool for MR tractography. It allows to quantitatively evaluate the human connectome, enabling for example the performance comparison of various tractography algorithms. In the next chapter, we show that this measure can also be used in combination with other evaluation methods in order to better understand the methodological limitations associated to the construction of the human connectome.

A Connectome-Based Evaluation of Diffusion MR Acquisition Schemes

8

8.1 Introduction

We remember from Chapter 2 that several acquisition schemes have been developed in order to map the diffusion in the human brain. As mentioned earlier, the well-known Diffusion Tensor Imaging (DTI, [14]) provides a simple but practical method to map the orientation of the fibers by fitting a tensor model on the diffusion data. However, it fails to correctly map diffusion in voxels where two or more fiber populations interfere. Several methods have been proposed to address this issue.

Q-Ball imaging (QBI, [215]) is a reconstruction scheme which measures the angular structure of the diffusion spectrum. It has been shown to allow the mapping of more complex diffusion structures in areas of "crossing" and "kissing" fibers, such as the intersection between the optic radiation and the splenium of the corpus callosum, the Meyer's loop or the middle temporal gyrus [213].

Another high angular resolution reconstruction scheme is the Diffusion Spectrum Imaging (DSI), which measures the diffusion spectrum by sampling the $\mathbf{q}$-space [92, 226, 227]. This method was validated with phantoms made of parallel capillaries filled with water, as well as with manganese-enhanced rat optic tracts. The results showed that the crossing fiber orientations estimated with DSI were in excellent agreement with the results from histology [142, 182]. Moreover, a comparison with DTI data showed that the accuracy of DTI deteriorates in the presence of a fiber crossing [228].

Though there is no doubt concerning the great potential of high angular resolution diffusion imaging to better disentangle complex fiber structures compared to DTI, the gain

at the level of *in vivo* whole-brain tractography is still not clearly quantified. In 2007, Behrens et al. suggested that the tractography performed using high angular resolution diffusion acquisitions should increase the sensitivity as compared to DTI, especially for non-dominant fiber tracts [21]. More recently, Wedeen et al. [228] made a comparison between DSI and DTI tractography based on adult macaque and human brains. They showed a significant improvement with DSI in the mapping of crossing fibers, especially in complex fiber crossing areas such as the optic chiasm, the centrum semi-ovale or the brainstem. However, comparing DTI and high angular resolution approaches such as DSI and QBI is still a poorly understood topic. What is the best acquisition method for tractography? Is the type of diffusion acquisition significantly affecting the mapping of the human connectome as it is proposed in this thesis? Is the DSI scheme more efficient than the QBI scheme, because of the acquisition of the diffusion measurements on multiple shells in the **q**-space? All these questions are of the highest importance, since a better understanding of the relationship between the acquisition and the resulting tractography would help in selecting the adequate diffusion scheme for a given application.

In this work, we address some of the above mentioned questions by performing a connectome-based comparative study of various diffusion acquisitions. This presents a challenge, as the methods differ quite significantly in a number of acquisition parameters such as overall scan time and used *b*-value. To be able to compare the results, we need to find a common description. Thus, we aim at comparable SNR properties and use the connection matrix as a mean to investigate differences between the techniques. The connection matrix appears to be an elegant way to compare the methods, since the outcome represents clinically relevant information. In other words, this metric allows us to omit differences in the technique that may exist but do not reflect a practical relevance, and rather focus on useful measures. Practically, we proceed by comparing the connection matrices obtained from three diffusion techniques: DSI, QBI and DTI. We evaluate and quantify the performances in terms of brain connectivity by using global network measures, by studying anatomically selected fiber tracts and by examining the relationship between structural and functional connectivity. Using those measurements, we show that the three acquisition schemes exhibit clear differences. We analyze the factors responsible for those differences. However, we emphasize that ultimately the choice of the acquisition scheme depends on the application.

8.2 Material and methods

MRI acquisitions

After written informed consent and in accordance with our institutional guidelines and ethics committee, five healthy female volunteers from 22 to 30 years old were scanned with a Siemens TimTrio 3T scanner and a 32-channel receive head matrix coil. Five diffusion acquisitions were performed on two separate days (at approximately one week interval), as follows: two DSI scans with 258 directions, sampling the **q**-space by taking the points of a cubic lattice within a hemisphere whose radius is 5 lattice units (DSIq5 (1) and (2), acquired both at day 1 and day 2), one DSI scan with 129 directions, sampling the **q**-space by taking the points of a cubic lattice within a hemisphere whose radius is 4 lattice units (DSIq4, two averages), one QBI scan with 257 directions and one DTI scan with 65 directions (4 averages) with encoding gradients uniformly distributed over a sphere. For

	DSI q5	DSI q4	QBI	DTI
TR (ms)	6000			
TE (ms)	138		110	89
B-value (s/mm^2)	8000 (max.)	6400 (max.)	3000	1000
Encoding gradients	258	129	257	65
Acquisition block (pixels)	96 x 96 x 34			
Spatial resolution (mm)	2.21 x 2.21 x 3			
Number of averages	1	2	1	4

Table 8.1: Parameters of the diffusion acquisitions.

all acquisitions, a diffusion weighted single shot spin echo EPI sequence was used [174]. All the acquisitions used the same field of view and spatial resolution. To match SNR between the scans the acquisition time was kept constant (approx. 26 minutes), i.e. the DTI scan resulted from the **q**-space complex averaging [77] of four individual DTI scans. Similarly, the DSIq4 was obtained with two averages. The sequence parameters are summarized in Table 8.1. In addition, a high-resolution T1-weighted (MP-RAGE) MRI was performed in a matrix of 256 x 256 x 128 voxels of isotropic 1mm resolution.

Structural connection matrices

The structural connection matrices are obtained using the procedure described in Chapter 4 and briefly summarized below.

First, the high-resolution T1 acquisition is registered on the diffusion images using an affine registration method [192, 230] (http://www.fmrib.ox.ac.uk/fsl/). Next, the gray matter is partitioned into 66 anatomical regions and 998 small regions of interest (ROIs). Since the diffusion data are acquired in two separate days, the partition obtained from the T1-weighted scan has to be registered in order to correspond to the diffusion acquisitions performed on day 2. Assuming that the shape of the brain does not change between the scans, we use a simple rigid-body registration on the b0 image of the diffusion scans.

Next, the DSI and QBI data are reduced into the Orientation Density Function (ODF, see Section 2.6) using the Trackvis software (http://www.trackvis.org). For each voxel a set of vectors corresponding to the local maxima of the ODF is built. For DTI data, the tensor field is computed (also using Trackvis) and the first eigenvector is extracted. White matter (WM) tractography is performed with the streamline algorithm described in Chapter 4, using the set of vectors obtained from each data set. In every WM voxel, 32 fibers are generated along each vector contained in the set. The fibers stop expanding when the end-points reach the WM-GM interface.

Finally, we build the high-resolution (998 ROIs) and low-resolution (66 areas) connection matrices for every acquisition, by computing the fiber density connecting every pair of ROIs. We remember that the fiber density is defined as the number of fibers connecting a pair of ROIs, normalized by the surface of the ROIs and by the length of the fibers (see Section 4.3 for more details).

Functional connection matrices

In addition, during the second scanning session subjects underwent a resting state experiment using a gradient echo EPI sequence (TR = 1920 ms, TE = 30 ms). Participants were instructed to keep their eyes open and to remain alert. Thirty-two slices of 3 mm thickness with a 0.3 mm gap were acquired, using an axial plane with a field of view of 211 x 192 mm (64 x 58 voxels, each 3.3 x 3.3 mm in-plane). All participants were scanned twice with the resting state protocol on the same day (2 x 8 minutes). The post-processing procedure is identical to the one presented in Chapter 7. Briefly, raw BOLD signals are registered and resampled onto the b0 image of the DSIq5 scan using rigid-body registration. BOLD time series are computed for each of the 998 ROIs by averaging across the ROI voxels. Then, ROI BOLD time series are piecewise-linearly detrended (every 50 s) and mean cortical, ventricular, and white matter signals are regressed. Pearson correlations are calculated between all ROI-pairs, and averaged over the two separate scans. Note that for structure-function comparisons, the structural connection matrices representing the fiber density are resampled following a Gaussian distribution, using the method described in Section 7.2.

8.3   Results

Global network measures

We first turn our attention to the global connectivity obtained with the high-resolution (N=998) connection matrices. The number of connected edges (defined as the edges having a non-zero connection density, see Chapter 6), are reported in Table 8.2 (top section), for the five subjects and for all diffusion scans. Since the global connectivity slightly varies among the subjects, we further report in Table 8.2 (bottom section) and in Figure 8.1 the connected edges normalized to the DSIq5 scan of day 1, called normalized connectivity in the following. Recall, since the DSIq5 scan was performed in each session, the day 2 DSIq5 scan provides a measure of reproducibility of the technique. Furthermore, paired t-tests are performed on the number of connected edges (null hypothesis: the samples come from distributions with equal means). The obtained p-values are reported in Table 8.3.

First, we notice that the difference between the two DSIq5 scans is minimal, since the normalized connectivity of the day 2 scan is of 98.4% on average. The paired t-test shows that the difference in terms of number of connected edges is not statistically significant. This is very important, since it demonstrates that variances in the acquisition and processing, e.g. the rigid-body registration applied to the cortex partitioning for the day 2 scans, do not significantly affect the calculated connectivity. Second, we can see that with the QBI and DTI scans the connectivity is significantly decreased as compared to the connectivity found by using DSIq5 (22.9% and 25.4% respectively). According to the paired t-test reported in Table 8.3, QBI and DTI connectivity can not be statistically differentiated, whereas for all other pair of scans the differences in terms of the number of connected edges are statistically significant. We consistently find lower numbers of connections for the DSIq4, QBI and DTI scan. Finally, we notice that the DSIq4 obtains an intermediate score, with a normalized connectivity of 83.6%. However, it is important to note that higher connectivity does not necessarily mean better connectivity. The
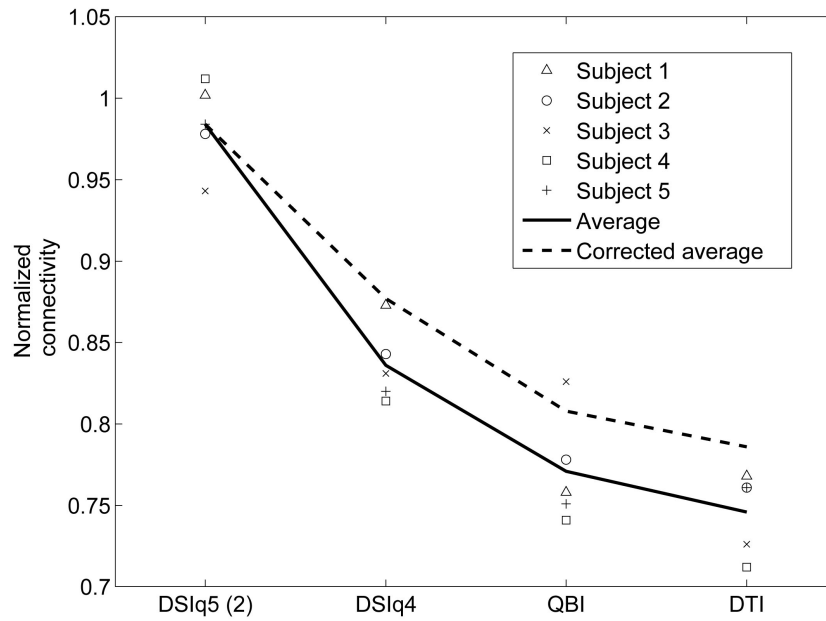
Figure 8.1: Average normalized connectivity (solid line) and average normalized connectivity corrected for the number of fibers (dotted line).

Subject	DSIq5 (1)	DSIq5 (2)	DSIq4	QBI	DTI
1	10042	10061	8768	7607	7717
2	11149	10904	9403	8678	8488
3	11007	10379	9146	9087	7991
4	10831	10963	8812	8021	7715
5	10261	10100	8416	7707	7809
1	1	1.002	0.873	0.758	0.768
2	1	0.978	0.843	0.778	0.761
3	1	0.943	0.831	0.826	0.726
4	1	1.012	0.814	0.741	0.712
5	1	0.984	0.820	0.751	0.761
average	**1**	**0.984**	**0.836**	**0.771**	**0.746**

Table 8.2: Top section: number of connected edges for the five subjects and for all diffusion scans. Bottom section: proportion of connected edges relatively to the DSIq5 scan of day 1.

	DSIq5 (1)	DSIq5 (2)	DSIq4	QBI	DTI
DSIq5 (1)	-	0.25	$1.59e^{-4}$	$7.36e^{-5}$	$6.12e^{-5}$
DSIq5 (2)	0.25	-	$6.80e^{-4}$	$1.11e^{-3}$	$1.43e^{-4}$
DSIq4	$1.59e^{-4}$	$6.80e^{-4}$	-	$1.79e^{-2}$	$5.94e^{-4}$
QBI	$7.36e^{-5}$	$1.11e^{-3}$	$1.79e^{-2}$	-	0.28
DTI	$6.12e^{-5}$	$1.43e^{-4}$	$5.94e^{-4}$	0.28	-

Table 8.3: P-values resulting from the paired t-tests performed on the number of connected edges.

added connections may be due to noise or some other artifacts, and those results have to be interpreted with the help of the other measurements performed in this work.

One could argue that the higher connectivity found for the DSIq5 scans is due to the number of generated fiber tracts. Indeed, since the number of fiber initialization points is proportional to the number of local maxima of diffusion, the number of generated fiber tracts is systematically higher for the DSIq5 scans as compared to the DTI scans, for which there is only one local maximum per voxel. This bias inherent to the tractography technique may explain the noticed differences between the scans. In order to test this hypothesis, we define a fixed number of fibers for each subject (arbitrarily defined as 85% of the number of fibers obtained with the DTI scan tractography). Then, for every subject and diffusion scan, we randomly suppress fibers from the corresponding tractography result until the desired number of fibers is reached. Next, we recompute the connection matrices, ensuring that each of them is built with the same number of fibers. The resulting average normalized connectivity is shown in Figure 8.1 (dotted line). Although we can see a small increase in the normalized connectivity, our initial observations remain valid. This indicates that the number of generated fiber tracts only explains a small part of the noticed connectivity differences.

Next, we focus on the edge distance l_e, defined as the geodesic distance in the brain WM (i.e., the shortest path being confined in the WM mask) separating the pair of ROIs linked by the edge e. In Figure 8.2, we report the edge distance distribution for the various acquisition schemes (summed over the five subjects). We can see that the edge distance distribution obtained with the DSIq5 scan has the heaviest tail, which tends to indicate that it maps more associative connections (mid- and long-range fibers) than the other acquisition schemes. In contrast, the QBI and DTI scans results show a much shorter edge distance. Again, the DSIq4 scan exhibits properties that are a kind of trade-off between the DTI and DSIq5 characteristics. Moreover, we notice that the biggest differences between the DSIq5 scan and the other diffusion scans are in the range 60-90mm. On average, the normalized connectivity for this range of distance is only of 66% for DSIq4, 50% for QBI and 43% for DTI.

Selected tracts

The low-resolution connection matrices representing the fiber density obtained with the five acquisition schemes for subject 4 are mapped in Figure 8.3A-E (the other subjects produce similar results, data not shown). Although the global shape of these matrices is similar, several differences can be noticed. First, the number of inter-hemispheric
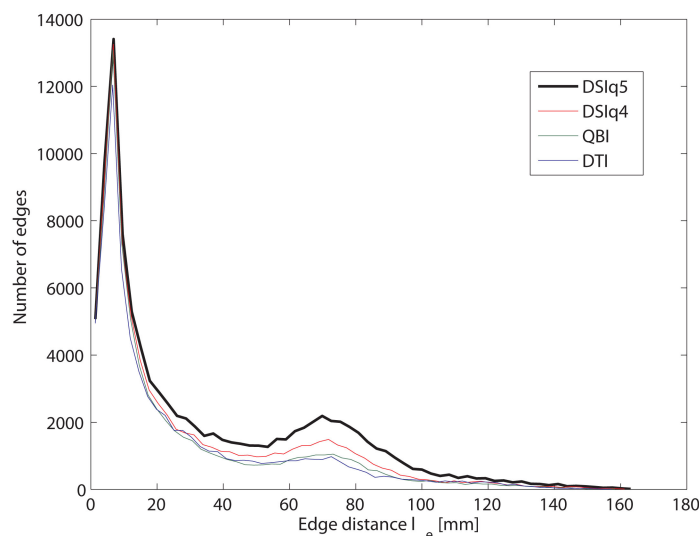
Figure 8.2: Edge distance distribution for the tractography results obtained with DSIq5 (black), DSIq4 (red), QBI (green) and DTI (blue). The edge distance distribution is obtained from the sum over the five subjects.

connections (red box) varies among the different scans. By ordering the scans by increasing number of inter-hemispheric connections, we find the DTI, followed by the QBI, the DSIq4 and finally the DSIq5 scan. This is in agreement with the normalized connectivity measurements. Fibers of the corpus callosum are plotted in Figure 8.4 for the various acquisition schemes. We can see that the DTI scan only captures the fibers whose endpoints lie in the apical part of the cortices. The DSI scan allows to map more lateral projections, especially in the frontal and parietal cortex. Interestingly, both the DSIq4 and QBI scans give results very close to those obtained with the DSIq5. This tends to indicate that the major tracts, characterized by large and dense axonal bundles, do not necessarily require a DSIq5 scan to be accurately mapped.

As additional examples we identify in the connection matrices of Figure 8.3 two association bundles: the arcuate fasciculus (green box) and the superior longitudinal fasciculus (orange box). For both fiber tracts, we can see that the number of connections is much higher with the DSIq5 scan than with the DTI scan, the QBI and DSIq4 scans providing an intermediate performance. This is confirmed by looking at Figure 8.5, where both tracts are mapped with the four acquisition schemes. For these association bundles, we notice that the DTI scan is unable to provide realistic fiber tracts. This is not surprising since those tracts are running through complex crossings areas. The DSIq5 well captures the global shape of these tracts and shows here a significant advantage over the QBI and DSIq4 scans.

Correlation with resting state fMRI

We now focus on the relationship between structural (SC) and resting-state functional connection (rsFC) matrices. We report in Table 8.4 (top section) the individual SC-rsFC correlations at the high resolution (N=998 nodes) for all region pairs. The correlation
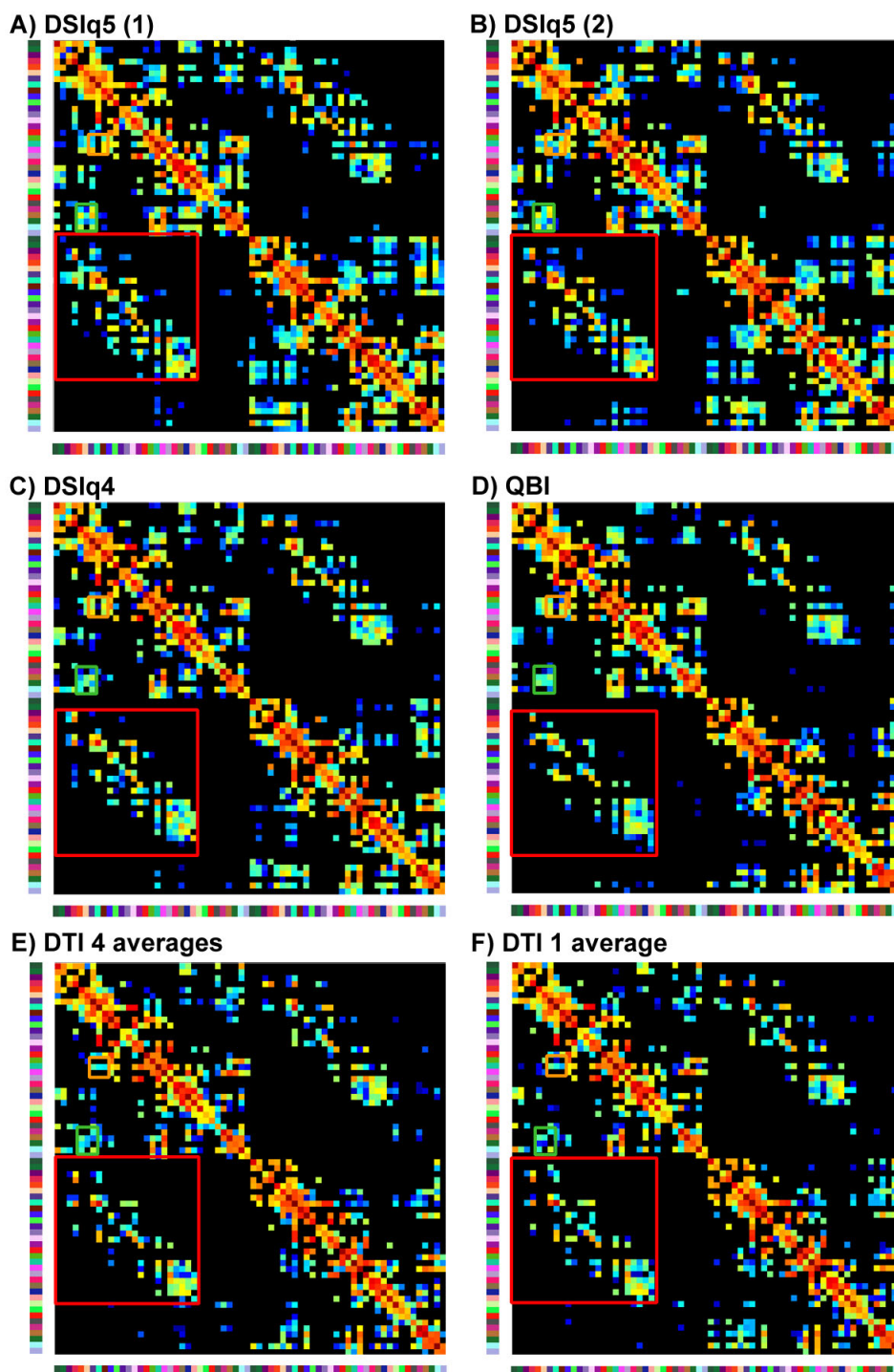
Figure 8.3: Low-resolution connection matrices for the various acquisition schemes (Subject 4). X and Y axis color bars represent the color code of the Freesurfer areas (see Figure 4.4). Three tracts are identified: the corpus callosum (red), the arcuate fasciculus (green) and the superior longitudinal fasciculus (orange).
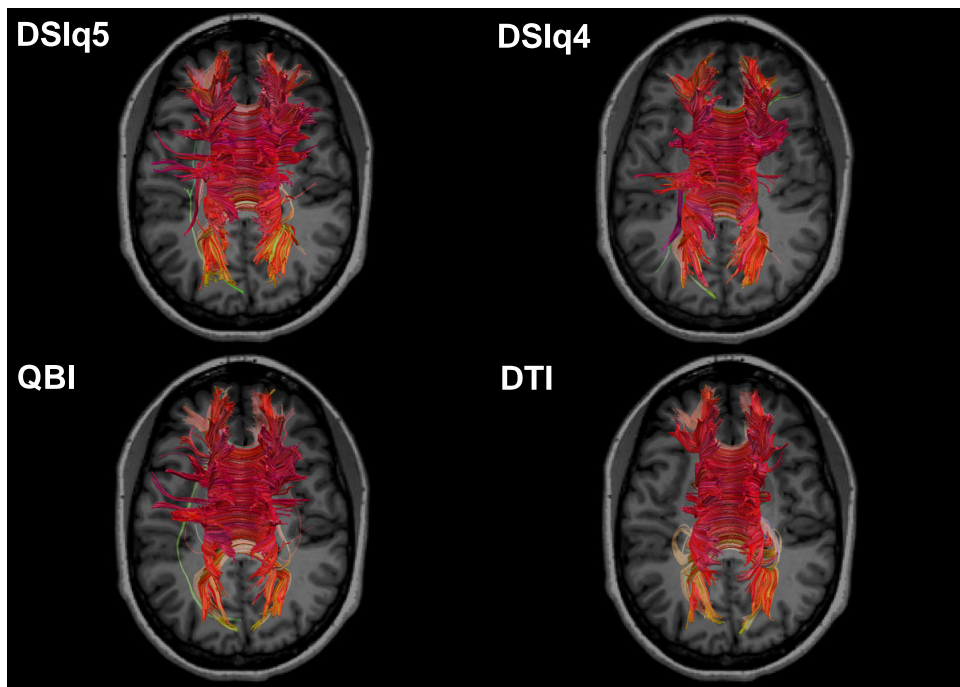
Figure 8.4: The corpus callosum mapped with the various acquisition schemes. This tract is obtained by selecting fibers whose end-points lie in the area delineated by the red box drawn in the connection matrices of Figure 8.3.

values obtained for all region pairs are very similar among the various acquisition schemes. This can be explained by three factors. First, the connection matrices are very similar for all diffusion scans, and therefore there is no reason to observe big differences in the correlation values. Second, the structural connection matrices are sparse, and consequently the potential differences among the various diffusion scans are averaged over the total number of region pairs. Third, the resting state analysis has a limited power and thus acts like a filter on subtle differences in the underlying structural basis.

Accordingly, we compute the correlation only for region pairs with SC, reported in Table 8.4 (bottom section) and in Figure 8.6. Furthermore, paired t-tests are performed on the SC-rsFC correlations for region pairs with SC (null hypothesis: the samples come from distributions with equal means). The obtained p-values are reported in Table 8.5. We can see that the DSIq5 scan tends to be more highly correlated than the other scans, with an average correlation of 0.44. Next, we find the DSIq4 scan, with a correlation of 0.42. Finally, the QBI and DTI scans obtain an average correlation of 0.40 and 0.39 respectively. This suggests that the DSIq5 scan benefits from a higher sensitivity. It is important to note that the inter-subject variability is relatively high, and that a bigger group of subjects would be recommended to confirm those observations. However, the obtained results are highly consistent with the global network measures presented above. Moreover, we can see in Table 8.5 that the differences among the scans are statistically significant, except between DSIq5(1) and DSIq4 (probably because of the limited number of subjects) and between QBI and DTI. This suggests that the global tendency observed in Figure 8.6 is reliable.
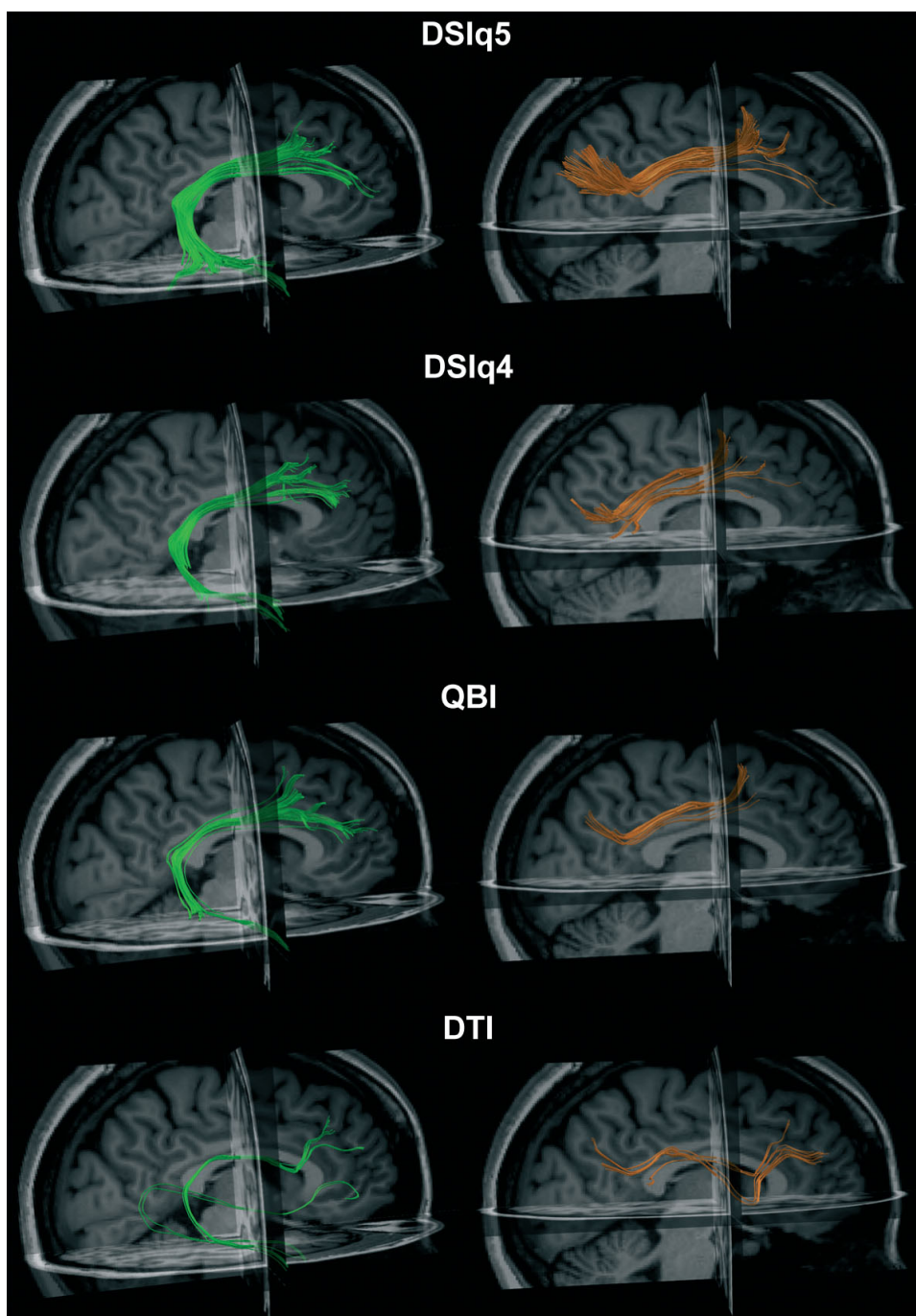
Figure 8.5: Arcuate fasciculus (left) and superior longitudinal fasciculus (right) mapped with the various acquisition schemes. These tracts are captured by selecting fibers whose end-points lie in the areas delineated by the boxes drawn in the connection matrices of Figure 8.3 (green: AF, orange: SLF).

Subject	DSIq5 (1)	DSIq5 (2)	DSIq4	QBI	DTI
All region pairs					
1	0.200	0.203	0.205	0.196	0.188
2	0.167	0.169	0.166	0.168	0.165
3	0.197	0.199	0.192	0.188	0.178
4	0.168	0.171	0.178	0.177	0.175
5	0.177	0.187	0.182	0.184	0.170
average	**0.182**	**0.186**	**0.185**	**0.183**	**0.175**
Region pairs with SC					
1	0.458	0.449	0.431	0.392	0.419
2	0.401	0.418	0.402	0.392	0.368
3	0.475	0.457	0.437	0.415	0.407
4	0.427	0.448	0.420	0.404	0.376
5	0.417	0.416	0.407	0.401	0.393
average	**0.436**	**0.438**	**0.419**	**0.401**	**0.393**

Table 8.4: Individual participant and average SC-rsFC correlations for all region pairs (top section) and for region pairs with SC (bottom section). All correlations are $P \ll 1e^{-3}$.

	DSIq5 (1)	DSIq5 (2)	DSIq4	QBI	DTI
DSIq5 (1)	-	0.80	$8.49e^{-2}$	$4.16e^{-2}$	$6.14e^{-3}$
DSIq5 (2)	0.80	-	$4.07e^{-3}$	$7.43e^{-3}$	$7.92e^{-3}$
DSIq4	$8.49e^{-2}$	$4.07e^{-3}$	-	$3.23e^{-2}$	$1.51e^{-2}$
QBI	$4.16e^{-2}$	$7.43e^{-3}$	$3.23e^{-2}$	-	0.48
DTI	$6.14e^{-3}$	$7.92e^{-3}$	$1.51e^{-2}$	0.48	-

Table 8.5: P-values resulting from the paired t-tests performed on the SC-rsFC correlations for region pairs with SC.

The effect of the q-space averaging

In order to perform a fair comparison between the scans, the acquisition time is matched for all diffusion scans. However, one of the advantages of the DTI and DSIq4 protocols is the shorter acquisition time (25% and 50% respectively). As the analysis of the individual scans is of high interest, we report here on the performance comparison between the **q**-space averaged DTI and DSIq4 scans with the individual scans.

For both the DTI and the DSIq4 scans, the number of connections is found to be slightly higher in the individual scans than in the averaged scans (presumably mild subject motion), as shown in Table 8.6 (top section). However, the differences are relatively small, as can be seen by comparing the low-resolution matrices calculated from the DTI 4 averages scan (Figure 8.3E) and the individual DTI scan (Figure 8.3F). Furthermore, those differences have no impact on the SC-rsFC correlations for region pairs with SC (paired t-test, p=0.53 and p=0.81 respectively), as reported in Table 8.6 (bottom section).
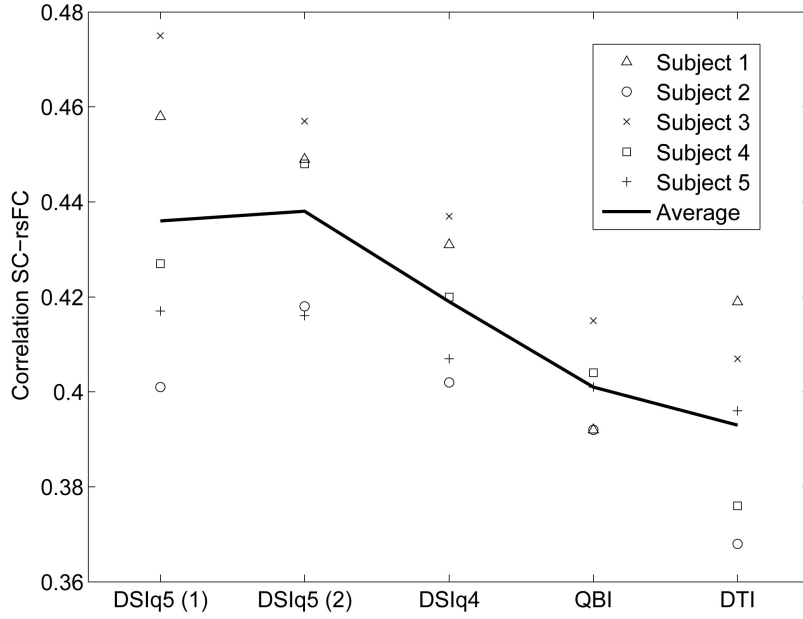
Figure 8.6: Average correlation for region pairs with SC at the high resolution (solid line). The symbols indicate the correlations obtained for each individual subject.

Subject	DSIq4 2av	DSIq4 1av	DTI 4av	DTI 1av
Number of connections				
1	8768	8766	7717	7834
2	9403	9470	8488	8689
3	9146	9353	7991	8169
4	8812	9560	7715	7898
5	8416	8923	7809	7920
SC-rsFC correlations (HR, region pairs with SC)				
1	0.431	0.419	0.419	0.405
2	0.402	0.391	0.368	0.381
3	0.437	0.438	0.407	0.402
4	0.420	0.445	0.376	0.376
5	0.407	0.395	0.396	0.386

Table 8.6: Comparison of individual and averaged DTI and DSIq4 scans. Top section: number of connections. Bottom section: SC-rsFC correlations for region pairs with SC. All correlations are $P \ll 1e^{-3}$.

8.4 Discussion

This comparative study helps us to better understand the influence of the acquisition scheme on the performance of whole-brain tractography. First, we demonstrate that the DSIq5 scan, which acquires 258 encoding directions in the **q**-space, maximizes the number of connected edges in the connection matrices. This is confirmed by the visual analysis of well-known fiber tracts. The increased performance obtained for the SC-rsFC correlation indicates that these additional connections correspond to real anatomical fiber tracts, and not to added noise. These results suggest that the DSI technique has a higher sensitivity to map the fiber pathways in the brain WM. Second, we show that the performances of the DTI scan are strongly limited by the underlying Gaussian model: about one fourth of the connections obtained with the DSIq5 scan are not mapped with DTI, even as high as 57% for connections in the distance range 60-90mm. The consequences are significant, since even well-known association bundles, such as the arcuate fasciculus or the superior longitudinal fasciculus, are not as comprehensively mapped. The two other scans, i.e. the QBI and the DSIq4 scans, exhibit intermediate results.

Interestingly, the QBI scan does not show significant improvements as compared to the DTI scan. On one hand, the angular structure approach of the QBI technique combined with a higher b-value provides additional information about the non-dominant fiber populations present inside the fiber crossing areas. On the other hand, this higher b-value also increases the amount of noise. Our results tends to indicate that the potential gain associated to the additive orientational information is counteracted by the higher level of noise. In contrast, the DSIq4 performs better although the number of encoding gradients is reduced by a factor two. This suggests that acquiring the diffusion signal on multiple shells in the **q**-space significantly improves the accuracy of diffusion measurements as compared to a single shell acquisition. Moreover, the single average data perform equally to the averaged data, as shown in Table 8.6. Consequently, the suggested protocol for the whole-brain DSIq4 experiment would require a scan time of 12-13 minutes, which becomes clinically more realistic than a full DSIq5 scan of more than 25 minutes acquisition time.

We can see that the biggest differences between the DTI, DSIq4 and DSIq5 scans are found for mid-range connections, i.e. connections with a length between 60 and 90 mm. This can be explained as follows. First, we know from anatomy that the long-range associative, striatal and commissural fiber tracts are composed of relatively big and tightly packed axonal bundles. Consequently, those tracts are dominant as compared to the smaller fiber tracts that may cross their trajectory, suggesting that even a DTI scan may capture them. Therefore, we do not expect major differences in long-range connectivity among the various acquisition techniques. Second, we know from Chapter 6 that short-range connectivity is partially due to random effects, that arise in any tractography experiment independently from the diffusion acquisition. Consequently, it is highly likely that short-range connectivity is similar in all the acquired data sets. The mid-range connections consist mainly in short association fibers, connecting pair of regions inside the same or adjacent gyrus, and neighboring association fibers, connecting pair of regions inside the same lobe [181, 183]. Those connections are precisely non-dominant fiber populations, for which high angular resolution is theoretically capable to disentangle more comprehensively pathways. This may explain the differences found for this category of connections.

Interestingly, it turns out that averaging multiple diffusion scans, as applied in the DSIq4 and DTI scans, does not improve the mapping of the human connectome. Although the signal-to-noise ratio is better in the averaged raw diffusion images, its influence on the tractography is negligible, suggesting that the impact of the **q**-space complex averaging on the reconstruction of the ODFs (or the tensor in the case of DTI) is limited. A possible explanation could be that the high number of encoding gradients used both for the DTI and the DSIq4 scans (64 and 129) already acts as an averaging factor when reconstructing the tensors or the ODFs. If this is the case, the effect of averaging should be noticeable for protocols with a lower number of encoding directions. Further work is necessary to better understand this phenomenon.

All diffusion scans used in this work, from the individual DTI scan to the high-angular resolution DSI acquisition, produce connection matrices that (i) have a similar distribution of connection densities and (ii) present roughly the same connection patterns. Moreover, all structural connection matrices obtain a correlation with rsFC of more than 0.36 for regions pairs with SC. This strong relationship [109] with the functional connectivity is of the highest importance: it tells us that although we notice some differences in terms of connectivity, all the diffusion scans result in a biologically meaningful mapping of the human connectome. Consequently, the choice of the optimal diffusion scheme depends on the application.

For clinical applications for which the acquisition time is an issue and which aim at creating scalar maps such as fractional anisotropy maps, a DTI scan can be an adequate solution. Similarly, to answer basic questions using tractography results DTI appears to be a capable technique. This is also the case for clinical studies particularly aiming at the investigation of large anatomical pathways, such as disconnection syndromes [38,39]. However, some precautions have to be taken when considering fiber tracts running through large fiber crossing areas, such as the arcuate fasciculus or the superior longitudinal fasciculus. In that case, a DSIq4 scan with an acquisition time of approximately 12 minutes should provide enough contrast to accurately identify the major bundles of the brain, and may turn out to be an optimal compromise between angular resolution and acquisition time.

As shown in this chapter, particular caution has to be used when investigating tracts of mid-range distance, that largely consists in non-dominant fiber populations. Those neighboring association fibers are of high interest in the study of plasticity, in the case of specific networks involving areas nearby, e.g. motor circuits in patients after stroke (post-stroke plasticity study; ongoing CHUV-Lausanne). In this context, high angular resolution diffusion imaging may be a promising technique to investigate the modification of the connectivity. For such studies, our observations show that the use of a DSI scan with 258 or more encoding gradients is preferable, though this needs more carefully control of data quality. Due to the particularly long scan time of this technique (25 minutes and more), it becomes very prone to motion artifacts that may significantly degrade the accuracy and the sensitivity of the method.

Methodological considerations

The parameters of the diffusion acquisitions deserve comment. In the specialized literature, it is striking to see the variability in the protocol settings, such as the number of encoding gradients or the maximal b-value. Since there is no consensus among the

scientific community, we define a "typical" protocol for each diffusion scan, by tuning the acquisition parameters according to recent diffusion MRI studies. For DTI, a b-value between 700 and 1300s/mm^2 and a number of encoding gradients ranging from 32 to 64 are commonly used and reported (see for example [118, 124, 208]). For the QBI scan, a b-value between 2500 and 3000s/mm^2 is recommended [132], with approximatively 250 directions [125, 213]. Typical DSI scans are achieved with 258 (DSIq5) encoding gradients with a b-value ranging between 8000 and 9000s/mm^2 [79, 90, 173]. Although changes in the protocols may slightly affect the results, it is highly likely that our observations remain valid for the range of typical settings.

As mentioned earlier, the subjects have to be scanned on two separate days due to the long acquisition time. Therefore, the registration applied to the cortical parcellation obtained with the high-resolution T1-weighted scan of day 1 may affect the results for diffusion scans of day 2. However, the results with the DSIq5 scans acquired on both days demonstrate that (i) the difference in terms of normalized connectivity is only of 1.6% and (ii) the average correlation with rsFC is equal (p-value of 0.80). This demonstrates an excellent scan rescan reproducibility. Consequently, we can affirm that the registration does not affect our observations.

The choice of the tractography algorithm is crucial, since several constraints have to be considered. First, we want the tractography algorithm to be the same for all diffusion scans. Therefore, we need to choose an algorithm that is suited for all diffusion scans, and that does not favor a specific type of input data. Second, as we want to perform global connectivity measurements, we need an algorithm for which the amount of false positive fibers is minimal. The chosen streamline algorithm meets all those requirements while being computationally very simple. An additional advantage of using this algorithm is that we already dispose of a complete study of the relationship between SC and rsFC (see Chapter 7) that can be used to evaluate the quality of our results. It is likely that more advanced tractography algorithms, such as front propagation algorithms, will show increased differences between the diffusion scans. However, those kind of approaches being strongly dependent on the input data type, it would be very difficult to perform an objective and fair comparison. Moreover, as mentioned in Chapter 5, the use of such complex methods for whole-brain connectivity studies is far from straightforward, because of the lack of efficient selection methods to discard the fibers arising from partial volume effects or noise.

In this work, we restrict to the analysis of DSI, QBI and DTI. However, other reconstruction schemes have been proposed. Assaf et al. have developed CHARMED, a composite hindered and restricted model of diffusion [10]. Tournier et al. have proposed the CSD technique [211], which estimates the fiber orientation distribution by using constrained spherical deconvolution. These methods tend to build a bridge between the tensor model and model-free reconstructions, and therefore have a great potential for optimized application-driven selection of a diffusion methodology. The acquired DTI data fulfill the requirements for the CSD method and may provide an interesting alternative to QBI.

8.5 Conclusion

In this chapter, we use several connectome-based measures to assess the performance of various diffusion acquisition schemes. These investigations help us to better understand the methodological limitations in the mapping of the human connectome. Whereas all

diffusion scans, from the classical DTI to the high-angular resolution DSI, produce a biologically meaningful mapping of the human connectome, the degree of complexity of the diffusion scheme significantly influences the sensitivity of tractography. The differences are particularly striking for non-dominant fiber populations, that run through complex fiber crossings. For this particular type of connections, a DSI scheme with 258 encoding gradients or more is recommended. However, depending on the application, a DTI scan may be preferable because of the shorter acquisition time, thus being less sensitive to motion artifacts.

In the last part of this thesis, we present two network-based applications of the human connectome. First, we analyze some basic properties of the human connectome and use the associated measures to demonstrate the small-world architecture of the brain. Then, with the help of network measurements we define the cortical areas that belong to the core of structural connectivity.

Part III

Applications

Network Topology and Properties of the Human Brain

9

9.1 Introduction

Biological neuronal networks, and in particular the human brain, are remarkable natural systems capable of complicated patterns of behavior. This capability seems possible due to the combination of an enormous computational capacity given by a huge amount of neurons, and a well designed communication network [135]. To understand the mechanisms behind higher-level brain functions, a detailed study of the individual neural cells is clearly insufficient [128]; global functional and structural properties of such a complex system need to be considered as well [207]. This requires, first of all, a good knowledge of the network architecture of the entire brain. A graph representing the connectivity of the brain (henceforth called a *brain network*) can be analyzed at various scales. Probably the most obvious is at the neuronal level, where each neuron is a separate node in the graph and connections between neurons are reflected by the edges. This detailed view, however, is feasible only for the most primitive animals such as C. elegans made of 302 neurons [43]. A graph of the human brain consisting of 10^{10} nodes and 10^{16} edges is not only impossible to obtain with current techniques, but it also would carry a great deal of information that is irrelevant from the global organization point of view. We must therefore resort to a different level of granularity, where a node represents thousands or millions of neurons grouped together.

Until recently, such available graphs were limited to small post-mortem data sets (only 50-70 nodes) of rat [34], cat [179, 180] and monkey [59] brains, whereas larger data sets of animal and human brains were missing [51]. As shown in Chapter 4, we now dispose of a
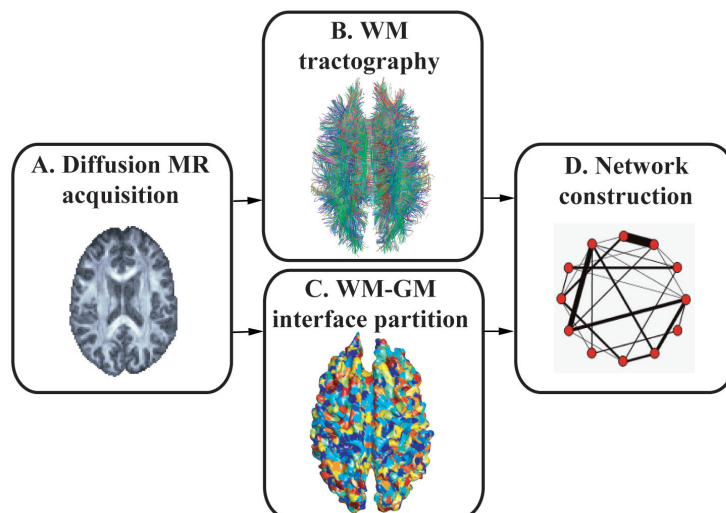
Figure 9.1: Overview of the whole process. (A) Acquisition of the diffusion MR images. (B) Tractography in the brain WM. (C) Partitioning of the WM-GM interface into small regions of interest (ROIs). (D) Creation of the network using the results of steps B and C.

methodology derived from diffusion MR tractography that allows us to map non-invasively and at a millimetric scale the structural white matter connectivity of the whole brain. The resulting network is composed of nodes representing small areas of the cortex, and weighted edges that capture long-distance connection densities between these areas. This approach provides us with a relatively high resolution; such networks consist of thousands of nodes, which is 1-2 orders of magnitude more than the networks currently available (thousands versus tens of nodes).

In this work, we analyze the basic brain graph properties of healthy subjects. In particular, we study a number of distributions derived for nodes (e.g., degree, strength) and edges (weight, length). We also answer some questions related to the topology, e.g., "Is the brain network a small world?". With technology improvements, finer resolution and a better Signal-to Noise Ratio (SNR), or a deeper analysis of the network, more complex and accurate network characteristics will be accessible, thus potentially contributing to the answers of some key questions in neuroscience.

9.2 Material and methods

The procedure from diffusion MRI to the graph mapping brain connectivity is similar to the four-step process described in Chapter 4: (A) diffusion MRI acquisition, (B) white matter (WM) tractography, (C) WM-GM interface partition into ROIs and (D) network construction (see Figure 9.1). However, there are several differences due to the particular nature of this work, especially on the WM-GM interface partition into ROIs. These differences as well as the various parameters used in this work are described in what follows.

MRI acquisition

After having obtained the informed consent of two healthy volunteers, two data sets were acquired with an Achieva 3T Philips scanner using a diffusion weighted single shot spin echo EPI sequence. The timing parameters of the pulse sequence were TR/TE/Δ/δ = 3000/154/47.6/35 ms, maximum diffusion gradient intensity was 80 mT/m, yielding a maximal b-value of 12000 s/mm^2. The matrix size was 128 x 128 and the slice number was 30. The field of view was 256 x 256 mm^2 and the slice thickness 3 mm, which yielded a voxel size of 2 x 2 x 3 mm^3. Q-space was sampled over the sphere using 515 different encoding gradients, and the data were reconstructed following a classical DSI scheme [226] (see Section 2.6), which produced a 3D diffusion probability density function (pdf) in every voxel. The data were further simplified by computing the orientation density function (ODF) in each voxel.

White matter tractography

We use the streamline tractography algorithm described in Section 4.3 to produce a set of approximately 3 million fibers, that we consider as an estimate of the real white matter axonal bundle trajectories. For the graph of about 1000 nodes they translate into about 50'000 edges. This is a very dense graph, of the average node degree of 100. Such dense graphs are sometimes difficult to analyze. For instance, the clustering coefficient c (the probability that two randomly chosen neighbors of a node are also direct neighbors of each other [224]) of a dense graph is naturally close to 1, which makes any analysis rather meaningless. Therefore, for some applications, we need a method to filter out some edges and keep only the relevant ones. We use two natural ways of limiting the number of edges in our graphs:

Random fibers   Although for every data set we generate around 3 million fibers, this is not any special number. We could as well take 100 thousand or 10 million fibers. As illustrated in Figure 9.2, this would strongly affect the number of resulting edges. Therefore, our first approach to limit the number of edges is to take a random subset of a given size out of our 3 million fibers. The study of the whole spectrum of fiber numbers gives us a better view than the study based on one, arbitrarily chosen number.

Top-weight edges   In the second method we consider the edges built based on all fibers, and delete only the edges with the smallest weights (according to some threshold). The heavy-tailed distribution of edge weights guarantees that we always retain most of the "edge mass" and reject only the edges with very small weights that are possibly the result of noise.

WM-GM interface partition into ROIs

Whereas in Chapter 4 the ROIs are built such that the location of each ROI is the same for each subject, here it is not required since we only want to analyze global properties of the networks. Moreover, we want to analyze the variability of our measurements over several scales from 500 ROIs to 4000 ROIs, creating regions by far smaller than the minimal size produced by the methodology described in Chapter 4. Therefore, we use a particular heuristic, as follows.
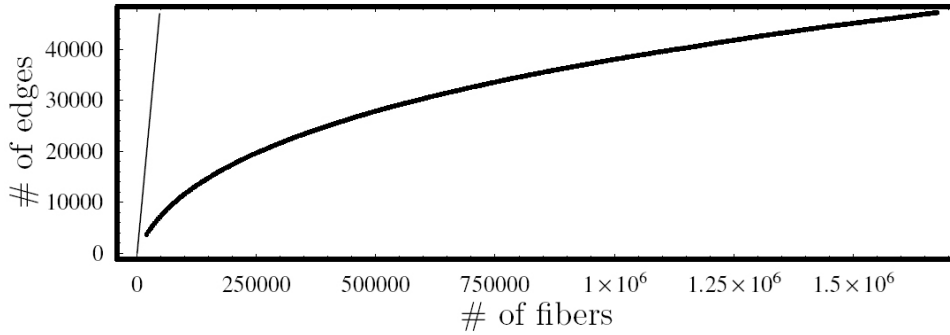
Figure 9.2: The number of edges in the resulting graph as a function of the number of randomly initiated fibers. The straight line represents the y=x relation.
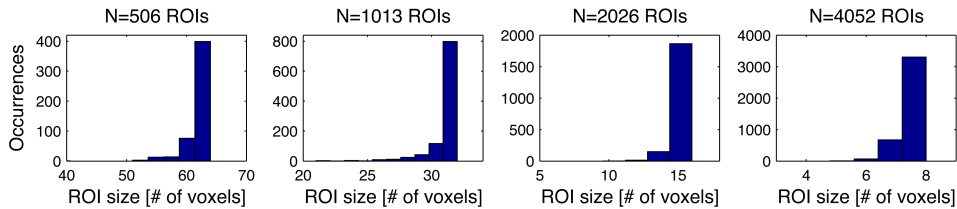
Figure 9.3: Histograms of ROI sizes for the number of ROIs ranging from N = 506 to 4052 in subject 1. One voxel translates to about 4 mm^2.

First, we identify the WM-GM interface based on a thresholding of the b0 image. Then, we choose a WM-GM interface voxel at random and iteratively connect it to the neighboring WM-GM interface voxels until it reaches the desired size; this structure becomes our first ROI. Similarly, we grow other ROIs, one by one, always starting near the ones that have already been created. We repeat this procedure until all the WM-GM interface is covered with ROIs. This gives us already quite a good partition, however, it can be easily further improved. Therefore, in the second phase of our heuristic we restart the ROI growth process. This time we grow all the ROIs simultaneously, starting from the centers of gravity of the ROIs found in the first phase. This results in a much better compactness of the ROIs with surface variations of less than 10%, as shown in Figure 9.3.

Network construction

Finally, the graph of brain connectivity is computed as follows. Every ROI becomes a node in the graph. An edge e is built if there exists at least one fiber f with end-points in the corresponding ROIs i and j. Its weight, representing the fiber density, is defined by Equation 4.1. Note that since the ROIs have similar size, we do not normalize the fiber density by the surface of the ROIs. We also define the edge length l_e as the average length of the fibers constituting the edge e.

The size of a ROI is a parameter in our methodology. On the one hand, a natural lower limit for this size is one voxel of the WM-GM interface. However, we prefer to take at least several of them to be sure to have a representative number of fibers connecting this ROI to the rest of the brain. On the other hand, taking too large ROIs results in

110

a network of trivially small size. In our simulations we set the ROI size between 8 and 64 voxels of WM-GM interface. It results in a weighted network of 500 to 4000 nodes representing small areas of WM-GM interface between 250 mm^2 (64 voxels/ROI) and 30 mm^2 (8 voxels/ROI), respectively. This graph has 25000 to 100000 edges that represent axonal bundles of millimetric or centimetric diameter. For simplicity, in this text we analyze graphs of about 1000 nodes. In particular, $|V1| = 1013$ nodes and $|E1| = 47217$ edges for subject 1, and $|V2| = 956$ and $|E2| = 50199$ for subject 2. The two graphs are built based on about $|F| = 3$ million fibers generated by the tractography algorithm. The results obtained for the other granularities, from $|V| = 500$ to 4000 nodes, are qualitatively similar (see [93] for more details).

9.3 Results and Discussion

Once the network constructed, several graph statistics characterizing the architecture of the network can be computed and examined.

Node statistics

We first turn our attention to the nodes of our graph. A basic characteristic of a node v is its degree, i.e., the number of edges incident on v. Many complex networks such as the World Wide Web, Internet, protein networks, ecological networks or cellular networks, have been shown to follow a heavy-tailed node degree distribution [3]. In other words, they have a very significant number of high degree nodes, called hubs. As such networks, also called *scale free* [3], are characterized by relatively short distances between any two nodes and by high robustness to random failures [4], they seem, at first sight, to be good candidates for brain topology. Surprisingly, we find in our data set that this is not the case. In Figure 9.4, we plot the node degree distribution (a), and a closely related node strength distribution (b). The strength s of a node v is the sum of weights of all edges incident on the node v [12]. Although these distributions cover more than two decades, they are roughly linear in the log-lin scale, which indicates their exponential tail. This is probably the first time that a claim about the node degree distribution of cortical structural connectivity mapped at high spatial resolution can be made. The networks available and studied to date [110, 197] are simply too small to judge if their node distribution is exponential, heavy tailed, or yet different. It is worth mentioning that in contrast to structural analyses, some functional brain networks have been described as scale-free [56].

Edge statistics

The edge length l distribution decays exponentially (Figure 9.5a), indicating that the number of long connections is small. The edge weight w distribution is much broader and close to heavy-tailed (Figure 9.5b). Therefore, there are a significant number of very strong connections that are predominantly short as demonstrated in Figure 9.5c. This observation is in agreement with the results of other complementary studies on the organization of the brain that suggest that brain favors, with some intriguing exceptions, locally dense communication and minimizes the number of long distance connections [41]. For instance, by examining many alternative arrangements of macaque pre-frontal cortex,
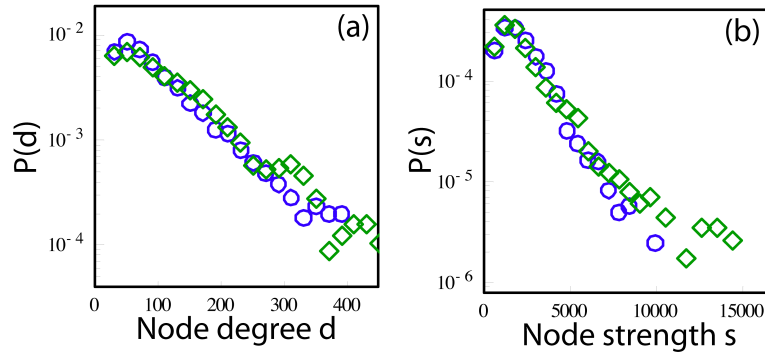
Figure 9.4: Basic characteristics of nodes in the graph of brain connectivity. $P(d)$ and $P(s)$ are the probability that a randomly chosen node has the degree, respectively the strength, equal to d, respectively s. The node degree distribution (a) and node strength distribution (b) are lin-binned and plotted in log-lin scale. Color code: subject 1 (blue circles), subject 2 (green diamonds).
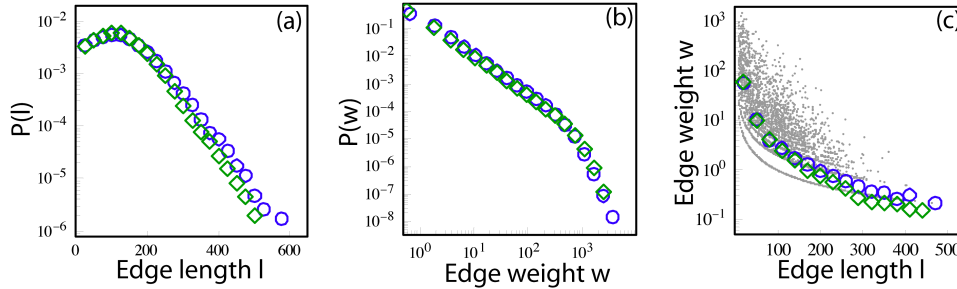
Figure 9.5: Basic characteristics of edges in the graph of brain connectivity. (a) The distribution of edge lengths l in log-lin scale, lin-binned. (b) The distribution of edge weights w in log-log scale, log-binned. (c) Scatter plot of w vs l. The symbols are lin-binned average values for subject 1 (blue circles) and subject 2 (green diamonds).

[127] showed that the layout of cortical areas minimizes the total lengths of the axons needed to join them. A similar observation was made by [44] about the intrinsic gray matter connectivity of mice where the volume fraction of axons and dendrites seems close to optimal. The work of [234] indicate that there is an evolutionary conserved scaling of the volume of the white matter as the 4/3 power of the volume of the gray matter, which can be explained by the fact that global geometry of the cortex minimizes the average length of the long-distance fibers while keeping the average connection density of long-distance connection fibers constant. However recent reports suggest that the organization of neural networks is not only shaped by the minimization of total wiring length. Multiple constraints seem to be involved, not only wiring length but also the average number of processing steps (related to the average distance between node) [121].

Network Topology

Having examined separately the distributions of nodes and edges, we now discuss the topology of the graph itself. An interesting question one can ask is: "Is the brain a small

world?". The more formal definition of a small-world graph involves two metrics, the clustering coefficient c and the average shortest path length $\langle sp \rangle$. We follow [224], who define the clustering coefficient c as the probability that two randomly chosen neighbors of a node are also direct neighbors of each other, i.e., $c = \frac{1}{|V|} \sum_{v \in V} c_v$, where c_v is the number of edges interconnecting the neighbors of the node v divided by the number of all possible edges. The average shortest path length $\langle sp \rangle$ is the average distance between any two nodes in graph. If the graph is disconnected, only the largest connected component is considered. A graph is called a small world if it has (i) a clustering coefficient much greater than that of equivalent random graphs and (ii) the average shortest path length $\langle sp \rangle$ is comparable with that of a random graph with the same number of nodes and edges [224].

There are two issues that we have to address before we attempt to decide if our graph G of brain connectivity is a small world. First, G is weighted. As there exists no standard way of generalizing the clustering coefficient to weighted graphs (see e.g. [122, 178]) and it is not obvious how to interpret edge weights when computing the average shortest path length, we have decided to treat every edge equally and apply the classic non-weighted approach [224]. Second, the number of fibers that are initiated during tractography determines the density of graph G. In order to explore the effect of connection density on our results, we exclude some of the edges by applying the two filtering techniques described above.

We present the results in Figure 9.6. As a reference we take a random graph not only with the same number of nodes and edges (as proposed in [224]), but also with the same degree distribution as the brain graph. This graph is generated with the rewiring technique described in [147]. Preserving the degree distribution allows us to rule out this factor from the set of possible reasons of observed differences between the brain and the reference topology. For any number $|E'|$ of edges remaining after the filtering, the graph of brain connectivity has a much higher clustering coefficient than the corresponding random graph; this is especially well pronounced for the "Top-weight edges" graph. At the same time their average shortest path lengths $\langle sp \rangle$ are comparable. Hence our measurements suggest that the small-world model fits the brain network. Indeed, the small-world topology seems well suited for the neuronal network of the brain when thinking in evolutionary and developmental terms. This is because it is a good compromise between full connectivity, which would be very costly in terms of wiring (i.e., brain volume) and power supply [11], and a lattice topology that impairs massively long distance communication. Furthermore, the combination of high local clustering and small average shortest path length with efficient neural coding [191] allows for a distributed computing where only a small fraction of local intense computation needs to be transmitted to distant regions, which may be sufficient for synchronous brain activity [80]. The small-worldness of the brain network was already advocated before, based on relatively small networks (50-70 nodes) resulting from post-mortem tracing studies in rat, macaque monkey and cat brain regions [105, 106, 197]. In contrast, the approach presented in this article provides, for the first time, evidence for the presence of small-world topology in the structural connectivity of the human cerebral cortex. Moreover, the one to two orders of magnitude higher resolution resulting from our method (thousands vs. tens of nodes) increases the confidence we have in the derived statistics.
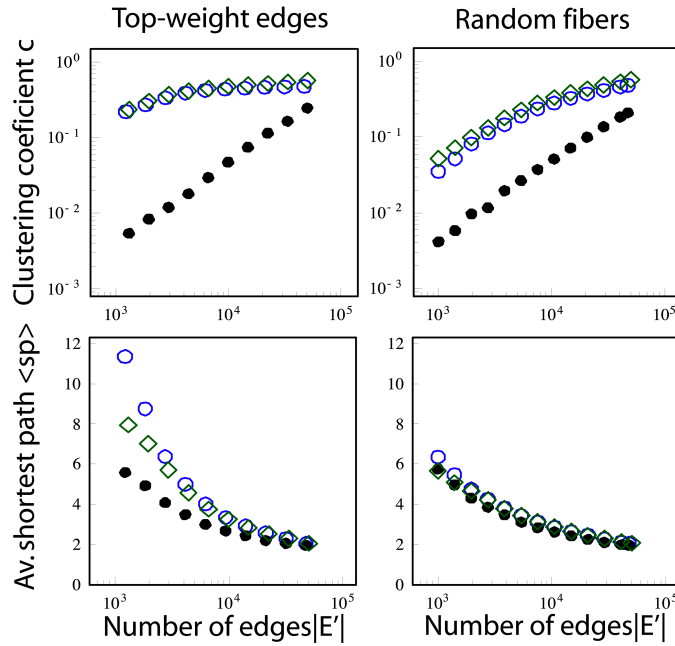
Figure 9.6: Average shortest path $\langle sp \rangle$ and clustering coefficient c as a function of the number of edges in the brain graph $|E'|$. The edges are chosen from the set of all edges E either giving the priority to the edges with high weights ("Top-weight edges", left column), or based on a random subset of fibers ("Random fibers", right column). As a reference we take a random graph with the same number of nodes and edges, and the same degree distribution. Color code: subject 1 (blue circles), subject 2 (green diamonds), random graph reference (black filled circles). The results are averaged over 10 realizations of the "random fibers" filtering and random graphs; the confidence intervals (not shown) are comparable with the symbol size.

Intra- and inter-individual network differences

In order to test the robustness of our methodology and because of uncertainty about the ideal number of nodes for the presented methodology, we measured the brain network at 4 different node resolutions on data set 1. We notice that for scales varying between 500 and 4000 nodes and 25'000 and 100'000 edges respectively, the global network topology is preserved. This is a range of scales that matches the sensitivity of the method, as we do not expect to be able to accurately map tracts smaller than several millimeters in diameter, which is presently the size of our ROIs. Pushing the network "resolution" higher by increasing the number of nodes and reducing the surface area of the ROIs would increase the quantification noise (limiting the number of fibers per ROI), which ultimately would destroy the information contained in the network model. On the other hand, increasing the ROI size limits the precision of the mapping, potentially grouping together pieces of gray matter that are functionally different. At the scale we use in this study, we expect that the chance that ROI overlaps several critically different cortices is not higher than the inaccuracy related to the matching of template atlas on our data. Notwithstanding the advantage with a fine grain method to always be able to group arbitrarily sets of nodes in order to study connectivity patterns between for example well known functional

	Data set 1	Data set 2
Number of nodes	1013	956
Number of fibers	1'677'892	1'833'794
ROIs area	1.28cm^2	1.43cm^2
Number of edges	47'217	50'199

Table 9.1: Network construction parameters for data sets 1 and 2.

or anatomical areas like Brodmann's.

While basic connectivity parameters differ slightly for data sets 1 and 2 (see Table 9.1), the global properties are quite similar. The differences that we observe in Figures 9.4, 9.5, 9.6 may or may not reflect the individual properties of the subjects. Clearly, more experiments and studies are needed to be able to address the issue of between-subject variability with a high level of confidence.

Although our methodology yields promising results, we need to keep in mind that there are some steps prone to various kinds of noise and distortions whose effect is difficult to evaluate, as shown previously in this thesis. First of all, we work at a given level of granularity. The spatial and angular resolution of our diffusion MRI experiment is limited, which makes it difficult to tell much about sub-millimetric fiber tracts and crossing axonal bundles separated with angles smaller than 20°. The ROIs have a given size, which automatically groups tens of thousands of neurons into a single node. Noise is also introduced during the MRI acquisition, and the tractography algorithm might not perfectly model the relationship between water diffusion and axonal orientation. Although all these points are constantly being improved, there will always remain a huge discrepancy between our constructed graph and the real neuronal network made of 10^{10} neurons and several orders more connections.

9.4 Conclusion

In this work, we have mapped networks of structural connectivity in the brain, allowing to globally characterize brain connectivity with individual tract properties or network statistics in an individual living subject. Based on the analysis of two healthy subjects we have found that the graph of the human brain is a small-world, but not a scale-free network. Large new areas of application are foreseen; in basic neuroscience our technique may contribute to the discovery of the general principles regulating communication, evolution and development of the brain; in clinical neuroscience it may shed new light into diseases of disorders that involve disruptions of anatomical brain connectivity.

A better understanding of the link between functional networks and structural connectivity is of the highest importance in neuroscience. In Chapter 7 we have demonstrated the relationship between structural connectivity measured with diffusion MR tractography and functional connectivity measured with resting-state functional MRI. In the next chapter, we propose another approach to link structure with function. Based on several network measures, we identify cortex areas that form a densely interconnected and topologically central core. Those regions are compared to a major feature of cortical functional connectivity: the default network [65–68, 82, 172, 190].

Mapping the Structural Core of the Human Cerebral Cortex

10

10.1 Introduction

The human cerebral cortex consists of approximately 10^{10} neurons that are organized into a complex network of local circuits and long-range fiber pathways. This complex network forms the structural substrate for distributed interactions among specialized brain systems [72, 164, 196]. Computational network analysis [194] has provided insight into the organization of large-scale cortical connectivity in several species, including rat, cat, and macaque monkey [34, 59, 180, 194]. In human cortex, the topology of functional connectivity patterns has recently been investigated [1, 2, 17, 199], and key attributes of these patterns have been characterized across different conditions of rest or cognitive load. A major feature of cortical functional connectivity is the default network [65–68, 82, 172, 190], a set of dynamically coupled brain regions that are found to be more highly activated at rest than during the performance of cognitively demanding tasks. Spontaneous functional connectivity resembling that of the human default network was reported in the anaesthetized macaque monkey, and functional connectivity patterns in the oculomotor system were found to correspond to known structural connectivity [222]. Computational modelling of spontaneous neural activity in large-scale cortical networks of the macaque monkey has indicated that anti-correlated activity of regional clusters may reflect structural modules present within the network [108]. These studies suggest that, within cerebral cortex, structural modules shape large-scale functional connectivity.

Understanding the structural basis of functional connectivity patterns requires a comprehensive map of structural connection patterns of the human brain (the human con-

nectome [196]). As we have shown previously, recent advances in diffusion imaging and tractography methods permit the noninvasive mapping of white matter cortico-cortical projections at high spatial resolution [26, 50, 96, 182, 225], yielding a connection matrix of inter-regional cortical connectivity (see Chapter 4). In the previous chapter, we have demonstrated small-world attributes and exponential degree distributions within such structural human brain networks. In the present study, we apply network analysis techniques on the high-resolution cortical connection matrices to identify structural modules. Several techniques reveal the existence of a set of posterior medial and parietal cortical regions that form a densely interconnected and topologically central core. The structural core contains numerous connector hubs, and these areas link the core with modules in temporal and frontal cortex. We finally discuss anatomical imaging data, suggesting an important role for the core in cerebral information integration.

10.2 Material and Methods

Diffusion imaging and tractography

The data used for this study are the same as those already described in Chapter 7, and the post-processing is rigorously identical to what is described in Chapter 4 and illustrated in Figure 4.3. This provides us with a weighted network of 998 ROIs of surface area approximately 1.5 cm^2, covering the entire cortex and grouped into 66 anatomical subregions. Remember that the anatomical positions of the ROIs are in register across participants, allowing for averaging across individual networks.

Network analysis

Connectivity backbone   To visualize network layout and clusters, we derive the network's connectivity backbone [104]. First, a maximum spanning tree, which connects all nodes of the network such that the sum of its weights is maximal, is extracted. Additional edges are added in order of their weight until the average node degree is 4. The resulting network constitutes the connectivity backbone of the connection matrix.

k-Core decomposition   This decomposition method [7] involves the recursive pruning of the nodes with degree less than k. Applied to large networks the method yields cores of vertices that are mutually linked by at least k connections. We derive all k-cores for high-resolution connection matrices, whose top 10'000 fiber densities are converted to ones. We implement a related method, which we call s-core decomposition, that recursively prunes weakest nodes up to a strength s. The remaining core contains only nodes with strengths of at least s. For a series of discrete degrees k_i or strengths s_i we can then derive the corresponding k_i-th and s_i-th cores. Any of the 66 anatomical subregions is considered part of the k_i-th or s_i-th core if at least half of its ROIs are present in that core.

Modularity detection   We apply a variant of a spectral community detection algorithm [154] to identify modules (communities) within each network. As inputs to the algorithm we use symmetric connectivity matrices corresponding to individual (998 ROI) or aggregated (66 anatomical region) fiber densities. The algorithm generates a modularity matrix with an associated modularity score. For regional connection matrices (n =

66), we obtain 10'000 solutions which are ranked according to their modularity and we select the optimal solution for a range of 212 modules. For high-resolution matrices we obtain 20'000 solutions for modularity ranging from 38 modules.

Hub classification Cluster assignment from the optimal modularity matrices provides the basis for the classification of network hubs into two groups [86]. We calculate each node's participation index P, which expresses its distribution of intra- versus extra-modular connections. P of node i is defined as

$$P_i = 1 - \sum_{1}^{N_M} (\frac{\kappa_{is}}{k_i})^2,$$
(10.1)

where N_M is the number of identified modules, k_i is the degree of node i, and κ_{is} is the number of edges from the ith node to nodes within module s. We classify nodes with above average degree and a participation coefficient $P < 0.3$ as provincial hubs, and nodes with $P \geq 0.3$ as connector hubs.

Graph theory methods With the sole exception of k-core decomposition and node degree, all graph theoretical analyses in this study are carried out for weighted networks. Node degrees are calculated as the column sums of the binarized connection matrix (i.e., the number of all edges for each node, regardless of weight). Node strengths are calculated as the column sum of the non-binarized connection matrix (i.e., the sum of all edge weights for each node).

Centrality of a node expresses its structural or functional importance. Highly central nodes may serve as waystations for network traffic or as centers of information integration. The betweenness centrality of a node is defined as the fraction of shortest paths between any pair of vertices that travel through the node [218]. The betweenness centrality of a node i is given as

$$C_i^B = \frac{1}{N(N-1)} \sum_{s \neq i \neq t}^{N_M} \frac{\rho_{st}(i)}{\rho_{st}},$$
(10.2)

where $\rho_{st}(i)$ is the total number of shortest paths between a source node s and a target node t that pass through i, ρ_{st} is the total number of all shortest paths linking s to t, and N is the number of nodes.

Efficiency of a node is defined as the arithmetic mean of the inverses of the path lengths between the node and all other nodes in the network [1, 134], i.e.,

$$E_i = \frac{1}{N-1} \sum_{i \neq j} \frac{1}{d_{ij}}.$$
(10.3)

10.3 Results

Data sets and network measures

Network analyses are carried out for high-resolution connection matrices (n = 998 ROIs with an average size of 1.5 cm^2), as well as for regional connection matrices (n = 66

BSTS	bank of the superior temporal sulcus
CAC	caudal anterior cingulate cortex
CMF	caudal middle frontal cortex
CUN	cuneus
ENT	entorhinal cortex
FP	frontal pole
FUS	fusiform gyrus
IP	inferior parietal cortex
IT	inferior temporal cortex
ISTC	isthmus of the cingulate cortex
LOCC	lateral occipital cortex
LOF	lateral orbitofrontal cortex
LING	lingual gyrus
MOF	medial orbitofrontal cortex
MT	middle temporal cortex
PARC	paracentral lobule
PARH	parahippocampal cortex
POPE	pars opercularis
PORB	pars orbitalis
PTRI	pars triangularis
PCAL	pericalcarine cortex
PSTS	postcentral gyrus
PC	posterior cingulate cortex
PREC	precentral gyrus
PCUN	precuneus
RAC	rostral anterior cingulate cortex
RMF	rostral middle frontal cortex
SF	superior frontal cortex
SP	superior parietal cortex
ST	superior temporal cortex
SMAR	supramarginal gyrus
TP	temporal pole
TT	transverse temporal cortex

Table 10.1: List of the subregion designators.

anatomical subregions). Table 10.1 shows a list of the subregion designators used throughout this work. All networks cover the entire cortices of both hemispheres but exclude subcortical nodes and connections. When not indicated otherwise, the data shown in this paper are based on the analysis of individual high-resolution connection matrices, followed by averaging across the five participants.

Network measures include degree, strength, betweenness centrality, and efficiency (see Material and Methods). Briefly, degree and strength of a given node measure the extent to which the node is connected to the rest of the network, while centrality and efficiency capture how many short paths between other parts of the network pass through the node. A node with high degree makes many connections (where each connection is counted

once), while a node with high strength makes strong connections (where strength is equal to the sum of connection density or weight). A node with high betweenness centrality lies on many of the shortest paths that link other nodes in the network to one another. A node with high efficiency is itself found to be, on average, at a short distance from other nodes in the network.

Degree and strength distribution

We find binary, high-resolution brain networks to be sparsely connected, with connection densities varying between 2.8% and 3.0%. Between 9% and 14% of all binary connections are interhemispheric. 54% of the total edge mass (the sum of all fiber densities) is accounted for by connections linking ROIs belonging to the same anatomical subregion, 42% is made between ROIs belonging to different anatomical subregions located in the same cortical hemisphere, and 4% is interhemispheric (homotopic or heterotopic). Confirming earlier reports [225], we find that cumulative distributions of node degree and node strength are exponential rather than scale-free (see also Section 9.3). While not scale-free, node degrees and node strengths for single ROIs can vary over a significant range (approximately 10-fold), indicating that fiber densities are not uniformly distributed across the cortical surface. Figure 10.1A and 10.1B shows the distribution of average node degree and node strength rank-ordered by anatomical subregion. A large number of ROIs with high degree and high strength are localized within subregions of medial cortex (e.g., cuneus and precuneus, posterior and anterior cingulate cortex) and temporal cortex (e.g., bank of the superior temporal sulcus). A plot of the distribution of node strengths on the cortical surface across all participants (Figure 10.1C) shows consistently high values in posterior medial cortex, in medial frontal cortex, and in superior temporal cortex.

ROIs with high degree or strength may connect randomly or they may connect preferentially to one another. We examine high-resolution connection patterns from individual subjects for degree and strength correlations by computing the network's assortativity [153]. We find that networks of all five subjects exhibit positive assortativity (0.1941 $\pm$ 0.0513 for degrees; 0.2161 $\pm$ 0.0275 for strengths) indicating a tendency for nodes with matching degree or strength to be directly connected. As expected, degree-matched randomized control networks show assortativity narrowly distributed around zero (e.g. -0.0122 $\pm$ 0.0098 for degrees). Positive assortativity is consistent with the existence of a densely interconnected and coherent structural core of brain regions.

Network visualizations

A representative example of a high-resolution structural connection matrix of an individual human brain is shown in Figure 10.2A. Entries of the matrix represent fiber densities between pairs of single ROIs. The matrix shown in the example displays a total of 14'865 symmetric connections (connection density 3.0%). To visualize structural patterns within this connection matrix, we extract the connectivity backbone ([104], see Material and Methods), which is displayed in Figure 10.2B with a layout derived from the Kamada-Kawai force-spring algorithm [123] implemented in Pajek [18]. The algorithm generates a spatial arrangement of ROIs along clearly defined anterior-posterior and medial-lateral axes and reveals clusters of dense connectivity within posterior, temporal, and frontal cortex. Figure 10.2C shows the connectivity backbone plotted in anatomical coordinates. The dorsal view shows groupings of highly interconnected clusters of ROIs arranged along
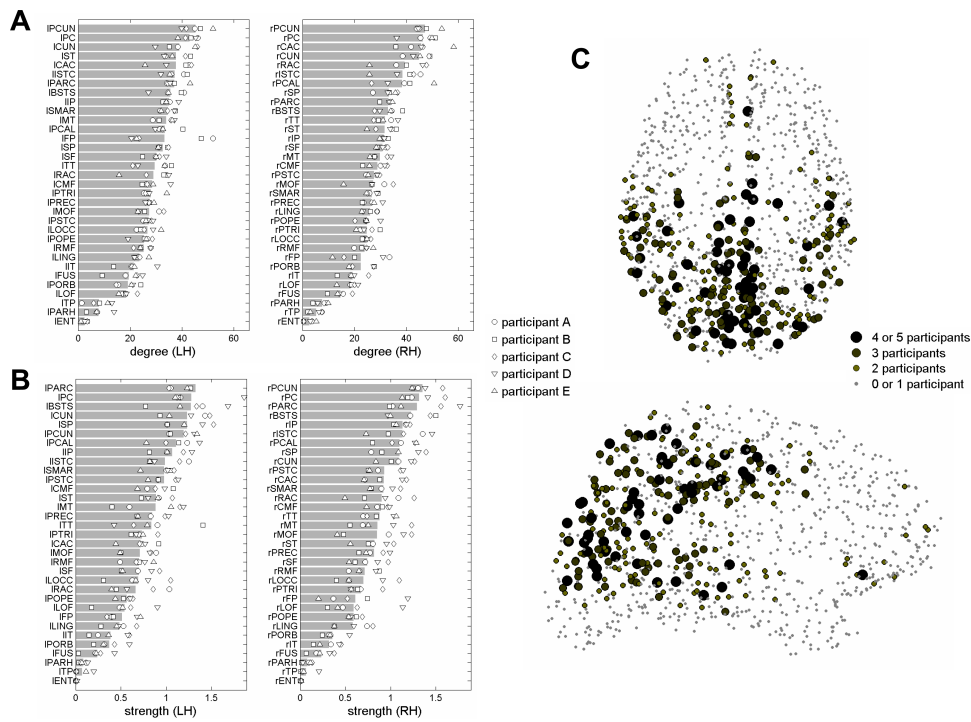
Figure 10.1: (A) Ranked distribution of node degree for left and right cerebral hemispheres. Shaded bars represent means across five participants and symbols indicate data for individual participants. (B) Ranked distribution of node strength for left and right cerebral hemispheres. (C) ROI strength obtained from high-resolution connection matrices. The plot shows how consistently ROI strength ranked in the top 20% across participants.

the medial cortical surface, extending from the precuneus via posterior and anterior cingulate cortex to the medial orbitofrontal cortex. Dorsal and lateral views additionally show clusters of temporal and frontal ROIs in both hemispheres.

Major structural patterns become more evident when considering the average regional connection matrix (Figure 10.3A). The matrix is constructed by calculating mean fiber densities over individual pairs of ROIs comprising each subregion, followed by the averaging of densities over all five participants. Figure 10.3B displays the connectivity backbone constructed from the average regional connection matrix, revealing groupings of anatomical regions largely corresponding to those shown for the high-resolution backbone in Figure 10.2B. A dominant feature of the regional connection matrix is a single, callosally interconnected cluster of regions extending from the cuneus and precuneus via cingulate cortex to medial frontal cortex. In addition, each hemisphere contains a single, relatively distinct cluster of temporal cortical regions, as well as a less-densely interconnected frontal cluster comprising periorbital cortex, pars opercularis, pars triangularis, and other regions.
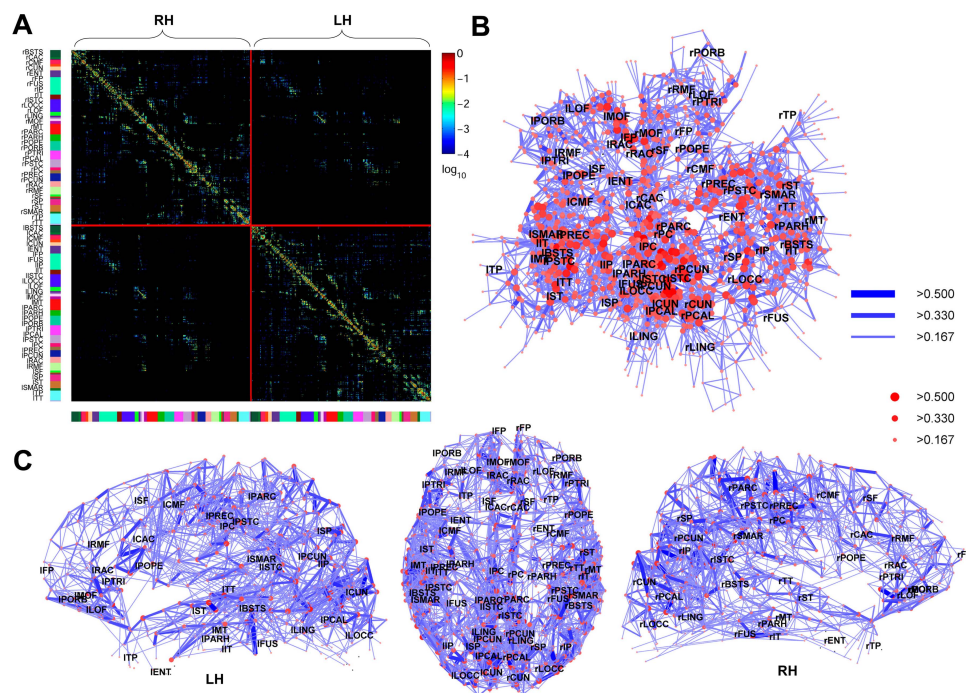
Figure 10.2: (A) Matrix of fiber densities (connection weights) between all pairs of n = 998 ROIs. ROIs are plotted by cerebral hemispheres, with right-hemispheric ROIs in the upper left quadrant, left-hemispheric ROIs in the lower right quadrant, and interhemispheric connections in the upper right and lower left quadrants. All connections are symmetric and displayed with a logarithmic color map. (B) Kamada-Kawai force-spring layout of the connectivity backbone. Labels indicating anatomical subregions are placed at their respective centers of mass. Nodes (individual ROIs) are coded according to strength and edges are coded according to connection weight (see legend). (C) Dorsal and lateral views of the connectivity backbone. Node and edge coding as in (B).

k-Core decomposition, modularity, and hubs

While network visualization provides strong hints of connectional relationships, objective methods are needed to map structural cores, to delineate network modules, and to identify hub regions that link distinct clusters. We quantify these phenomena using k-core decomposition [7], spectral community detection [154], and nodal participation indices [86], respectively.

Intuitively, a network core is a set of nodes that are highly and mutually interconnected. For a binary network, the k-core is the largest subgraph comprising nodes of degree at least k, and is derived by recursively peeling off nodes with degree lower than k until none remain [7]. Each node is then assigned a core number, which is defined as the largest k such that the node is still contained in the k-core. We perform k-core decomposition on binary, high-resolution connection matrices from all five participants and derive the core number for each ROI, as well as the average core number for each anatomical subregion (Figure 10.4). A large core number indicates that an ROI or region is resistant to this erosive procedure and participates in high-k structural cores of the network. In all participants, full erosion occurs at a core number of 20. The most consistent members of

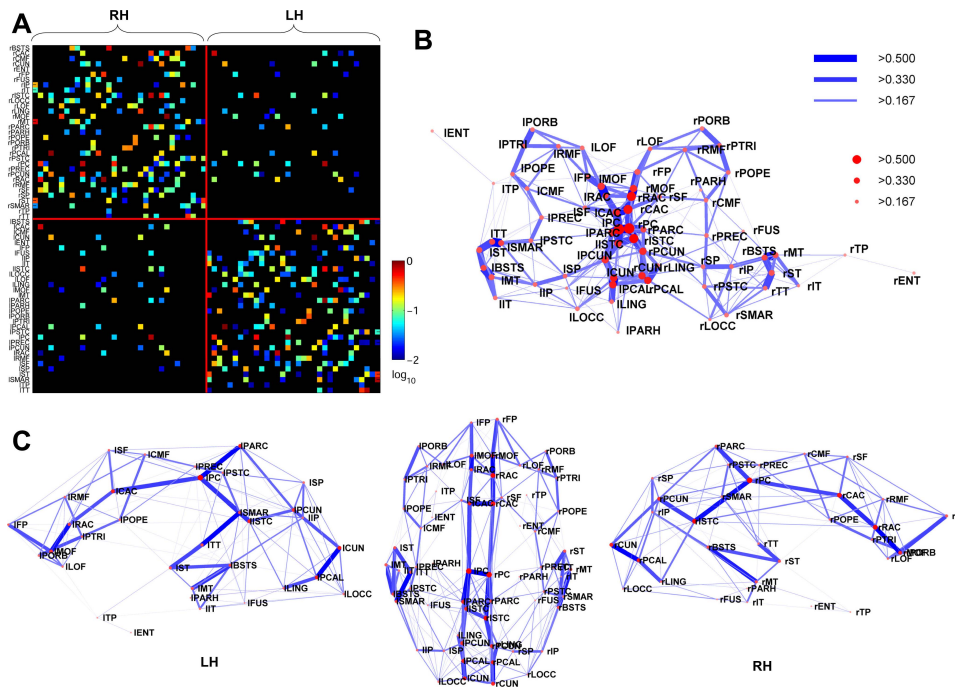Figure 10.3: (A) Matrix of inter-regional fiber densities between pairs of anatomical subregions, obtained by averaging over fiber densities for all pairs of ROIs within the regions, and averaging across all five participants. Connection weights are symmetric and are plotted on a logarithmic scale. (B) Network layout. (C) Dorsal and medial views of the connectivity backbone in anatomical coordinates.

the highest degree k-core for each network (Figure 10.4A and 10.4B) are the precuneus, the posterior cingulate, the isthmus of the cingulate, and the paracentral lobule in both hemispheres. In all participants, the structural core is located within posterior medial cortex, and often extends laterally into parietal and temporal cortices, especially in the left hemisphere. A rank-ordered distribution of average core numbers per anatomical subregion (Figure 10.4C) identifies the posterior cingulate cortex, the isthmus of the cingulate cortex, the precuneus, the cuneus, and the paracentral lobule as regions with a high core number. Several temporal and parietal structures, including the superior and inferior parietal cortex, the bank of the superior temporal gyrus, and transverse temporal cortex all have high core rankings as well. k-Core decomposition, as applied in this work, largely discards edge weights. To test if the inclusion of edge weight information would alter our conclusions, we design a procedure that operates on the weighted fiber density matrix and erodes vertices according to their strength (s-core decomposition). s-Core decomposition (Figure 10.5) identifies the posterior cingulate cortex, the precuneus, the cuneus, the paracentral lobule, as well as the superior and inferior parietal cortex, all in both hemispheres, as members of the structural core.

We use spectral graph partitioning [154] to identify modules within the weighted high-resolution (n = 998) network as well as within the weighted average regional (n = 66) network. The spectral algorithm provides a means of grouping regions in a way that optimally matches the intrinsic modularity of the network. Optimal modularity for the average regional connectivity matrix is achieved with six clusters (Figure 10.6A). Four
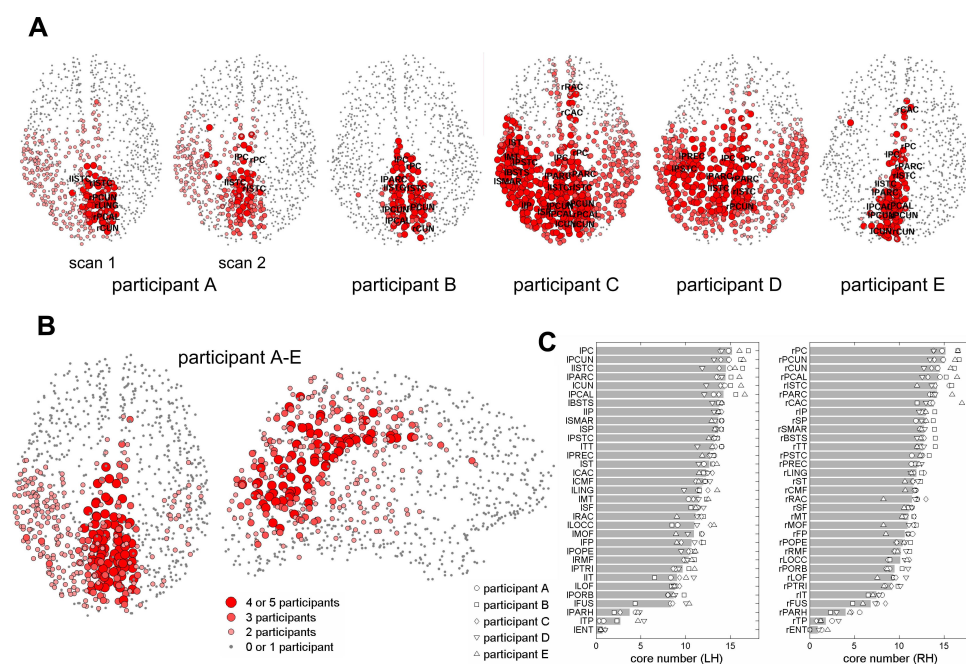
Figure 10.4: (A) Network cores for each individual participant derived by k-core decomposition of a binary connection matrix obtained by thresholding the high-resolution fiber densities such that a total of 10,000 connections remain in each participant. Nodes are plotted according to their core number, counted backwards from the last remaining core. (B) Average network core across all five participants. (C) Ranked distribution of core numbers for left and right cerebral hemispheres. Shaded bars represent means across five participants and symbols indicate data for individual participants.

contralaterally matched modules are localized to frontal and temporo-parietal areas of a single hemisphere. The two remaining modules comprise regions of bilateral medial cortex, one centered on the posterior cingulate cortex and another centered on the precuneus and pericalcarine cortex. Recovering the modularity structure using high-resolution connection matrices produces similar results (data not shown).

Knowledge of the distribution of connections within and between modules enables us to identify provincial hubs (hub regions that are highly connected within one module) and connector hubs (hub regions that link multiple modules) [86]. Without exception, connector hubs are located within the anterior-posterior medial axis of the cortex (Figure 10.6A), including bilaterally the rostral and caudal anterior cingulate, the paracentral lobule, and the precuneus. Examination of high-resolution connection matrices shows that the majority of connector hub ROIs is consistently found in posterior medial and parietal cortex (Figure 10.6B). Provincial hubs are members of the frontal (e.g., medioorbitofrontal cortex), temporoparietal (e.g., bank of the superior temporal sulcus, superior temporal cortex) or occipital modules (e.g., pericalcarine cortex). Most core regions, as identified by k-core or s-core decomposition, are members of the two medial modules. When combined into a single core module, over 70% of the between-module edge mass is attached to the core.

When modularity detection is applied to more restricted portions of the high-resolution
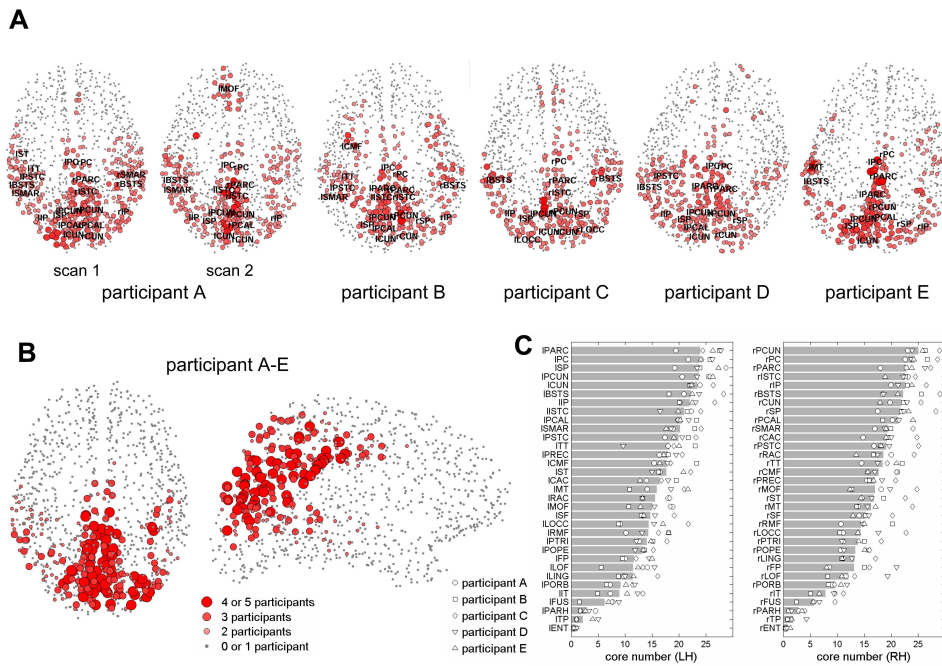
Figure 10.5: s-Core decomposition is carried out as described in Section Material and Methods. Individual s-core plots are shown for all five participants (A), as well as a plot showing the average s-core across all five participants (B). (C) A rank-ordered distribution of s-core numbers for all 66 anatomical subregions is shown.

connection data sets, for example the visual and frontal cortex, we are able to recover clusters that are consistent with those found in previous studies based on classical anatomical techniques, or orderings that were suggested based on functional subdivisions. For example, we find, in all five participants, a segregated dorsal and ventral cluster of visual ROIs, corresponding in location and extent to the dorsal and ventral stream of visual cortex [218]. Clustering of frontal cortical ROIs yields distinct clusters centered on orbital, medial, and lateral frontal cortex (Figure 10.7).

Centrality and efficiency

Regions with elevated betweenness centrality are positioned on a high proportion of short paths within the network [70]. The spatial distribution of ROIs with high betweenness centrality (Figure 10.8A and 10.8B) shows high centrality for regions of medial cortex such as the precuneus and posterior cingulate cortex, as well as for portions of medial orbitofrontal cortex, inferior and superior parietal cortex, as well as portions of frontal cortex. Figure 10.8B provides lateral views of the distribution of centrality across the two cerebral hemispheres showing that ROIs with high centrality are widely distributed. For example, ROIs with high centrality are found in the superior and middle frontal gyrus, in the inferior and superior parietal cortex, in addition to in regions of cingulate and medial posterior cortex. Averaged over all ROIs belonging to the same anatomical subdivision and over all participants (Figure 10.8C), centrality appears highest in the right and left posterior cingulate cortex, as well as other subdivisions of cingulate cortex,
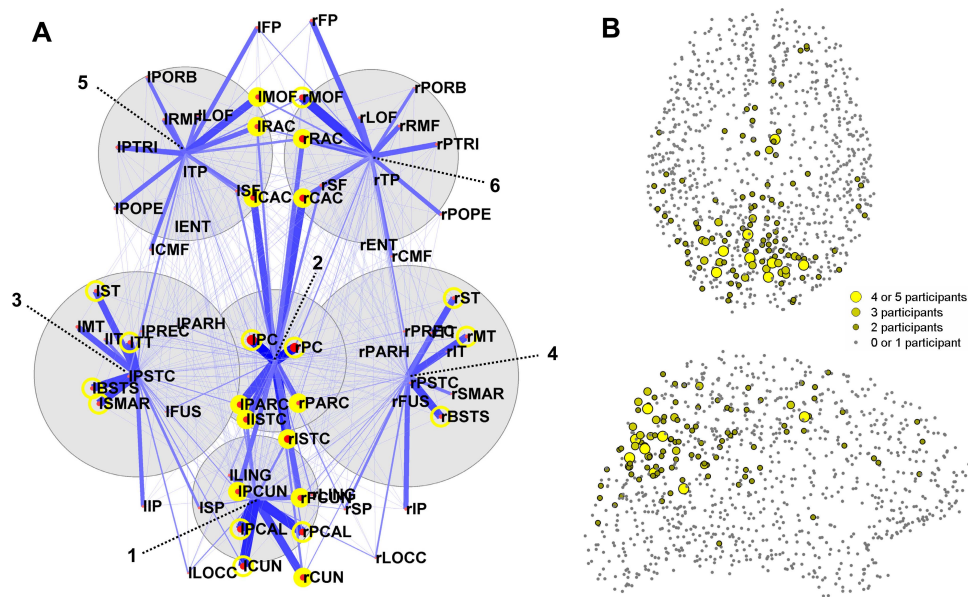
Figure 10.6: The modularity is derived from the average regional connection matrix. (A) The plot shows a dorsal view, with nodes representing anatomical subregions. The spatial position of each region corresponds to the center of mass coordinates calculated from participant A, scan 2 (as seen in Figure 10.3C). Six modules are shown as gray circles centered on their center of mass and sized according to their number of members. Edges correspond to the average connection densities of each region with the member regions of each of the six modules, plotted between that region's spatial coordinates and the center of mass of each module Connector hubs are defined as regions with above average strength and a participation index $P \geq 0.3$, indicating a high proportion of cross-module connectivity. These regions are marked as filled yellow circles. Provincial hubs have above-average strength and $P < 0.3$; they are marked as unfilled yellow circles. (B) Connector hubs obtained from analyses of high-resolution connection matrices. ROIs are displayed according to how consistently a given ROI is identified as a connector hub across participants.

and the precuneus and cuneus. Efficiency is related to closeness centrality, in that regions with high efficiency maintain short average path lengths with other regions in the network. We find that the posterior cingulate cortex, the precuneus, and the paracentral lobule are most highly ranked in both cerebral hemispheres (Figure 10.8D).
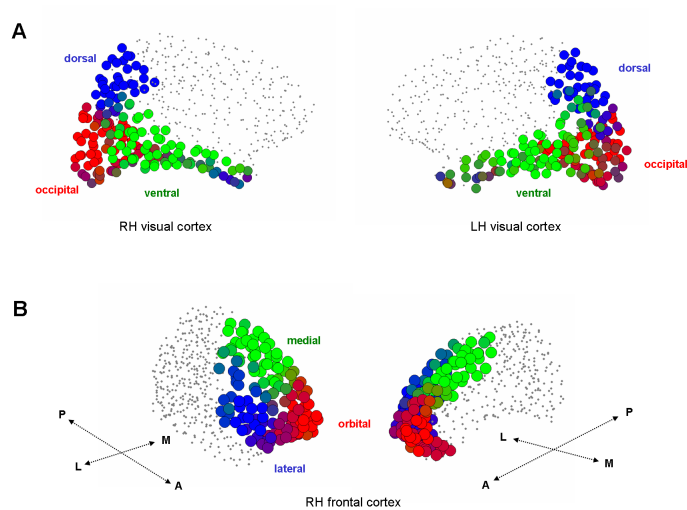
Figure 10.7: Cluster analysis of visual and frontal cortex. (A) After selection of visual ROIs and their interconnections, we search for optimal modularity using the spectral community detection algorithm described in [154]. The plot shows an overlay of the cluster arrangement found for each of the five participants. Red, green, and blue dots indicate the anatomical positions of ROIs grouped into three distinct clusters, roughly corresponding to occipital, ventral, and dorsal visual system, respectively. Pure colors indicate that the ROI is grouped consistently (for all five participants) into the corresponding cluster; intermediate clusters indicate groupings that are inconsistent across participants. (B) Clusters obtained after modularity analysis restricted to frontal ROIs and their interconnections, roughly corresponding to medial, lateral, and orbital frontal cortex.
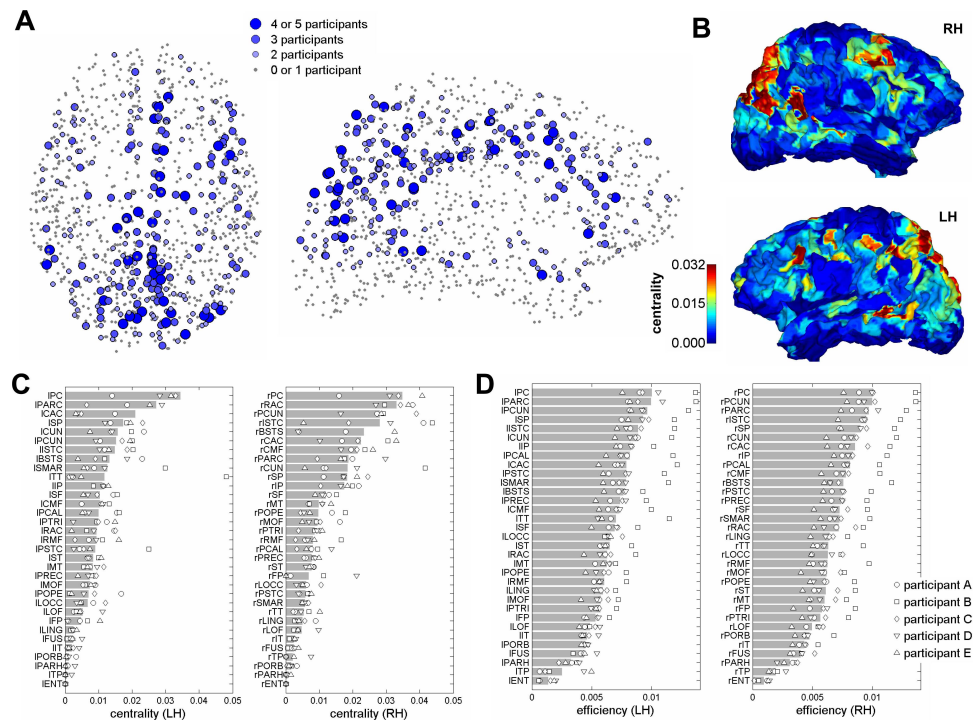
Figure 10.8: (A) ROI centrality obtained from analyses of high-resolution connection matrices. The plot shows how consistently ROI centrality ranked in the top 20% across participants. (B) Lateral views of the right and left cerebral hemispheres showing ROI centrality, averaged across all five participants and projected onto the cortical surface of participant A. (C) Ranked distribution of betweenness centrality for left and right cerebral hemispheres. Shaded bars represent means across five participants and symbols indicate data for individual participants. (D) Ranked distribution of efficiency for left and right cerebral hemispheres.

10.4   Discussion

Cortical connectivity plays a crucial role in shaping spontaneous and evoked neural dynamics. We map structural cortico-cortical pathways in the human cerebral cortex at high spatial resolution and find evidence for the existence of a structural core composed of posterior medial and parietal cortical regions that are densely interconnected and topologically central.

We characterize the structural core by mapping network indices, such as node degree, strength, and centrality, and by applying several network analysis methods: extracting a structural backbone, performing core decomposition, retrieving network modules, and classifying hub nodes. While several of these measures are known to be interrelated, each provides a different viewpoint from which to discern major features of the large-scale architecture. Based on their aggregated ranking scores across six network measures, we can identify eight anatomical subregions as members of the structural core. These are the posterior cingulate cortex, the precuneus, the cuneus, the paracentral lobule, the isthmus of the cingulate, the banks of the superior temporal sulcus, and the inferior and superior parietal cortex, all of them in both hemispheres. These regions are chosen because they exhibit elevated fiber counts and densities (node degree and strength), they are most resistant to the erosive procedures of k-core and s-core decomposition and they have high topological centrality. The high degree of interhemispheric coupling within the core further suggests that it acts as a single integrated system from which processes in both cortical hemispheres are coordinated.

The central structural embedding of posterior medial cortex in the human brain is consistent with a series of physiological findings including high levels of energy consumption and activation at rest [172] and significant deactivation during goal-directed tasks [67, 172, 190]. Studies of resting state functional networks have reported a high density of strong functional connections in posterior cortex [2]. In such networks, the precuneus was found to exhibit short path length, low clustering, and high centrality [1, 2]. Activation of the precuneus [40] and of other cortical midline structures [155] has been linked to self-referential processing and consciousness. Reduced metabolic activation in the posterior cingulate cortex [149], amyloid deposition, and atrophy [32], as well as impaired task-dependent deactivation in posterior medial cortex, is associated with the onset of Alzheimer-type dementia [144, 167].

The human default network comprises a set of interacting subsystems linked by hubs [30]. Key components of the default network are the posterior cingulate cortex, the precuneus, the lateral and medial parietal cortex, and the medial prefrontal cortex [66, 67, 82, 190]. Of these areas, medial prefrontal cortex is the only component entirely excluded from the structural core. Our structural results suggest the hypothesis that default network activity may be driven from highly coupled areas of the posterior medial and parietal cortex, which in turn link to other highly connected and central regions, such as the medial orbitofrontal cortex.

An important issue relates to the comparison of our present network analysis in human cortex to previous analyses carried out on anatomical connection matrices derived from tract-tracing studies in the macaque monkey. Direct comparison is made difficult by differences in spatial resolution (998 ROIs in human, 3070 regions in macaque), the incomplete coverage of macaque cortex in most extant data sets, the lack of interhemispheric connections in the macaque, the lack of connection density data in the macaque, and the

uncertainty of cross-species homologies between functionally defined brain regions [156]. A previous study focusing on the distribution of highly central hubs in macaque cortex had revealed the existence of connector hubs in some areas of prefrontal and parietal cortex [195], but was lacking connectional data on significant portions of posterior medial and frontal cortex. Here, we report ROIs with high centrality in several human cortical subregions, including medial and superior frontal cortex, inferior and superior parietal cortex, as well as cingulate and posterior medial cortex. The structural embedding of core regions within the human brain is consistent with anatomical studies of the connections of the macaque posteromedial cortex, which includes posterior cingulate and medial parietal regions. These regions are reported to have high interconnectivity as well as widespread connection patterns with other parts of the brain [163].

Previous attempts to provide a map of structural connections of the human brain have utilized correlations in cortical gray-matter thickness [100], as well as diffusion tensor imaging (DTI) [111,112]. Our approach to mapping human cortical structural connections is DSI followed by computational tractography. DSI has been shown to be especially sensitive with regard to detecting fiber crossings. In macaque monkey [182], this method has been shown to produce connection patterns that substantially agree with traditional anatomical tract tracing studies. As shown in Part II of this thesis, several studies suggest that diffusion imaging can yield accurate connection maps. However, it must be noted that the method may be participant to scanning noise, errors in fiber reconstruction, and systematic detection biases. In particular, smaller fiber tracts and interhemispheric connections toward lateral cortices may be under-represented given the limited resolution and complexity of the anatomy in the centrum semi-ovale. We note that our study focuses on a large-scale anatomical feature, the structural core, and that our main conclusions are insensitive to various degradations and manipulations of the original fiber density matrix (data not shown).

Future improvements in diffusion imaging and tractography, as well as computational network analysis, will no doubt reveal additional features of the connectional anatomy of the human brain. It will be important to include major subcortical regions, such as the thalamus, into future network analyses. Another advance would be to parcellate the cortex not on the basis of sulcal and gyral landmarks, but rather on the basis of regularities in functional connections that are observed in individual participants [48,116].

10.5 Conclusion

In this chapter, we have used the mapping of the human connectome to provide evidence for the existence of a structural core in the human cerebral cortex. This complex of densely connected regions in posterior medial cortex is both spatially and topologically central within the brain. Its anatomical correspondence with regions of high metabolic activity and with some elements of the human default network suggests that the core may be an important structural basis for shaping large-scale brain dynamics. The availability of single-participant structural and functional connection maps now provides the opportunity to investigate inter-participant connectional variability and to relate it to differences in individual functional connectivity and behavior.

Conclusion

11

11.1 Achievements

Throughout this thesis, we have investigated the possibilities of whole-brain diffusion MR tractography. After a short introduction on diffusion MRI and tractography, we have presented a methodology allowing us to obtain the human connectome from the diffusion images. This methodology has opened a window on multiple aspects of the brain connectivity. First, by combining the human connectome framework with front propagation techniques we have obtained a highly sensitive tractography algorithm, which enables the study of associative fiber tracts that can not be observed with conventional MR tractography techniques. Second, the analysis of the human connectome has revealed important characteristics of the human brain, such as its small-world architecture. We published these results in [93]. Third, by studying network properties of the human connectome we have been able to define the cortical areas that belong to the core of structural connectivity. Those areas have been shown to correspond to regions belonging to the brain's default network. This is presented in details in our publication [90].

However, without an extensive validation of MR tractography, which is the main underlying component of the human connectome, the above mentioned applications would not be meaningful. Little is known about the human brain anatomical connectivity. Few ex-vivo tracing studies have been performed and most of our knowledge is deduced from animal models. Therefore, the validation of MR tractography suffers from the lack of a gold standard. Here again, the human connectome framework has allowed to investigate unexplored ways and has turned out to be an indispensable tool towards the validation of tractography. First, we have evaluated the confidence we can have in the connections obtained from diffusion MR tractography by studying the influence of non-diffusion

effects. We have shown that whereas we can have a strong confidence in long-range connections, short-range connectivity is significantly affected by random effects and thus has to be interpreted with caution. Those results were published in [76]. Second, we have studied the relationship between the structural connectivity obtained from diffusion MR tractography and the functional connectivity obtained from resting-state functional MRI. We have observed a strong correlation between these two modalities, supporting the hypothesis of a strong relationship between structure and function in the brain. This relationship is analyzed in details in our publication [109]. Third, we have analyzed the performance of various diffusion acquisition schemes through several measurements based on the human connectome. Diffusion spectrum imaging turns out to be the most sensitive diffusion scheme and consequently the adequate candidate for MR tractography. Taken individually, each of these studies can only be considered as partial validation. However, the multiplicity of the employed techniques, along with the integration of non-diffusion modalities such as functional MRI, and finally the novelty of the whole-brain approach constitute a big step towards the definitive validation of diffusion MR tractography.

11.2 Perspectives

Improvements of the human connectome

The mapping of the human connectome may benefit from several technical improvements.

- The diffusion acquisition and the associated pre-processing steps constitute a crucial point for the accurate mapping of the human connectome. Higher spatial and angular resolutions would improve the orientational information and would lower the partial volume effects. Motion and field inhomogeneities are important sources of noise in the diffusion MR images, that may be corrected by adapting the existing correction techniques currently applied to anatomical MR data. A reduction of the acquisition time is also needed, if one wants to perform high angular resolution diffusion imaging on patients.

- Although a lot of tractography algorithms have been developed in order to maximize the information extracted from diffusion tensor imaging, their adaptation to higher angular resolution techniques such as diffusion spectrum imaging remains largely uninvestigated. A lot of work has to be done in order to fully exploit the potential of such diffusion acquisitions. Moreover, there is a great need for fiber selection methods aiming at limiting the effect of partial voluming, thus increasing the specificity of tractography.

- The parcellation of the cortex is determinant in the mapping of the human connectome. In our opinion, the major challenge consists in choosing the right criteria to define an identical node between subjects. In this thesis, we have chosen to label the nodes according to their topological position on the cortical surface. However, they could also be labelled according to some sophisticated functional MRI experiment that would partition the cortex using many activation paradigms. The connectivity itself could also be used to label the nodes, in such a way that the connectional profile is preserved. A lot of work has thus to be achieved in order to find the ideal parcellation.

Potential applications of the human connectome

The technical improvements mentioned above, that should be addressed in order to increase the precision of high-resolution structural networks, are only part of the challenge. Now that the human connectome can be mapped with diffusion MR tractography, one can foresee many extremely exciting applications in the field of basic or clinical neuroscience. However, these applications will require the development of advanced network analysis methods and visualization tools. Furthermore, with the expected accumulation of tremendous amounts of data, we will need to develop adequate systems of connectional databases, that can serve queries from a large neuroscience community needing connectional information.

Connectome visualization   Since large-scale connectional networks directly derived from *in vivo* imaging are getting more readily available, adequate representations of these complex data in a visual form is crucial in order to help the analysis. Our group is currently developing the ConnectomeViewer. We have defined the connectome file format as a XML metadata structure that contains the heterogeneous types of data, such as three dimensional brain images, surface-rendered brain structures, fiber trajectories, or networks and their associated properties. With this tool, networks can be visualized in the form of directed and undirected graphs embedded in 3D, and global network measures can be computed. It also allows the mapping of fiber pathways corresponding to a particular edge of the graph. The ConnectomeViewer is expected to provide the scientific community with an extensible and powerful tool for visualization and analysis of the human connectome.

Connectional databases   Recently, international efforts have begun to build standardized ontologies in neuroscience (www.neurolex.org), especially important in the field of neuroanatomy. We believe that embedding connectomics research in this landscape, providing highly standardized and widely available connectional information, is of the highest interest for the neuroscience community. Therefore, we propose a semantic wiki (www.connectome.ch) that would serve as a web interface to query a database hosting connectional information from different sources. Similar to existing connectivity databases such as CoCoMac (www.cocomac.org), SumsDB (http://sumsdb.wustl.edu) or BAMS (brancusi.usc.edu/bkms), this fully integrated connectome wiki and database would provide a way to store and query easily the large data sets coming from MRI connectomics in the upcoming years.

The connectome of the healthy and diseased brain   From a conceptual point of view, the nervous system is most conveniently considered as a large-scale network, and mapping its topology is essential to understand its organizing principle. For the human brain, such connectional information has been lacking for a long time, hampering the development of neuroscience [51]. As shown in this thesis, diffusion MRI tractography is about to fill this gap. The combination of structural and functional imaging developments will provide us with a more and more comprehensive map of brain connectivity. The human connectome is expected to be at the root of significant improvements in the understanding of the brain's function, both in the healthy and pathologic states, or during development and senescence.

In the near future, one will need large studies combining high quality structural and functional connectomic data with elaborate demographic, social, cognitive, somato-motor and genomic data. The collection of this information should allow us to understand the principle of brain network topology, as well as its normal variation. It should also enable, via the development of adequate models, to link structure and function. The variation of structural and functional connectional patterns will not only be characterized, but interdependence will also be studied. Even more exciting is the potential inferences we will be able to draw from a clever combination of large population based connectomic and genomic information. Indeed, except a few notorious Mendelian gene defect related to clear brain malformations, the genetic determinants of brain organization are largely unknown. Such large-scale data should enable to identify the subtle mono- or multi-genetic determinants of neuronal network topology, network myelination, network information flow and functional interaction.

From birth to early adulthood the brain undergoes dramatic modifications, axonal pruning, synaptic plasticity and myelination. Those modifications are expected to modify the neuronal network topology and information flow quite extensively. Similarly, at the other end of age spectrum, normal degenerative mechanisms induce changes in the brain white and gray matter, causing neuronal loss and modification of neuronal information transport efficacy, which inevitably translate into cognitive decline [52, 148]. On the other hand, the neuroscience community recognizes that mis- or dis-connectivity is implicated not only in the etiology of many neuro-psychiatric diseases, but also as the primary mechanism for observed morphometric changes [133, 188, 202]. Schizophrenia and Alzheimer's disease are the two most prominent examples [16, 31]. In both cases, it has been shown that widespread changes in cortical thickness, white matter structure, brain electrophysiology and metabolism occur. Those changes are supposed to be related to changes in the underlying connectivity, which likely precisely translated into the related cognitive impairment. In this context, the human connectome and its related network metrics may become important diagnostic tools, as more and more connectomics data sets, from healthy human participants and from people with clinical conditions, become available.

We hope that this thesis will contribute to the development of this extraordinary and fascinating domain of *in vivo* human brain connectivity analysis.

Bibliography

[1]   S. Achard and E. Bullmore. Efficiency and cost of economical functional brain networks. *PLoS Comp Biol*, 3:e17, 2006.

[2]   S. Achard, R. Salvador, B. Whitcher, J. Suckling, and E. Bullmore. A resilient, low-frequency, small-world human brain functional network with highly connected association cortical hubs. *J Neurosci*, 26:63–72, 2006.

[3]   R. Albert and A. Barabasi. Statistical mechanics of complex networks. *Reviews of modern physics*, 74:47–97, 2002.

[4]   R. Albert, H Jeong, and A. Barabasi. Error and attack tolerance of complex networks. *Nature*, 406:378–382, 2000.

[5]   A. L. Alexander, K. M. Hasan, M. Lazar, J. S. Tsuruda, and D. L. Parker. Analysis of partial volume effects in diffusion-tensor MRI. *Magn Res Med*, 45(5):770–780, 2001.

[6]   D. C. Alexander, G. J. Barker, and S. R. Arridge. Detection and modeling of non-gaussian apparent diffusion coefficient profiles in human brain data. *Magn Res Med*, 48:331–340, 2002.

[7]   I. Alvarez-Hamelin, L. Dall'Asta, A. Barrat, and A. Vespignani. *Advances in neural information processing systems.*, chapter Large scale networks fingerprinting and visualization using the k-core decomposition., pages 41–50. Cambridge (Massachusetts): MIT Press, 2006.

[8] A. W. Anderson. Theoretical analysis of the effects of noise on diffusion tensor imaging. *Magn Res Med*, 46(6):1174–1188, 2001.

[9] S. Angenent, S. Haker, A. Tannenbaum, and R. Kikinis. On the laplace-beltrami operator and brain surface flattening. *IEEE Trans. Medical Imaging*, 18(8):700–711, 1999.

[10] Y. Assaf and P. J. Basser. Composite hindered and restricted model of diffusion (CHARMED) MR imaging of the human brain. *Neuroimage*, 27:48–58, 2005.

[11] D. Attwell and S. B. Laughlin. An energy budget for signaling in the grey matter of the brain. *J Cereb Blood Flow Metab*, 21:1133–1145, 2001.

[12] A. Barrat, M. Barthelemy, R. Pastor-Satorras, and A. Vespignani. The architecture of complex weighted networks. *Proc Natl Acad Sci U S A*, 101:3747–3752, 2004.

[13] A. Bartels and S. Zeki. Brain dynamics during natural viewing conditions: a new guide for mapping connectivity in vivo. *Neuroimage*, 24:339–349, 2005.

[14] P. Basser, J. Mattiello, and D. LeBihan. Estimation of the effective self-diffusion tensor from the NMR spin echo. *J Magn Res B*, 103:247–254, 1994.

[15] P. J. Basser, S. Pajevic, C. Pierpaoli, J. Duda, and A. Aldroubi. In vitro fiber tractography using DT-MRI data. *Magn Reson Med*, 44:625–632, 2000.

[16] D. S. Bassett, E. Bullmore, B. A. Verchinski, V. S. Mattay, D. R. Weinberger, et al. Hierarchical organization of human cortical networks in health and schizophrenia. *J Neurosci*, 28:9239–9248, 2008.

[17] D. S. Bassett, A. Meyer-Lindenberg, S. Achard, T. Duke, and E. Bullmore. Adaptive reconfiguration of fractal small-world human brain functional networks. *Proc Natl Acad Sci USA*, 103:19518–19523, 2006.

[18] B. Batagelj and A. Mrvar. Pajek - program for large network analysis. *Connections*, 21:47–57, 1998.

[19] C. Beaulieu. The basis of anisotropic water diffusion in the nervous system - a technical review. *NMR in Biomedicine*, 15:435–455, 2002.

[20] T. E. Behrens and H. Johansen-Berg. Relating connectional architecture to grey matter function using diffusion imaging. *Philos Trans R Soc Lond B Biol Sci*, 360:903–911, 2005.

[21] T. E. Behrens, H. Johansen-Berg, S. Jbabdi, M. F. Rushworth, and M. W. Woolrich. Probabilistic diffusion tractography with multiple fiber orientations: what can we gain? *Neuroimage*, 34:144–155, 2007.

[22] T. E. J. Behrens, M. W. Woolrich, M. Jenkinson, H. Johansen-Berg, R. G. Nunes, et al. Characterization and propagation of uncertainty in diffusion-weighted MR imaging. *Magn Res Med*, 50(5):1077–1088, 2003.

[23] Y. A. Bhagat, M. S. Hussain, R. W. Stobbe, K. S. Butcher, D. J. Emery, et al. Elevations of diffusion anisotropy are associated with hyper-acute stroke: a serial imaging study. *Magn Reson Med*, 26:683–693, 2008.

[24] D. Le Bihan. *Diffusion and Perfusion Magnetic Resonance Imaging.* Raven Press, Ltd., New York, 1995.

[25] D. Le Bihan. Looking into the functional architecture of the brain with diffusion MRI. *Nat Rev Neurosci*, 4:469–480, 2003.

[26] D. Le Bihan, J.-F Mangin, C. Poupon, C. A. Clark, S. Pappata, et al. Diffusion tensor imaging: Concepts and applications. *Journal of Magnetic Resonance Imaging*, 13:534–546, 2001.

[27] M. Breakspear, J. Terry, and K. Friston. Modulation of excitatory synaptic coupling facilitates synchronization and complex dynamics in a biophysical model of neuronal dynamics. *Network: Computation in Neural Systems*, 14:703–732, 2003.

[28] P. Broca. Remarks on the seat of the faculty of articulated language, following an observation of aphemia (loss of speech). *Bulletin de la Société Anatomique*, 6:330–357, 1861.

[29] R. Brown. A brief account of microscopical observations made in the months of june, july and august, 1827, on the particles contained in the pollen of plants; and on the general existence of active molecules in organic and inorganic bodies. *Phil. Mag.*, 4:161–173, 1827.

[30] R. L. Buckner, J. R. Andrews-Hanna, and D. L. Schacter. The brain's default network. anatomy, function, and relevance to disease. *Ann N Y Acad Sci*, 1124:1–38, 2008.

[31] R. L. Buckner, J. Sepulcre, T. Talukdar, F. M. Krienen, H. Liu, et al. Cortical hubs revealed by intrinsic functional connectivity: mapping, assessment of stability, and relation to Alzheimer's disease. *J Neurosci*, 29:1860–1873, 2009.

[32] R. L. Buckner, A. Z. Snyder, B. J. Shannon, G. LaRossa, R. Sachs, et al. Molecular, structural and functional characterization of Alzheimer's disease: Evidence for a relationship between default activity, amyloid, and memory. *J Neurosci*, 25:7709–7717, 2005.

[33] E. Bullmore and O. Sporns. Complex brain networks: graph theoretical analysis of structural and functional systems. *Nat Rev Neurosci*, 10:186–198, 2009.

[34] G. A. Burns and M. P. Young. Analysis of the connectional organization of neural systems associated with the hippocampus in rats. *Philos Trans R Soc Lond B Biol Sci*, 355:55–70, 2000.

[35] P. T. Callaghan. *Principles of Nuclear Magnetic Resonance Microscopy.* Oxford science publications, 1991.

[36] L. Cammoun, P. Hagmann, X. Gigandet, P. Maeder, J.-P. Thiran, et al. A method to study alterations in networks of structural connectivity. In *Proc Intl Soc Mag Reson Med*, volume 15, page 235, 2007.

[37] J. S. W. Campbell, K. Siddiqi, V. V. Rymar, A. F. Sadikot, and G. B. Pike. Flow-based fiber tracking with diffusion tensor and q-ball data: validation and comparison to principal diffusion direction techniques. *Neuroimage*, 27(4):725–736, 2005.

[38] M. Catani and M. Mesulam. The arcuate fasciculus and the disconnection theme in language and aphasia: history and current state. *Cortex*, 44:953–961, 2008.

[39] M. Catani and M. Mesulam. What is a disconnection syndrome? *Cortex*, 44:911–913, 2008.

[40] A. E. Cavanna and M. R. Trimble. The precuneus: a review of its functional anatomy and behavioural correlates. *Brain*, 129:564–583, 2006.

[41] B. L. Chen, D. H. Hall, and D. B. Chklovskii. Wiring optimization can relate neuronal structure and function. *Proc Natl Acad Sci USA*, 103:4723–4728, 2006.

[42] T. L. Chenevert, J. A. Brunberg, and J. G. Pipe. Anisotropic diffusion within human white matter: demonstration with NMR techniques in vivo. *Radiology*, 177:401–405, 1990.

[43] C. Cherniak. Component placement optimization in the brain. *J Neurosci*, 14:2418–2427, 1994.

[44] D. B. Chklovskii, T. Schikorski, and C. F. Stevens. Wiring optimization in cortical circuits. *Neuron*, 34:341–347, 2002.

[45] H. Chui, J. Rambo, J. Duncan, R. Schultz, and A. Rangarajan. Registration of cortical anatomic structures via robust 3D point matching. *Lecture Notes in Computer Science*, 1613, 1999.

[46] O. Ciccarelli, A. T. Toosy, G. J. M. Parker, C. A. M. Wheeler-Kingshott, G. J. Barker, et al. Diffusion tractography based group mapping of major white-matter pathways in the human brain. *Neuroimage*, 19:1545–1555, 2003.

[47] S. Clarke, S. Riahi-Arya, E. Tardif, A. C. Eskenasy, and A. Probst. Thalamic projections of the fusiform gyrus in man. *Eur J Neurosci*, 11:1835–1838, 1999.

[48] A. L. Cohen et al. Defining functional areas in individual human brains using resting functional connectivity MRI. *Neuroimage*, 41:45–57, 2008.

[49] D. L. Collins, G. Le Goualher, and A. C. Evans. Non-linear cerebral registration with sulcal constraints. In *MICCAI'98*, 1998.

[50] T. E. Conturo, N. F. Lori, T. S. Cull, E. Akbudak, A. Z. Snyder, et al. Tracking neuronal fiber pathways in the living human brain. *Proc Natl Acad Sci U S A*, 96:10422–10427, 1999.

[51] F. Crick and E. Jones. Backwardness of human neuroanatomy. *Nature*, 361:109–110, 1993.

[52] J. S. Damoiseaux, C. F. Beckmann, E. J. Arigita, F. Barkhof, P. Scheltens, et al. Reduced resting-state brain activity in the default network in normal aging. *Cereb Cortex*, 18:1856–1864, 2008.

[53] J. S. Damoiseaux et al. Consistent resting-state networks across healthy participants. *Proc Natl Acad Sci USA*, 103:13848–13853, 2006.

[54] R. S. Desikan, F. Segonne, B. Fischl, B. T. Quinn, B. C. Dickerson, et al. An automated labelling system for subdividing the human cerebral cortex on MRI scans into gyral based regions of interest. *Neuroimage*, 31(3):968–980, 2006.

[55] E. W. Dijkstra. A note on two problems in connexion with graphs. *Numerische Mathematik*, 1:269–271, 1959.

[56] V. M. Eguiluz, D. R. Chialvo, G. A. Cecchi, M. Baliki, and A. V. Apkarian. Scale-free brain functional networks. *Phys Rev Lett*, 94:018102, 2005.

[57] A. Einstein. Über die von der molekularkinetischen Theorie der Wärme geforderte Bewegung von in ruhenden Flüssigkeiten suspendierten Teilchen. *Annalen der Physik*, 17:549–560, 1905.

[58] G. B. Ermentrout and D. Kleinfeld. Traveling electrical waves in cortex: insights from phase dynamics and speculations on a computational role. *Neuron*, 29:33–44, 2001.

[59] D. J. Felleman and D. C. Van Essen. Distributed hierarchical processing in the primate cerebral cortex. *Cereb Cortex*, 1:1–47, 1991.

[60] A. Fick. Über diffusion. *Annalen der Physik und Chemie*, pages 59–86, 1855.

[61] B. Fischl, A. Van Der Kouwe, C. Destrieux, E. Halgren, E. Segonne, et al. Automatically parcellating the human cerebral cortex. *Cereb Cortex*, 14(1):11–22, 2004.

[62] B. Fischl, D. H. Salat, E. Busa, M. Albert, M. Dieterich, et al. Whole brain segmentation: automated labeling of neuroanatomical structures in the human brain. *Neuron*, 33:341–355, 2002.

[63] B. Fischl, M. I. Sereno, and A. M. Dale. Cortical surface-based analysis II: Inflation, flattening, and a surface-based coordinate system. *Neuroimage*, 9(2):195–207, February 1999.

[64] B. Fischl, M. I. Sereno, R. B. Tootell, and A. M. Dale. High-resolution intersubject averaging and a coordinate system for the cortical surface. *Hum. Brain Mapp.*, 8(4):272–284, 1999.

[65] M. D. Fox, M. Corbetta, A. Z. Snyder, J. L. Vincent, and M. E. Raichle. Spontaneous neuronal activity distinguishes human dorsal and ventral attention systems. *Proc Natl Acad Sci USA*, 103:10046–10051, 2006.

[66] M. D. Fox and M. E. Raichle. Spontaneous fluctuations in brain activity observed with functional magnetic resonance imaging. *Nat Rev Neurosci*, 8:700–711, 2007.

[67] M. D. Fox, A. Z. Snyder, J. L. Vincent, M. Corbetta, D. C. Van Essen, and M. E. Raichle. The human brain is intrinsically organized into dynamic, anticorrelated functional networks. *Proc Natl Acad Sci USA*, 102:9673–9678, 2005.

[68] M. D. Fox, A. Z. Snyder, J. M. Zacks, and M. E. Raichle. Coherent spontaneous activity accounts for trial-to-trial variability in human evoked brain responses. *Nat Neurosci*, 9:23–25, 2005.

[69] L. R. Frank. Anisotropy in high angular resolution diffusion-weighted MRI. *Magn Res Med*, 45:935–939, 2001.

[70] L. C. Freeman. A set of measures of centrality based on betweenness. *Sociometry*, 40:35–41, 1977.

[71] K. J. Friston. Functional and effective connectivity in neuroimaging: A synthesis. *Hum Brain Mapp*, 2:56–78, 1994.

[72] K. J. Friston. Beyond phrenology: what can neuroimaging tell us about distributed circuitry. *Annu Rev Neurosci*, 25:221–250, 2002.

[73] P. Funk. Über eine geometrische Anwendung der Abelschen Integralgleichnung. *Math. Ann.*, 77:129–135, 1916.

[74] F. J. Gall and G. Spurzheim. *Anatomie et physiologie du système nerveux en général et du cerveau en particulier, avec des observations sur la possibilité de reconnaître plusieurs dispositions intellectuelles et morales de l'homme et des animaux par la configuration de leurs têtes.* F. Schoell (Paris) ed., 1810-1819.

[75] A. Ghosh, Y. Rho, A. R. McIntosh, R. Kotter, and V. K. Jirsa. Noise during rest enables the exploration of the brains dynamic repertoire. *PLoS Comput Biol*, 4:e1000196, 2008.

[76] X. Gigandet, P. Hagmann, M. Kurant, L. Cammoun, R. Meuli, and J.-P. Thiran. Estimating the confidence level of white matter connections obtained with MRI tractography. *PLoSONE*, 3:e4006, 2008.

[77] G. Gilbert, D. Simard, and G. Beaudoin. Impact of an improved combination of signals from array coils in diffusion tensor imaging. *IEEE Trans Med Imaging*, 26:1428–1436, 2007.

[78] G. Gong, Y. He, L. Concha, C. Lebel, D. W. Gross, et al. Mapping anatomical connectivity patterns of human cerebral cortex using in vivo diffusion tensor imaging tractography. *Cereb Cortex*, 19(3):524–536, 2009.

[79] C. Granziera, J. D. Schmahmann, N. Hadjikhani, H. Meyer, R. Meuli, et al. Diffusion spectrum imaging shows the structural basis of functional cerebellar circuits in the human cerebellum in vivo. *PLoSONE*, 4:e5101, 2009.

[80] C. M. Gray, P. Konig, A. K. Engel, and W. Singer. Oscillatory responses in cat visual cortex exhibit inter-columnar synchronization which reflects global stimulus properties. *Nature*, 338:334–337, 1989.

[81] M. Greicius. Resting-state functional connectivity in neuropsychiatric disorders. *Curr Opin Neurol*, 24:424–430, 2008.

142

[82] M. D. Greicius, B. Krasnow, A. L. Reiss, and V. Menon. Functional connectivity in the resting brain: a network analysis of the default mode hypothesis. *Proc Natl Acad Sci USA*, 100:253–258, 2003.

[83] M. D. Greicius and V. Menon. Default-mode activity during a passive sensory task: uncoupled from deactivation but impacting activation. *J Cogn Neurosci*, 16:1484–1492, 2004.

[84] M. D. Greicius, K. Supekar, V. Menon, and R. F. Dougherty. Resting-state functional connectivity reflects structural connectivity in the default mode network. *Cereb Cortex*, 19:72–78, 2009.

[85] L. Gross. From structure to function: Mapping the connection matrix of the human brain. *PLoS Biol*, 6:e164, 2008.

[86] R. Guimera, M. Sales-Pardo, and L. A. N. Amaral. Classes of complex networks defined by role-to-role connectivity profiles. *Nat Phys*, 3:63–69, 2007.

[87] D. A. Gusnard and M. E. Raichle. Searching for a baseline: functional imaging and the resting human brain. *Nat Rev Neurosci*, 2:685–694, 2001.

[88] M. Guye, F. Bartolomei, and J. P. Ranjeva. Imaging structural and functional connectivity: towards a unified definition of human brain organization? *Curr Opin Neurol*, 24:393–403, 2008.

[89] P. Hagmann. *From diffusion MRI to brain connectomics*. PhD thesis, Ecole Polytechnique Fédérale de Lausanne, 2005.

[90] P. Hagmann, L. Cammoun, X. Gigandet, R. Meuli, C. J. Honey, et al. Mapping the structural core of human cerebral cortex. *PLOS Biology*, 6(7):1479–1493, 2008.

[91] P. Hagmann, X. Gigandet, R. Meuli, R. Kötter, O. Sporns, et al. Quantitative validation of MR tractography using the CoCoMac database. In *Proc Intl Soc Mag Reson Med*, volume 16, 2008.

[92] P. Hagmann, L. Jonasson, P. Maeder, J.-P. Thiran J-P, V. J. Wedeen, et al. Understanding diffusion MR imaging techniques: From scalar diffusion-weighted imaging to diffusion tensor imaging and beyond. *Radiographics*, 26:205–223, 2006.

[93] P. Hagmann, M. Kurant, X. Gigandet, P. Thiran, Wedeen V. J., et al. Mapping human whole-brain structural networks with diffusion MRI. *PloSONE*, 2(7), 2007.

[94] P. Hagmann, M. Kurant, X. Gigandet, P. Thiran, V. J. Wedeen, et al. Imaging the brain neuronal network with diffusion mri: a way to understand its global architecture. In *Proc Intl Soc Mag Reson Med*, volume 14, 2006.

[95] P. Hagmann, T. Reese, W.-Y. I. Tseng, R. Meuli, J.-P. Thiran, et al. Diffusion spectrum imaging tractography in complex cerebral white matter: An investigation of the centrum semiovale. In *Proc Intl Soc Mag Reson Med*, volume 12, 2004.

[96] P. Hagmann, J.-P. Thiran, L. Jonasson, P. Vandergheynst, S. Clarke, et al. DTI mapping of human brain connectivity: statistical fibre tracking and virtual dissection. *Neuroimage*, 19(3):545–554, 2003.

[97] M. Hampson, N. R. Driesen, P. Skudlarski, J. C. Gore, and R. T Constable. Brain connectivity related to working memory performance. *J Neurosci*, 26:13338–13343, 2006.

[98] B. J. He, G. L. Shulman, A. Z. Snyder, and M. Corbetta. The role of impaired neuronal communication in neurological disorders. *Curr Opin Neurol*, 20:655–660, 2007.

[99] B. J. He, A. Z. Snyder, J. M. Zempel, M. D. Smyth, and M. E. Raichle. Electrophysiological correlates of the brains intrinsic large-scale functional architecture. *Proc Natl Acad Sci USA*, 105:16039–16044, 2008.

[100] Y. He, Z. J. Chen, and A. C. Evans. Small-world anatomical networks in the human brain revealed by cortical thickness from MRI. *Cerebr Cortex*, 17:2407–2419, 2007.

[101] M. Hebert, K. Ikeuchi, and H. Delingette. A spherical representation for recognition of free-form surfaces. *IEEE Transactions on Pattern Analysis and Machine Intelligence*, 17(7):681–690, July 1995.

[102] S. Helgason. *The Radon Transform, Volume 5.* Springer-Verlag, 1999.

[103] P. Hellier, C. Barillot, I. Corouge, B. Gibaud, G. Le Goualher, D. L. Collins, A. Evans, G. Malandain, N. Ayache, G. E. Christensen, and H. J. Johnson. Retrospective evaluation of intersubject brain registration. *IEEE Trans. Medical Imaging*, 22(9):1120–1130, 2003.

[104] C. A. Hidalgo, B. Klinger, A.-L. Barabasi, and R. Hausmann. The product space conditions the development of nations. *Science*, 317:482–487, 2007.

[105] C. C. Hilgetag, G. A. Burns, M. A. O'Neill, J. W. Scannell, and M. P. Young. Anatomical connectivity defines the organization of clusters of cortical areas in the macaque monkey and the cat. *Philos Trans R Soc Lond B Biol Sci*, 355:91–110, 2000.

[106] C. C. Hilgetag and M. Kaiser. Clustered organization of cortical connectivity. *Neuroinformatics*, 2(3):353–360, 2004.

[107] C. C. Hilgetag, M. A. O'Neill, and M. P. Young. Hierarchical organization of macaque and cat cortical sensory systems explored with a novel network processor. *Philos Trans R Soc Lond B Biol Sci*, 355:71–89, 2000.

[108] C. J. Honey, R. Kötter, M. Breakspear, and O. Sporns. Network structure of cerebral cortex shapes functional connectivity on multiple time scales. *Proc Natl Acad Sci USA*, 104:10240–10245, 2007.

[109] C. J. Honey, O. Sporns, L. Cammoun, X. Gigandet, J.-P. Thiran, et al. Predicting human resting-state functional connectivity from structural connectivity. *Proc Natl Acad Sci U S A*, 106:2035–2040, 2009.

[110] M. Humphries, K. Gurney, and T. Prescott. The brainstem reticular formation is a small-world, not scale-free, network. *Proc of the Royal Society B-Biological Sciences*, 273:503–511, 2006.

[111] Y. Iturria-Medina, E. J. Canales-Rodriguez, L. Melie-Garcia, P. A. Valdes-Hernandez, E. Martinez-Montes, et al. Characterizing brain anatomical connections using diffusion weighted MRI and graph theory. *Neuroimage*, 36:645–660, 2007.

[112] Y. Iturria-Medina, R. C. Sotero, E. J. Canales-Rodriguez, Y. Aleman-Gomez, and L. Melie-Garcia. Studying the human brain anatomical network via diffusion-weighted MRI and graph theory. *Neuroimage*, 40:1064–1076, 2008.

[113] E. M. Izhikevich and G. M. Edelman. Large-scale model of mammalian thalamo-cortical systems. *Proc Natl Acad Sci USA*, 105:3593–3598, 2008.

[114] S. Jbabdi, P. Bellec, R. Toro, J. Daunizeau, M. Pélégrini-Issac, et al. Accurate anisotropic fast marching for diffusion-based geodesic tractography. *International Journal of Biomedical Imaging*, page 320195, 2008.

[115] H. K. Jeong, S.-K. Lee, D. I. Kim, and J. H. Heo. The usefulness of fractional anisotropy maps in localization of lacunar infarctions in striatum, internal capsule and thalamus. *Neuroradiology*, 47:267–270, 2005.

[116] H. Johansen-Berg, T. E. J. Behrens, M. D. Robson, I. Drobnjak, M. F. S. Rushworth, et al. Changes in connectivity profiles define functionally distinct regions in human medial frontal cortex. *Proc Natl Acad Sci USA*, 101:13335–13340, 2004.

[117] J. M. Johnston et al. Loss of resting interhemispheric functional connectivity after complete section of the corpus callosum. *J Neurosci*, 28:6453–6458, 2008.

[118] D. K. Jones and C. Pierpaoli. Confidence mapping in diffusion tensor magnetic resonance imaging tractography using a bootstrap approach. *Magn Res Med*, 53(5):1143–1149, 2005.

[119] M. Kaiser. Brain architecture: a design for natural computation. *Phil Trans R Soc A*, 365:3033–3045, 2007.

[120] M. Kaiser and C. Hilgetag. Modelling the development of cortical systems networks. *Neurocomputing*, 58-60:297–302, 2004.

[121] M. Kaiser and C. C. Hilgetag. Nonoptimal component placement, but short processing paths, due to long-distance projections in neural systems. *PLoS Comput Biol*, 2:e95, 2006.

[122] G. Kalna and D. Higham. Clustering coefficients for weighted networks. *University of Strathclyde Mathematics.*, 2006.

[123] T. Kamada and S. Kawai. An algorithm for drawing general undirected graphs. *Inf Proc Lett*, 31:7–15, 1989.

[124] R. A. Kanaan, S. S. Sukhwinder, G. J. Gareth, M. Catani, V. W. Ng, et al. Tract-specific anisotropy measurements in diffusion tensor imaging. *Neuroimage*, 146:73–82, 2006.

[125] M. H. Khachaturian, J. J. Wisco, and D. S. Tuch. Boosting the sampling efficiency of q-ball imaging using multiple wavevector fusion. *Magn Reson Med*, 57:289–296, 2007.

[126] J. C. Klein, T. E. Behrens, M. D. Robson, C. E. Mackay, D. J. Higham, et al. Connectivity-based parcellation of human cortex using diffusion MRI: Establishing reproducibility, validity and observer independence in BA 44/45 and SMA/pre-SMA. *Neuroimage*, 34:204–211, 2007.

[127] V. A. Klyachko and C. F. Stevens. Connectivity optimization and the positioning of cortical areas. *Proc Natl Acad Sci U S A*, 100(13):7937–7941, 2003.

[128] C. Koch and G. Laurent. Complexity and the nervous system. *Science*, 284:96–98, 1999.

[129] M. Koch, V. Glauche, J. Finsterbusch, U. Nolte, J. Frahm, et al. Estimation of anatomical connectivity from diffusion tensor data. *Neuroimage*, 13(6):176, 2001.

[130] M. A. Koch, D. G. Norris, and M. Hund-Georgiadis. An investigation of functional and anatomical connectivity using magnetic resonance imaging. *Neuroimage*, 16:241–250, 2002.

[131] B. W. Kreher, I. Mader, and V. G. Kiselev. Gibbs tracking: A novel approach for the reconstruction of neuronal pathways. *Magn Reson Med*, 60:953–963, 2008.

[132] L.-W. Kuo, J.-H. Chen, V. J. Wedeen, and W.-Y. I. Tseng. Optimization of diffusion spectrum imaging and q-ball imaging on clinical MRI system. *Neuroimage*, 41:7–18, 2006.

[133] M. Kyriakopoulos, T. Bargiotas, G. J. Barker, and S. Frangou. Diffusion tensor imaging in schizophrenia. *Eur Psychiatry*, 23:255–273, 2008.

[134] V. Latora and M. Marchiori. Efficient behavior of small-world networks. *Phys Rev Lett*, 87:198701, 2001.

[135] S. B. Laughlin and T. J. Sejnowski. Communication in neuronal networks. *Science*, 301:1870–1874, 2003.

[136] P. C. Lauterbur. Image formation by induced local interactions: Examples of employing nuclear magnetic resonance. *Nature*, 242:190–191, 1973.

[137] M. Lazar and A. L. Alexander. An error analysis of white matter tractography methods: synthetic diffusion tensor field simulations. *Neuroimage*, 20(2):1140–1153, 2003.

[138] M. Lazar and A. L. Alexander. Bootstrap white matter tractography (BOOT-TRAC). *Neuroimage*, 24(2):524–532, 2005.

[139] K. V. Leemput, F. Maes, D. Vandermeulen, and P. Suetens. Automated model-based bias field correction of MR images of the brain. *IEEE Tran Med Imag*, 18:885–896, 1999.

[140] H. Lester and S. Arridge. A survey of hierarchical non-linear medical image registration. *Pattern Recognition*, 32(1):129–149, 1999.

146

[141] J. D. Lewis, R. J. Theilmann, M. I. Sereno, and J. Townsend. The relation between connection length and degree of connectivity in young adults: A DTI analysis. *Cereb Cortex*, 19:554–562, 2008.

[142] C.-P. Lin, V. J. Wedeen, J.-H. Chen, C. Yao, and W.-Y. I. Tseng. Validation of diffusion spectrum magnetic resonance imaging with manganese-enhanced rat optic tracts and ex vivo phantoms. *Neuroimage*, 19(3):482–495, 2003.

[143] N. F. Lori, E. Akbudak, J. S. Shimony, T. S. Cull, A. Z. Snyder, et al. Diffusion tensor fiber tracking of human brain connectivity: acquisition methods, reliability analysis and biological results. *NMR Biomed*, 15(7-8):494–515, 2002.

[144] C. Lustig, A. Z. Snyder, M. Bhakta, K. C. O'Brien, M. McAvoy, et al. Functional deactivations: Change with age and dementia of the alzheimer type. *Proc Natl Acad Sci USA*, 100:14504–14509, 2003.

[145] F. Maes, A. Collignonand, D. Vandermeulen, G. Marchal, and P. Suetens. Multi-modality image registration by maximization of mutual information. *IEEE Tran Med Imag*, 16:187–198, 1997.

[146] D. Mantini, M. G. Perrucci, C. Del Gratta, G. L. Romani, and M. Corbetta. Electrophysiological signatures of resting state networks in the human brain. *Proc Natl Acad Sci USA*, 104:13170–13175, 2007.

[147] S. Maslov and K. Sneppen. Specificity and stability in topology of protein networks. *Science*, 296:910–913, 2002.

[148] D. Meunier, S. Achard, A. Morcom, and E. Bullmore. Age-related changes in modular organization of human brain functional networks. *Neuroimage*, 44:715–723, 2009.

[149] S. Minoshima, B. Giordani, S. Berent, K. A. Frey, N. L. Foster, et al. Metabolic reduction in the posterior cingulate cortex in very early alzheimer's disease. *Ann Neurol*, 42:85–94, 1997.

[150] S. Mori, B. J. Crain, V. P. Chacko, and P. C. van Zijl. Three-dimensional tracking of axonal projections in the brain by magnetic resonance imaging. *Ann Neurol*, 45:265–269, 1999.

[151] S. Mori, B. J. Crain, V. P. Chacko, and M. Van Zijl. Three-dimensional tracking of axonal projections in the brain by magnetic resonance imaging. *Annals of neurology*, 45:265–269, 2001.

[152] S. Mori and P.C. Van Zijl. Fiber tracking: Principles and strategies - a technical review. *NMR Biomed*, 15:468–480, 2002.

[153] M. E. J. Newman. Assortative mixing in networks. *Phys Rev Lett*, 89:208701, 2002.

[154] M. E. J. Newman. Modularity and community structure in networks. *Proc Natl Acad Sci USA*, 103:8577–8582, 2006.

[155] G. Northoff and F. Bermpohl. Cortical midline structures and the self. *Trends Cogn Sci*, 8:102–107, 2004.

[156] G. A. Orban, D. Van Essen, and W. Vanduffel. Comparative mapping of higher visual areas in monkeys and humans. *Trends Cogn Sci*, 8:315–324, 2004.

[157] C.-H. Park, S. Y. Kim, Y.-H. Kim, and K. Kim. Comparison of the small-world topology between anatomical and functional connectivity in the human brain. *Physica A*, 387:5958–5962, 2008.

[158] G. J. M. Parker and D. C. Alexander. Probabilistic anatomical connectivity derived from the microscopic persistent angular structure of cerebral tissue. *Phil Trans R Soc B*, 360:893–902, 2005.

[159] G. J. M. Parker, H. A. Haroon, and C. A. M. Wheeler-Kingshott. A framework for a streamline-based probabilistic index of connectivity (PICo) using a structural interpretation of MRI diffusion measurements. *Journ Magn Res*, 18(2):242–254, 2003.

[160] G. J. M. Parker, C. A. M. Wheeler-Kingshott, and G. J. Barker. Estimating distributed anatomical connectivity using fast marching methods and diffusion tensor imaging. *IEEE Tran Med Imag*, 21(5):505–512, 2002.

[161] S. C. Partridge, P. Mukherjee, R. G. Henry, S. P. Miller, J. I. Berman, et al. Diffusion tensor imaging: serial quantitation of white matter tract maturity in premature newborns. *Neuroimage*, 22:1302–1314, 2004.

[162] J. Parvizi, G. W. Van Hoesen, J. Buckwalter, and A. Damasio. Neural connections of the posteriomedial cortex in the macaque. *Proc Natl Acad Sci USA*, 103:1563–1568, 2005.

[163] J. Parvizi, G. W. Van Hoesen, J. Buckwalter, and A. Damasio. Neural connections of the posteromedial cortex in the macaque. *Proc Natl Acad Sci USA*, 103:1563–1568, 2006.

[164] R. E. Passingham, K. E. Stephan, and R. Kötter. The anatomical basis of functional localization in the cortex. *Nat Rev Neurosci*, 3:606–616, 2002.

[165] O. Pasternak, Y. Assaf, N. Intratora, and N. Sochen. Variational multiple-tensor fitting of fiber-ambiguous diffusion-weighted magnetic resonance imaging voxels. *Magn Reson Med*, 26:1133–1144, 2008.

[166] M. Perrin, C. Poupon, Y. Cointepas, B. Rieul, N. Golestani, et al. Fiber tracking in q-ball fields using regularized particle trajectories. *Inf Process Med Imaging*, 19:52–63, 2005.

[167] J. R. Petrella, L. Wang, S. Krishnan, M. J. Slavin, S. E. Prince, et al. Cortical deactivation in mild cognitive impairment: High-field-strength functional MR imaging. *Radiology*, 245:224–235, 2007.

[168] C. Poupon, J.-F. Mangin, C. A. Clark, V. Frouin, J. Régis, et al. Towards inference of human brain connectivity from MR diffusion tensor data. *Medical Image Analysis*, 5:1–15, 2001.

[169] M. C. Putnam, G. S. Wig, S. T. Grafton, W. M. Kelley, and M. S. Gazzaniga. Structural organization of the corpus callosum predicts the extent and impact of cortical activity in the nondominant hemisphere. *J Neurosci*, 28:2912–2918, 2008.

[170] L. Qingfen. *Enhancement, extraction, and visualization of 3D volume data.* PhD thesis, Linköpings University (Sweden), 2003.

[171] M. Quigley et al. Role of the corpus callosum in functional connectivity. *Am J Neuroradiol*, 24:208–212, 2003.

[172] M. E. Raichle et al. A default mode of brain function. *Proc Natl Acad Sci USA*, 98:676–682, 2001.

[173] T. G. Reese, T. Benner, R. Wang, D. A. Feinberg, and V. J. Wedeen. Halving imaging time of whole brain diffusion spectrum imaging and diffusion tractography using simultaneous image refocusing in EPI. *J Magn Reson Imag*, 29:517–522, 2009.

[174] T. G. Reese, O. Heid, R. M. Weisskoff, and V. J. Wedeen. Reduction of eddy-current-induced distortion in diffusion MRI using a twice-refocused spin echo. *Magn Reson Med*, 49:177–182, 2003.

[175] D. Rubino, K. A. Robbins, and N. G. Hatsopoulos. Propagating waves mediate information transfer in the motor cortex. *Nat Neurosci*, 9:1549–1557, 2006.

[176] E. Rykhlevskaia, G. Gratton, and M. Fabiani. Combining structural and functional neuroimaging data for studying brain connectivity: a review. *Psychophysiology*, 45:173–187, 2008.

[177] R. Salvador et al. Neurophysiological architecture of functional magnetic resonance images of human brain. *Cereb Cortex*, 15:1332–1342, 2005.

[178] J. Saramaki, M. Kivela, J.-P. Onnela, K. Kaski, and J. Kertesz. Generalizations of the clustering coefficient to weighted complex networks. *arXiv.org*, 2006.

[179] J. W. Scannell, C. Blakemore, and M. P. Young. Analysis of connectivity in the cat cerebral cortex. *J Neurosci*, 15:1463–1483, 1995.

[180] J. W. Scannell, G. A. Burns, C. C. Hilgetag, M .A. O'Neil, and M. P. Young. The connectional organization of the cortico-thalamic system of the cat. *Cereb Cortex*, 9:277–299, 1999.

[181] J. D. Schmahmann and D. N. Pandya. *Fiber pathways of the brain.* New York, 2006.

[182] J. D. Schmahmann, D. N. Pandya, R. Wang, G. Dai, H. E. D'Arceuil, et al. Association fibre pathways of the brain: parallel observations from diffusion spectrum imaging and autoradiography. *Brain*, 130(3):630–653, 2007.

[183] J. D. Schmahmann, E. E. Smith, Florian S. Eichler, and C. M. Filley. Cerebral white matter: neuroanatomy, clinical neurology, and neurobehavioral correlates. *Ann. N. Y. Acad. Sci.*, 1142:266–309, 2008.

[184] J. A. Sethian. A fast marching level set method for monotonically advancing fronts. *Proc Natl Acad Sci USA*, 93:1591–1595, 1996.

[185] J. A. Sethian. *Level set methods and fast marching methods.* Cambridge University Press, Mass, USA, 2002.

[186] J. A. Sethian and A. Vladimirsky. Ordered upwind methods for static hamilton-jacobi equations. *Proc Natl Acad Sci USA*, 98:11069–11074, 2001.

[187] K. K. Seunarine, P. A. Cook, M. G. Hall, K. V. Embleton, G. J. M. Parker, et al. Exploiting peak anisotropy for tracking through complex structures. *IEEE International Conference on Computer Vision*, 0:1–8, 2007.

[188] M. E. Shenton, C. C. Dickey, M. Frumin, and R. W. McCarley. A review of MRI findings in schizophrenia. *Schizophr Res*, 49:1–52, 2001.

[189] K. Shmueli et al. Low-frequency fluctuations in the cardiac rate as a source of variance in the resting-state fMRI BOLD signal. *Neuroimage*, 38:306–320, 2007.

[190] G. L. Shulman, J. A. Fiez, M. Corbetta, R. L. Buckner, F. M. Miezin, et al. Common blood flow changes across visual tasks: II. decreases in cerebral cortex. *J Cogn Neurosci*, 9:648–663, 1997.

[191] E. P. Simoncelli and B. A. Olshausen. Natural image statistics and neural representation. *Annu Rev Neurosci*, 24:1193–1216, 2001.

[192] S. M. Smith, M. Jenkinson, M. W. Woolrich, C. F. Beckmann, T. E. J. Behrens, et al. Advances in functional and structural MR image analysis and implementation as FSL. *Neuroimage*, 23:208–219, 2004.

[193] R. C. Sotero and N. J. Trujillo-Barreto. Biophysical model for integrating neuronal activity, EEG, fMRI and metabolism. *Neuroimage*, 39:290–309, 2008.

[194] O. Sporns, D. Chialvo, M. Kaiser, and C. C. Hilgetag. Organization, development and function of complex brain networks. *Trends Cogn Sci*, 8:418425, 2004.

[195] O. Sporns, C. J. Honey, and R. Kötter. Identification and classification of hubs in brain networks. *PLoS ONE*, 2:e1049, 2007.

[196] O. Sporns, G. Tononi, and R. Kötter. The human connectome: A structural description of the human brain. *PLoS Comput Biol*, 1:e42, 2005.

[197] O. Sporns and J. D. Zwi. The small world of the cerebral cortex. *Neuroinformatics*, 2:145–162, 2004.

[198] P. Staempfli, T. Jaermann, G. R. Crelier, S. Kollias, A. Valavanis, et al. Resolving fiber crossing using advanced fast marching tractography based on diffusion tensor imaging. *Neuroimage*, 30:110–120, 2006.

[199] C. J. Stam, B. F. Jones, G. Nolte, M. Breakspear, and P. Scheltens. Small-world networks and functional connectivity in alzheimer's disease. *Cereb Cortex*, 17:92–99, 2007.

[200] E. Stejskal and J. Tanner. Spin diffusion measurements - spin echoes in presence of a time-dependent field gradient. *J. Chem. Phys*, 42(1):288–292, 1965.

[201] K. E. Stephan, J. J. Riera, G. Deco, and B. Horwitz. The brain connectivity workshops: moving the frontiers of computational systems neuroscience. *Neuroimage*, 42:1–9, 2008.

[202] P. M. Thompson and L. G. Apostolova. Computational anatomical methods as applied to ageing and dementia. *Br J Radiol*, 80:78–91, 2007.

[203] P. M. Thompson and A. W. Toga. A surface-based technique for warping 3-dimensional images of the brain. *IEEE Trans. Medical Imaging*, 15(4):402–417, 1996.

[204] P. Thottakara, M. Lazar, S. C. Johnson, and A. L. Alexander. Application of brodmann's area templates for ROI selection in white matter tractography studies. *Neuroimage*, 29:868–878, 2006.

[205] A. W. Toga. *Brain Warping*. Academic Press, 1999.

[206] V. Tomassini, S. Jbabdi, J. C. Klein, T. E. Behrens, C. Pozzilli, et al. Diffusion-weighted imaging tractography-based parcellation of the human lateral premotor cortex identifies dorsal and ventral subregions with anatomical and functional specializations. *J Neurosci*, 27:10259–10269, 2007.

[207] G. Tononi and G. M. Edelman. Consciousness and complexity. *Science*, 282:1846–1851, 1998.

[208] A. Toosy, O. Ciccarelli, G. J. M. Parker, C. A. M. Wheeler-Kingshott, D. H. Miller, et al. Characterizing function structure relationships in the human visual system with functional MRI and diffusion tensor imaging. *Neuroimage*, 21:1452–1463, 2004.

[209] D. Tosun, M. E. Rettmann, and J. L. Prince. Mapping techniques for aligning sulci across multiple brains. *Med. Image Anal.*, 8(3):295–309, 2004.

[210] J. D. Tournier, F. Calamante, M. King, D. G. Gadian, and A. Connelly. Limitations and requirements of diffusion tensor fiber tracking: an assessment using simulations. *Magn Res Med*, 47(4):701–708, 2002.

[211] J. D. Tournier, C.-H. Yeh, F. Calamante, K.-H. Cho, A. Connelly, et al. Resolving crossing fibres using constrained spherical deconvolution: validation using diffusion-weighted imaging phantom data. *Neuroimage*, 42:617–625, 2008.

[212] D. S. Tuch. *Diffusion MRI of complex tissue structure*. PhD thesis, Massachusetts Institute of Technology, 2002.

[213] D. S. Tuch. Q-ball imaging. *Magn Res Med*, 52:1358–1372, 2004.

[214] D. S. Tuch, J. W. Belliveau, and V. J. Wedeen. A path integral approach to white matter tractography. In *Proc Intl Soc Mag Reson Med*, volume 8, 2000.

[215] D. S. Tuch, T. Reese, M. Wiegell, and V. J. Wedeen. Diffusion MRI of complex neural architecture. *Neuron*, 40(5):885–895, 2003.

[216] D. S. Tuch, T. G. Reese, M. R. Wiegell, N. Makris, J. W. Belliveau, et al. High angular resolution diffusion imaging reveals intravoxel white matter fiber heterogeneity. *Magn Res Med*, 48:577–582, 2002.

[217] L. Q. Uddin et al. Residual functional connectivity in the split-brain revealed with resting-state functional MRI. *Neuroreport*, 19:703–709, 2008.

[218] L. G. Ungerleider and M. Mishkin. *Analysis of visual behavior*, chapter Two cortical visual systems, pages 549–586. Cambridge (Massachusetts): MIT Press, 2006.

[219] M. Vaillant and C. Davatzikos. Finding parametric representations of the cortical sulci using an active contour model. *Med. Image Anal.*, 1(4):295–315, 1997.

[220] S. Vanhatalo et al. Infraslow oscillations modulate excitability and interictal epileptic activity in the human cortex during sleep. *Proc Natl Acad Sci USA*, 101:5053–5057, 2004.

[221] J. L. Vincent et al. Coherent spontaneous activity identifies a hippocampal-parietal memory network. *J Neurophysiol*, 96:3517–3531, 2006.

[222] J. L. Vincent et al. Intrinsic functional architecture in the anaesthetized monkey brain. *Nature*, 447:83–86, 2007.

[223] G. Di Virgilio, S. Clarke, G. Pizzolato, and T. Schaffner. Cortical regions contributing to the anterior commissure in man. *Exp Brain Res*, 124:1–7, 1999.

[224] D. Watts and S. Strogatz. Collective dynamics of 'small-world' networks. *Nature*, 393:440–442, 1998.

[225] V. J. Wedeen. Diffusion aniostropy and white matter tracts. In *Second Int. Conf. Funct. Mapp. Human Brain*, volume 2, page 146, 1996.

[226] V. J. Wedeen, P. Hagmann, W.-Y. Tseng, T. Reese, and R. Weisskoff. Mapping complex tissue architecture with diffusion spectrum magnetic resonance imaging. *Magn Res Med*, 54:1377–1386, 2005.

[227] V. J. Wedeen, T. Reese, D. S. Tuch, M. Weigel, J.-G. Dou, et al. Mapping fiber orientation spectra in cerebral white matter with fourier-transform diffusion MRI. In *Proc Intl Soc Mag Reson Med*, volume 8, 2000.

[228] V. J. Wedeen, R. P. Wang, J. D. Schmahmann, T. Benner, W. Y. Tseng, et al. Diffusion spectrum magnetic resonance imaging (DSI) tractography of crossing fibers. *Neuroimage*, 41:1267–1277, 2008.

[229] C. Wernicke. *Der aphasische Symptomencomplex*. Schulz-Kirchner, 2005.

[230] M. W. Woolrich, S. Jbabdi, B. Patenaude, M. Chappell, S. Makni, et al. Advances in functional and structural MR image analysis and implementation as FSL. *Neuroimage*, 45:173–186, 2009.

[231] R. Xue, P. C. M. Van Zijl, B J Crain, M. Solaiyappan, and S. Mori. In vivo three-dimensional reconstruction of rat brain axonal projections by diffusion tensor imaging. *Magn Reson Med*, 42:1123–1127, 1999.

[232] E. Zaidel, F. Aboitiz, and J. Clarke. Sexual dimorphism in interhemispheric relations: anatomical-behavioral convergence. *Biol Res*, 28:27–43, 1995.

[233] E. Zarahn, G. K. Aguirre, and M. DEsposito. Empirical analyses of BOLD fMRI statistics. I. spatially unsmoothed data collected under null-hypothesis conditions. *Neuroimage*, 5:179–197, 1997.

[234] K. Zhang and T. J. Sejnowski. A universal scaling law between gray matter and white matter of cerebral cortex. *Proc Natl Acad Sci USA*, 97:5621–5626, 2000.

Curriculum Vitae

Name:	Xavier Gigandet

Birthdate:	May 1, 1982
Nationality:	Swiss
Civil status:	Married

Address:	Ch. Derrière-le-Château 21
	1033 Cheseaux-sur-Lausanne
	Switzerland
Phone:	+41 79 519 06 83
Email:	xavier.gigandet@epfl.ch

Currently

- **Ph.D. student** at the Signal Processing Laboratory (LTS5), Ecole Polytechnique Fédérale de Lausanne, Switzerland.

Degree

- **Master of Electrical and Electronics Engineering**, Ecole Polytechnique Fédérale de Lausanne, Switzerland.

Publications

Journal Papers

- Honey C, Sporns O, Cammoun L, Gigandet X, Thiran J-P, Meuli R, Hagmann P. (2009) Predicting human resting-state functional connectivity from structural connectivity. Proceedings of the National Academy of Sciences of the USA. 106(6):2035-2040.

- Gigandet X, Hagmann P, Kurant M, Cammoun L, Meuli R, Thiran J-P. (2008) Estimating the confidence level of white matter connections obtained with MRI tractography. PLoSONE. 3(12):e4006.

- Hagmann P, Cammoun L, Gigandet X, Meuli R, Honey C, Sporns O. (2008) Mapping the structural core of human cerebral cortex. PLoS Biology. 6(7):e159.

- Hagmann P, Kurant M, Gigandet X, Thiran P, Wedeen VJ, Meuli R, Thiran J-P. (2007) Mapping human whole-brain structural networks with diffusion MRI. PLoS ONE. 2(7):e597.

Conference Papers

- Cammoun L, Gigandet X, Hagmann P, Meuli R, Thiran J-P. (2009) Diffusion MR image segmentation: towards global brain connectivity analysis. Proceedings of the 10th European Congress of Stereology and Image Analysis, Milano, Italy.

- Cammoun L, Gigandet X, Sporns O, Thiran J-P, Maeder P, Meuli R, Hagmann P, Bovet P, Do KQ. (2009) Connectome alterations in schizophrenia. 15th Annual Meeting Human Brain Mapping, San Francisco, USA

- Honey C, Sporns O, Cammoun L, Gigandet X, Thiran J-P, Meuli R, Hagmann P. (2009) Predicting resting-state functional connectivity from structural connectivity. Proc. Intl. Soc. Mag. Reson. Med. 17, Hawaii, USA.

- Cammoun L, Gigandet X, Sporns O, Thiran J-P, Do KQ, Maeder P, Meuli R, Hagmann P, Bovet P. (2009) Mapping the human connectome at multiple scales with diffusion spectrum MRI. Proc. Intl. Soc. Mag. Reson. Med. 17, Hawaii, USA.

- Sporns O, Cammoun L, Gigandet X, Meuli R, Honey C, Hagmann P. (2008) Mapping the structural core of human cerebral cortex. 14th Annual Meeting Human Brain Mapping, Melbourne, Australia.

- Honey C, Sporns O, Cammoun L, Gigandet X, Meuli R, Hagmann P. (2008) Predicting resting-state functional connectivity from structural connectivity. 14th Annual Meeting Human Brain Mapping, Melbourne, Australia.

- Gigandet X, Cammoun L, Meuli R, Thiran J-P, Hagmann P. (2008) Fast-marching tractography for connection matrix (Fast-TraC). Proc. Intl. Soc. Mag. Reson. Med. 16, Toronto, Canada.

- Hagmann P, Gigandet X, Meuli R., Kötter R, Sporns O, Wedeen VJ. (2008) Quantitative validation of MR tractography using the CoCoMac database. Proc. Intl. Soc. Mag. Reson. Med. 16, Toronto, Canada.

- Hagmann P, Cammoun L, Gigandet X, Meuli R, Honey C, Sporns O. (2008) The structural core of human cerebral cortex and its relation to the brain's default network. Proc. Intl. Soc. Mag. Reson. Med. 16, Toronto, Canada.

- Gigandet X, Hagmann P, Kurant M, Thiran J-P, Meuli R. (2007) How much confidence do we have in a MRI tractography experiment? Proc. Intl. Soc. Mag. Reson. Med. 15, Berlin, Germany.

- Cammoun L, Hagmann P, Gigandet X, Maeder P, Thiran J-P, Meuli R. (2007) A method to study alterations in networks of structural connectivity. Proc. Intl. Soc. Mag. Reson. Med. 15, Berlin, Germany.

- Hagmann P, Gigandet X, Cammoun L, Wedeen VJ, Maeder P, Thiran J-P, Meuli R. (2007) Deriving scalar maps from diffusion spectrum MRI. Proc. Intl. Soc. Mag. Reson. Med. 15, Berlin, Germany.

- Hagmann P, Gigandet X, Wedeen VJ, Meuli R, Thiran J-P. (2006) Statistical DSI brain tractography: a way to handle the kiss-cross uncertainty. Proc. Intl. Soc. Mag. Reson. Med. 14, Seattle, USA.

- Hagmann P, Kurant M, Gigandet X, Thiran P, Wedeen VJ, Meuli R, Thiran J-P. (2006) Imaging the brain neuronal network with diffusion MRI: a way to understand its global architecture. Proc. Intl. Soc. Mag. Reson. Med. 14, Seattle, USA.

- Gigandet X, Bach Cuadra M, Pointet A, Cammoun L, Caloz R, Thiran J-P. (2005) Region-based satellite image classification: method and validation. IEEE International Conference on Image Processing (ICIP).

Master Thesis

- Gigandet X. (2004) Satellite image segmentation and classification. EPFL, Lausanne, Switzerland.

Educational History

- **2005 - 2009:** Ph.D. student at the Signal Processing Laboratory (LTS5), Ecole Polytechnique Fédérale de Lausanne, Switzerland.

- **2000 - 2005:** Master student in electrical and electronics engineering, Ecole Polytechnique Fédérale de Lausanne, Switzerland.

- **2000:** Federal Diploma of Maturity type C (sciences).

Postgraduate Education

- **June 2006:** Biomedical Imaging: IEEE Summer School on Biomedical Imaging, Berder Island, France.

Skills

Languages

French:	mother tongue
English:	fluent oral and written
German:	intermediate

Computing

Operating systems:	Windows, Linux, Unix
Programming languages:	C/C++, Java, Matlab